

Estimation and Correction of Tropospheric and Ionospheric Effects on Differential SAR Interferograms

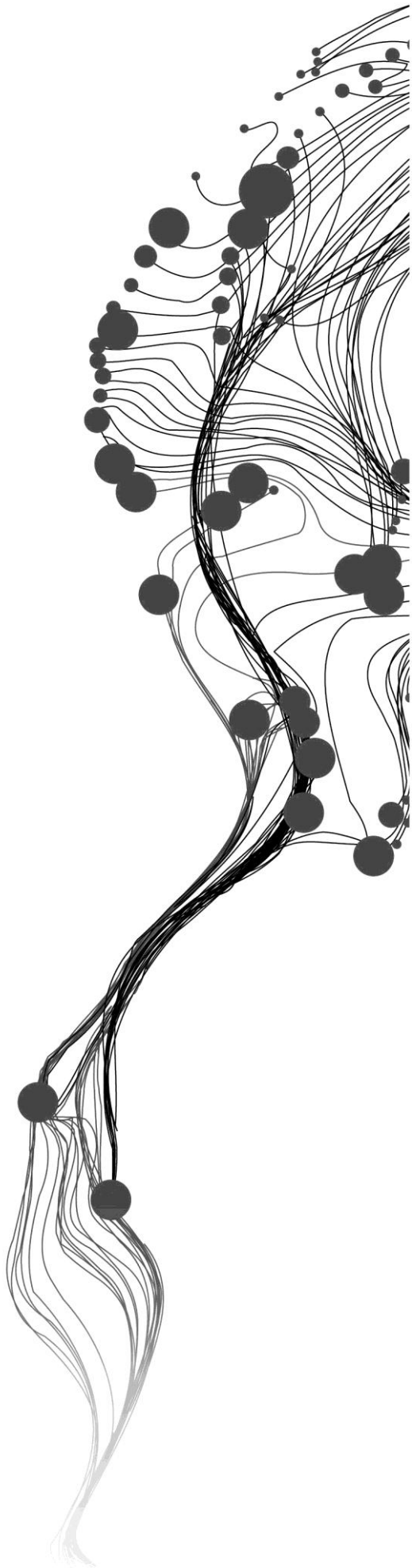
PREETHI MALUR BALAJI

April, 2011

SUPERVISORS:

Mr. Shashi Kumar

Mr. Gerrit Huurnemann



Estimation and Correction of Tropospheric and Ionospheric Effects on Differential SAR Interferograms

PREETHI MALUR BALAJI

Enschede, The Netherlands, April, 2011

Thesis submitted to the Faculty of Geo-Information Science and Earth Observation of the University of Twente in partial fulfilment of the requirements for the degree of Master of Science in Geo-information Science and Earth Observation.

Specialization: M.Sc. Geoinformatics

SUPERVISORS:

Mr. Shashi Kumar

Mr. Gerrit Huurnemann

THESIS ASSESSMENT BOARD:

Prof. Dr. Ir. A. Alfred Stein (Chair)

Mr. P. L. N. Raju

Dr. A. Senthil Kumar (External Examiner, National Remote Sensing Centre)

DISCLAIMER

This document describes work undertaken as part of a programme of study at the Faculty of Geo-Information Science and Earth Observation of the University of Twente. All views and opinions expressed therein remain the sole responsibility of the author, and do not necessarily represent those of the Faculty.

*Dedicated to my Loving Family
and Friends*

ABSTRACT

The repeat-pass Synthetic Aperture Radio Detection and Ranging (RADAR) Interferometry (InSAR) has been a widely used geodetic technique for observing the Earth's surface, especially for mapping the Earth's topography and deformations. However, InSAR measurements are prone to atmospheric errors. RADAR waves traverse the Earth's atmosphere twice and experience a delay due to atmospheric refraction. The two major layers of the atmosphere (troposphere and ionosphere) are mainly responsible for this delay in the propagating RADAR wave. Previous studies have shown that water vapour and clouds present in the troposphere and the Total Electron Content (TEC) of the ionosphere are responsible for the additional path delay in the RADAR wave. The tropospheric delay considering the two-way propagation can add up to 16 m. The tropospheric refractivity is mainly dependent on pressure, temperature and partial pressure of water vapour. To calculate the amount of tropospheric delay occurred, the Moderate Resolution Imaging Spectroradiometer (MODIS) data is used. On the other hand, the ionosphere has a major influence on L-band data. With the help of TEC maps, the ionospheric delay for the month of June, August and September was calculated and found to vary from -8 m to -13 m. The tropospheric refractivity leads to an increase in the observed range and ionospheric electron density leads to propagation path shortenings. These induced propagation delays affect the quality of phase measurement and introduce errors in the topography and deformation fields. The effect of this delay is studied on three-pass differential interferogram (DInSAR) generated from two interferograms. The interferograms generated from three Advanced Land Observation Satellite (ALOS) carrying Phased Array L-band Synthetic Aperture RADAR (PALSAR) Single Look Complex (SLC) images acquired on the same study area are subjected to atmospheric phase correction. The study area consists of different types of scatterers exhibiting different coherence. The correction applied on the interferograms for the entire study area does not prove to be much effective. This is because of baseline decorrelation and phase noise such as temporal decorrelation and volume scattering. When the region within the study site showing high coherence is considered, the correction in that particular region has given effective results. A DInSAR with zero baseline and coherence between the images equal to one should give phase differences equal to zero. A DInSAR generated from the two corrected interferograms when compared with the original DInSAR gives phase difference values close to zero and not exactly zero because of the non-zero baseline factor. Any movement or change in the surface of the land would introduce phase variations which is the principle behind DInSAR. The atmospheric phase error obtained may be confused with the displacement component. Unless the phase values due to atmospheric disturbances are not corrected, it is difficult to obtain accurate measurements. Thus, the atmospheric error correction is essential for all practical applications of DInSAR to avoid inaccurate erratic height and deformation measurements.

Keywords: Atmosphere, troposphere, ionosphere, path delay, total electron content, Interferometric synthetic aperture radar, differential interferometry, phase, baseline

ACKNOWLEDGEMENTS

First and foremost, I would like to extend my deepest gratitude to my IIRS supervisor Mr. Shashi Kumar who stood as a backbone throughout my research period. Without his constant support, guidance and encouragement, the completion of this research work would not have been possible. I am very grateful to him for having given me an opportunity to work as his student and for sharing his immense knowledge with me.

I am extremely thankful to my ITC supervisor Dr. Gerrit Huurneman who encouraged me and guided me in the right direction and helped me with his valuable suggestions and comments which made my work a success.

I would like to thank Dr. Nicholas Hamm for the support and encouragement he offered throughout the course period. I would specially like to owe him my gratitude for making our stay easier and pleasant at ITC.

I would like to thank Dr. P.S Roy (Dean IIRS), Mr. P.L.N. Raju (Head of Department, Geoinformatics Division) for their support and providing excellent infrastructure facilities to implement the research work. A special thanks to all the members of CMA for providing technical inventory for the research.

A special thanks to Mr. Rahul Raj for extending his help whenever in need. I would also like to thank Dr. Reshu Agarwal for being so helpful and approachable during my initial stages of research work.

Last but not the least, a very deep gratitude to my friends Tanvi Rajput, Sourabh Pargal, Deepak Upreti, Shreyes Shiv, Charles Richardson, Poonam Singh and Anwar Hashemi for creating a very friendly and cooperative environment and for providing me all the help and support I needed throughout my research period.

TABLE OF CONTENTS

List of Figures.....	v
List of Tables.....	vii
List of Acronyms.....	viii
1. INTRODUCTION.....	1
1.1. Background.....	1
1.2. SAR Interferometry (InSAR).....	1
1.3. Differential Interferometry (DInSAR).....	2
1.3.1. DInSAR Principles.....	2
1.4. Problem statement.....	3
1.4.1. Troposphere.....	3
1.4.2. Ionosphere.....	3
1.5. Research identification.....	3
1.5.1. Main objective.....	4
1.5.2. Sub-objectives.....	4
1.5.3. Research questions.....	4
1.6. Structure of the thesis.....	4
2. LITERATURE REVIEW.....	5
2.1. Introduction.....	5
2.2. InSAR.....	5
2.3. DInSAR.....	6
2.4. Study of atmospheric effects on RADAR interferometry.....	10
2.4.1. Tropospheric Effects.....	10
2.4.2. Ionospheric Effects.....	16
3. STUDY AREA.....	18
3.1. Attributes of the study area.....	18
3.2. Scientific importance of the study area.....	20
4. MATERIALS AND METHODS.....	21
4.1. Materials.....	22
4.2. Effects of Atmospheric Propagation.....	23
4.2.1. Introduction to the Earth's atmosphere.....	23
4.2.2. Troposphere case.....	24
4.3. Ionospheric case.....	25
4.4. Generation of DInSAR.....	28
4.4.1. Image Coregistration.....	28
4.4.2. Multibaseline Estimation.....	29
4.4.3. Interferogram Generation.....	30

4.4.4.	Interferogram Flattening	32
4.4.5.	Interferogram Adaptive Filter and Coherence Generation – Boxcar Window	33
4.4.6.	Phase Unwrapping.....	35
4.4.7.	DInSAR generation from the two interferograms	37
4.5.	Phase Correction	38
5.	RESULTS AND DISCUSSIONS.....	40
5.1.	Path delay as an effect of atmospheric propagation.....	40
5.2.	A discussion on the degree of similarity (coherence) between the three images.....	43
5.3.	Effects of phase correction on interferogram	49
5.3.1.	Correction on phase of DInSAR	59
5.3.1.1.	DInSAR Error Map	60
5.4.	Validation of the corrected interferograms.....	66
6.	CONCLUSIONS AND RECOMMENDATIONS	68
6.1.	Conclusions.....	68
6.2.	Recommendations	69
	List of References.....	70

LIST OF FIGURES

Figure 1.1: Two-pass DInSAR	2
Figure 1.2: Three-pass DInSAR.....	2
Figure 2.1: Imaging geometry of RADAR.....	7
Figure 3.1: Location of the study area (Google image)	19
Figure 4.1: Flow Diagram of Methodology.....	21
Figure 4.2: TEC map showing yearly and monthly TEC variations	26
Figure 4.3: Master Image on which total path delay is calculated.....	27
Figure 4.4: Slave image 1 on which total path delay is calculated.....	27
Figure 4.5: Slave image 2 on which total path delay is calculated.....	28
Figure 4.6: Interferogram of first image pair (Master image and Slave image 1)	31
Figure 4.7: Interferogram of second image pair (Master image and Slave image 2).....	32
Figure 4.8: Flattened interferogram generated from the first pair (Master image and Slave image 1).....	33
Figure 4.9: Flattened interferogram generated from the second pair (Master image and Slave image 2)	33
Figure 4.10: Coherence image obtained from the first pair (Master image and Slave image 1).....	35
Figure 4.11: Coherence image obtained from the second pair (Master image and Slave image 2)	35
Figure 4.12: Phase unwrapped interferogram obtained from the first pair (Master image and Slave image 1)	36
Figure 4.13: Phase unwrapped interferogram obtained from the second pair (Master image and Slave image 2)	36
Figure 4.14: Differential Interferogram (DInSAR) obtained from the three SAR images (Master, Slave 1 and Slave2).....	37
Figure 5.1: Histogram showing the tropospheric path delay caused on the day of acquisition of Master image.....	40
Figure 5.2: Histogram showing the tropospheric path delay caused on the day of acquisition of Slave image 1.....	41
Figure 5.3: Histogram showing the tropospheric path delay caused on the day of acquisition of Slave image 2.....	41
Figure 5.4: Troposphere Ionosphere delay (total path delay) occurred on June 16, 2010.....	42
Figure 5.5: Troposphere Ionosphere delay (total path delay) occurred on August 01, 2010.....	42
Figure 5.6: Troposphere Ionosphere delay (total path delay) occurred on September 16, 2010.....	43
Figure 5.7: Google image of Region 1 showing settlement areas	44
Figure 5.8: Region 1 showing high coherence between Master image and Slave image 1.....	44
Figure 5.9: Region 1 showing high coherence between Master image and Slave image 2.....	45
Figure 5.10: Google image of Region 2 showing settlement areas	45
Figure 5.11: Region 2 showing high coherence between Master image and Slave image 1.....	46
Figure 5.12: Region 2 showing high coherence between Master image and Slave image 2.....	46
Figure 5.13: Variation of coherence between the two image pairs (Region 1)	47
Figure 5.14: Variation of coherence between the two image pairs (Region 2)	48
Figure 5.15: Phase image (Pair 1) before correction	49
Figure 5.16: Phase variation of Pair 1 before correction.....	49
Figure 5.17: Phase image (Pair 1) after correction	50
Figure 5.18: Phase variation of Pair 1 after correction	50
Figure 5.19: Phase image (Pair 2) before correction	51

Figure 5.20: Phase variation of Pair 2 before correction	52
Figure 5.21: Phase image (Pair 2) after correction	52
Figure 5.22: Phase variation of Pair 2 after correction.....	53
Figure 5.23: Pair 1 (100 points chosen on entire study area)	55
Figure 5.24: Pair 1 (100 points chosen on region 1 of study area)	56
Figure 5.25: Pair 2 (100 points chosen on entire study area)	57
Figure 5.26: Pair 2 (100 points chosen on region 1 of study area)	58
Figure 5.27: Phase image of DInSAR before correction	59
Figure 5.28: Phase variation of DInSAR before correction	59
Figure 5.29: DInSAR Error Map.....	60
Figure 5.30: Phase image of DInSAR after correction.....	61
Figure 5.31: Phase variation of DInSAR after correction	61
Figure 5.32: Phase of DInSAR before and after correction.....	63
Figure 5.33: DInSAR (100 points chosen on region 1 of study area).....	64
Figure 5.34: DInSAR before correction	65
Figure 5.35: DInSAR after correction.....	66

LIST OF TABLES

Table 2.1: Effects related to TEC	16
Table 3.1: Scene Boundary	20
Table 4.1: Dataset	22
Table 4.2: Dataset extent	23
Table 4.3: Interferometric pairs	28
Table 4.4: Normal Baseline values for all possible interferometric pairs	30
Table 4.5: Critical Baseline values	30
Table 5.1: Path delay calculated from TEC	42
Table 5.2: Error ranges estimated in DInSAR	60

LIST OF ACRONYMS

RADAR	Radio Detection and Ranging
SAR	Synthetic Aperture Radar
RAR	Real Aperture Radar
InSAR	Interferometric Synthetic Aperture Radar
DInSAR	Differential Interferometric Synthetic Aperture Radar
SLC	Single Look Complex
MODIS	Moderate Resolution Imaging Spectroradiometer
ALOS PALSAR	Advanced Land Observation Satellite Phased Array L-band Synthetic Aperture Radar
TEC	Total Electron Content
TID	Travelling Ionospheric Disturbance
HDF-EOS	Hierarchical Data Format – Earth Observing System
FBD	Fine Beam Dual polarized
CODE	Centre for Orbit Determination in Europe
GIM	Global Ionospheric Map

1. INTRODUCTION

1.1. Background

The exploitation of electromagnetic spectrum including microwaves has led to remarkable inventions such as radio and television, mobile communication, microwave ovens and radio detection and ranging system [1]. The microwave signals are part of the spectrum with wavelengths between 1 centimetre and 1 meter. The development in the field of microwave remote sensing has helped to shape models of the world as we know it today.

Microwaves are applied for Conventional Radio Detection and Ranging (RADAR) technology. RADAR is not only used for detection and ranging but also for imaging of the Earth surface. As such it is considered as a remote sensing technique. The Earth surface is illuminated by microwave signals and from the reflected signals an image can be created in offline processing. Microwaves are, compared to the visual part of the electromagnetic spectrum, relatively long and they have the ability to penetrate through the clouds and are independent of some atmospheric conditions such as haze.

Imaging of the Earth can be done by Real Aperture RADAR (RAR) systems but the resolution of the acquired data from spaceborne systems is about 5-10 km. The resolution is limited by the power and size of the footprint of the RADAR beam which in itself is based on the aperture size, and thus its use is limited for few remote sensing applications [2]. This limitation in providing the useful spatial resolutions is overcome by Synthetic Aperture RADAR (SAR) systems. In SAR technique a large antenna is synthesized by means of offline processing techniques which use the Doppler Effect in the acquired data. SAR combines the techniques of signal processing and satellite orbit information and thus produces a much higher resolution (tens of meters) RADAR image. SAR processing helps to significantly improve the resolution of images in both the cross-track (range) and along-track (azimuth) direction.

1.2. SAR Interferometry (InSAR)

Synthetic aperture RADAR (SAR) interferometry (InSAR) is a processing technique which can be used to measure the topography of a surface [3]. It is a technique in which two SAR images are combined to produce an interferogram. An interferogram is a phase interference image [4]. The raw SAR images are in complex-valued format containing both amplitude and phase information per pixel. An interferogram is formed by taking pixel-to-pixel phase differences between the two images. The phase difference is calculated by the multiplication of one image by the complex conjugate of the other. This results in a phase difference image which is termed as interferogram. From this interferometric phase image, relative terrain elevation can be derived using also orbit data of the two images.

InSAR can be classified into single-pass and repeat-pass interferometry which are based on the number of platforms involved. Single-pass interferometry is performed either with one-antenna or two-antenna SAR system. For a one-antenna system, revisit to the same scene is required which is hence termed as repeat-pass interferometry [5].

1.3. Differential Interferometry (DInSAR)

SAR is an extensive tool to measure the topography of the surface, its changes over time and also other changes in the surface [3]. In SAR interferometry, the deformation signal obtained from the Earth surface is mixed with topographic signal [6]. To overcome this problem, differential interferogram is used. Differential Synthetic Aperture RADAR Interferometry or DInSAR is used in remote sensing for measuring Earth surface deformation [7]. This technique is considered more accurate than InSAR as it is capable of providing relative measures up to few centimetres or less [8].

1.3.1. DInSAR Principles

This technique requires minimum three single-look complex (SLC) images in order to form at least two interferometric phase measurements. The phases corresponding to each pixel in the SLC images are calculated and differenced to form an interferogram.

There are three types of DInSAR. They are two-pass, three-pass and four-pass DInSAR [9]. A differential interferogram (DInSAR) can also be generated using an interferometric image pair and a digital elevation model (DEM). Figure [1.1] and Figure [1.2] show two-pass and three-pass DInSAR respectively.

Basic principle

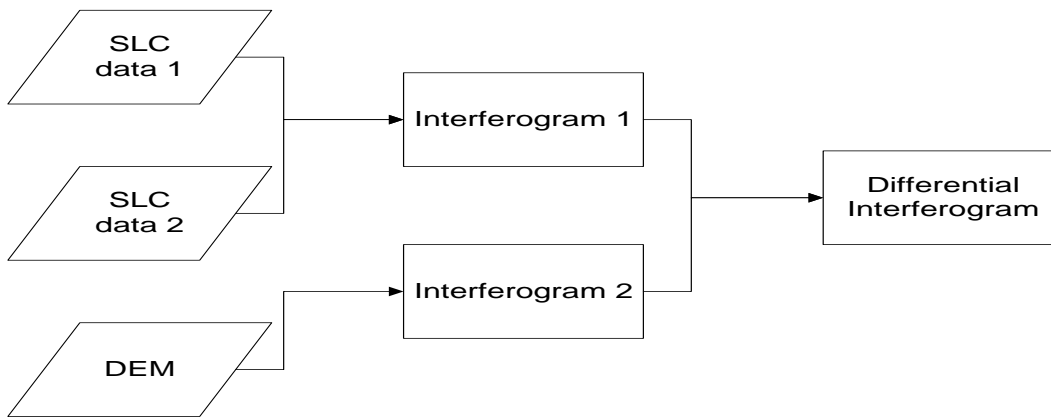


Figure 1.1: Two-pass DInSAR

Source: [9]

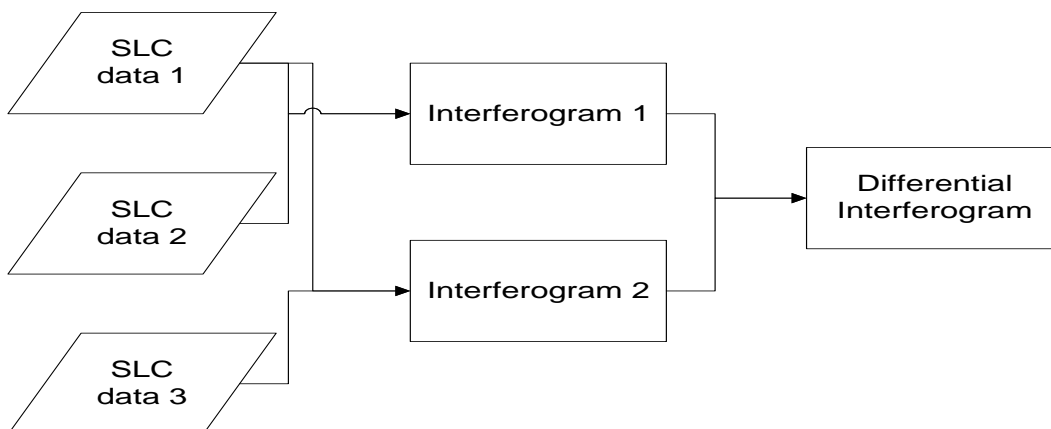


Figure 1.2: Three-pass DInSAR

Source: [9]

When two interferograms are formed from three SLC images, the interferogram phases are again differenced to form one more interferogram which is termed as “Double-Differenced Interferogram” [10]. This step removes phase changes due to topography and a new phase image is formed. The final phase of the DInSAR consists of surface change phase contributions, atmospheric delay contribution and phase noise. The atmospheric effects which contribute to phase differences cannot be easily distinguished from surface displacements. The effect of atmospheric contributions has an impact on altitude and surface deformation measurements [11].

DInSAR using space borne sensors has become an established tool for the analysis of very small surface deformations. The idea behind this is to analyze the phase differences between SAR interferograms caused by surface displacements between the data acquisitions. As the SAR sensors possess short wavelength, surface movements on the centimetre scale can easily be detected.

1.4. Problem statement

When a RADAR wave propagates through the atmosphere, two types of errors may potentially be introduced viz. bending and propagation delays. The bending effect is negligible based on the incidence angles of the satellites [12]. Hence, in this study, propagation delay is taken under consideration. This is one of the main limitations of DInSAR which is caused due to atmosphere. The atmosphere is divided into two major layers, ionosphere and troposphere [12]. These layers affect the propagation of electromagnetic waves, due to their different refractive indices. The repeat-pass InSAR shows random variations in phase due to atmospheric heterogeneities giving inaccurate measurements [13].

1.4.1. Troposphere

The troposphere which is the lowest portion of the Earth’s atmosphere contains 99% of water vapour and aerosols. The path delay due to troposphere is caused due to air refractivity gradients [7]. The air refractivity gradients in the troposphere are due to the dry air pressure, temperature, air moisture and condensed water in clouds or rain.

1.4.2. Ionosphere

The ionosphere is characterized by free electrons that are created by external sources such as ultraviolet radiation from the Sun [6]. These external sources create free electrons by knocking them off from atoms. The number of free electrons present in the ionosphere is represented by electron density in electrons per cubic meter [6].

The electron density in the ionosphere creates propagation path shortenings and the partial pressure of water vapour in troposphere causes an increase in the observed range.

This research work aims at atmospheric delay correction in the phase of a three-pass DInSAR. The path delay is calculated using Moderate Resolution Imaging Spectroradiometer (MODIS) data.

1.5. Research identification

To arrive at a solution for the problem statement mentioned in section 1.4, the below mentioned research objectives and research questions have been formulated.

1.5.1. Main objective

To estimate the troposphere and ionosphere error induced in the phase of a differential interferogram and to minimize this error.

1.5.2. Sub-objectives

- To estimate the effect of troposphere and ionosphere on a RADAR wave using a model.
- To study the effect of troposphere and ionosphere on the phase of differential interferogram.
- To correct the error induced in the phase of the differential interferogram.

1.5.3. Research questions

- What are the constituents of the troposphere and ionosphere that affect the RADAR signals?
- What will be the effect of troposphere and ionosphere on the RADAR signal?
- What will be the techniques used to minimize the error?
- What will be the accuracy of the DInSAR after error correction?

1.6. Structure of the thesis

The whole thesis has been divided into six chapters. The first chapter includes an overview of the major aspects covered in the research work, problem statement, research objectives and questions. In the second chapter literature review is given in which the related works with respect to the present research work are presented. In the third chapter information about the chosen study area is given. The methodology and details about the dataset used are given in fourth chapter. Fifth chapter has been dedicated to a detailed discussion on the results obtained. Finally, in the sixth chapter, the thesis has been concluded along with some future recommendations.

2. LITERATURE REVIEW

2.1. Introduction

The growth of differential RADAR interferometry can be in a nutshell comprehended by a simple progress flow as Radio Detection and Ranging (RADAR) – Synthetic Aperture RADAR (SAR) – Interferometric SAR (InSAR) – Differential Interferometric SAR (DInSAR). The history of RADAR can be traced back to 19th century in which the significant discovery of radio waves and electromagnetism by Maxwell and Hertz changed the world [1]. Significant improvements of RADAR technology in the upcoming years led to the development of SAR. The Coherent RADAR, in which both phase and amplitude information are received, acted as the key factor for the advances in RADAR. An artificially long antenna was created synthetically using a moving antenna, which combined the information of received pulse returns within the synthetic antenna length. A SAR system enabled satellite was launched in June 1978 for ocean studies [6]. This led to the launch of many SAR system enabled satellites which became the main requirement data source for many applications. A SAR's inability to distinguish two objects at the same range but from different angles then came into limelight. The solution to this problem was to use two RADARs. This idea, along with the use of phase information paved the way for interferometry [6]. It became possible with two SAR images to obtain distance as well as angular measurements [6].

2.2. InSAR

The use of a SAR system in an interferometric mode to generate topographic maps was first generated by Graham [14] in the year 1974. The efficiency of data collection by aerial photography was found to be hampered by clouds and poor sunlight conditions. Hence, RADAR technology which is used in connection with all-weather electronic systems was used to remove the restrictions posed by aerial photography. The RADAR was expected to perform two functions. First, the image should be presented with sufficient resolution in order to identify the various objects and features to be mapped. Second, a three-dimensional measurement of position of a sufficient number of points to define the terrain surface has to be made. These could be achieved using the synthetic aperture RADAR technology (to obtain fine resolution image of the terrain) and RADAR interferometry (to obtain three-dimensional measurement).

Using interferometric techniques, a high-resolution topographic map of the San Francisco Bay area, of size 11 km by 11 km was successfully derived by Zebker and Goldstein [15] in the year 1986. Two images were obtained using two antennas mounted in the flight direction of the aircraft. A single image (interferogram) was obtained by combining the two images acquired simultaneously with a baseline of 11.1 m. Interference fringes were produced when the two images were combined pixel by pixel which resulted in a single image whose phase at each location was the difference of the two phases of the two original images and whose magnitude was the product of the two original magnitudes. Using some mathematical relations, this data was transformed into a cartographically accurate map of the height of the illuminated terrain.

The repeat-pass method of InSAR with satellite data was first demonstrated by Li and Goldstein [16] in the year 1987. This yielded extremely useful topography information and to illustrate the same a specific data set obtained by the SEASAT SAR was used. The interferograms formed from the data pairs

resembled conventional topographic contours in which the fringes were consistent with the conventional topographic map of the area under study. The paper mainly focused on topography mapping attempted by a conventional SAR with a single antenna in a repeat ground-track orbit.

The application of interferometry using repeat-pass method was also demonstrated by Gabriel and Goldstein [17] in the year 1988. SIR-B data was used on two separate orbits, not exactly parallel but inclined at a small angle to carry out the Interferometric process. This was done in order to restrict the length of the baseline by choosing an imaging site near the crossover point of two orbits. Crossed orbit interferometry has been projected as a useful extension of SAR Interferometric usual methods.

C-band RADAR data was processed to generate rectified topographic maps by Madsen, Zebker and Martin [18] in the year 1993. They developed a new processing scheme which featured motion compensation, absolute phase retrieval and three-dimensional location. The performance of the new processor was evaluated under adverse conditions by testing the processor using data which were acquired using extreme aircraft motion. The digital elevation models derived using conventional optical stereo techniques were compared with the topographic maps generated by the RADAR and thus the accuracy was studied.

Digital Elevation Models (DEMs) are used in many applications such as in topographic mapping, seismic source modelling, rainfall-runoff studies etc. Okeke [4] in his paper showed that InSAR is an established technique of generating high quality DEMs from spaceborne and airborne data. The paper describes the processing steps required for DEM generation using SLC SAR data.

A review of the issues, techniques and applications of SAR interferometry was carried out by Gens and Van Genderen [19]. The article discusses the various potential applications of SAR interferometry such as topographic mapping, digital elevation modelling, slope measurement etc. The paper concludes with a focus on one of the research issues which is the investigation of the influence of the atmosphere which hinders the quality of InSAR data.

2.3. DInSAR

Topography estimation was the main element of interest for the early applications of RADAR interferometry. The voracious experiments conducted with the repeat-pass method of InSAR gave rise to an even more spectacular application - deformation monitoring. This application had its own limitations. The deformation signal mixed with the topographic signal for any effective baseline larger than zero. This gave birth to what is now popularly known as Differential Interferometry or DInSAR. The topographic signal obtained from an interferogram containing topographic information was scaled to the baseline conditions of the interferogram containing the deformation signal and subtracted from it resulting in a differential interferogram also known as DInSAR.

The differential interferometry technique was introduced by Gabriel et.al. [10] in the year 1989. For the first time, a new technique which uses InSAR methods to measure very small changes in the surface of the terrain was demonstrated. This new technique was capable of measuring very small (1 cm) motions of terrain with high resolution over large swaths. Three Seasat observations in the Imperial Valley, California were used to apply this method from which a double-difference interferogram was formed. This interferogram showed clear areas of phase change which were due to the swelling of water-absorbing clays in the scene.

With more and more in-depth exploration of differential interferometric techniques, the concept of the three types of DInSAR: two-pass, three-pass and four-pass took its ascent. The three-pass technique of DInSAR requires three images of the same scene, an external DEM is not necessary. The idea behind this technique is that one of the interferometric pairs includes differential phase contributions and the other pair is used to subtract the corresponding topographic phase contributions. This method of three-pass DInSAR in which three images of the same scene are used to generate a displacement map was demonstrated by Zebker et.al. [20] in the year 1994. The three-pass DInSAR method is described in this paper and is illustrated in the Figure [2.1] below.

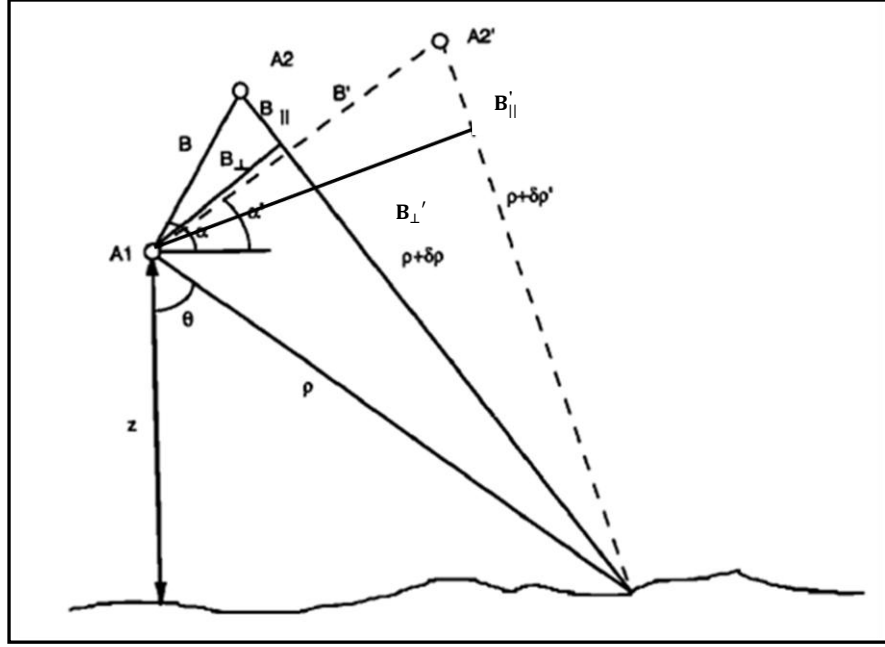


Figure 2.1: Imaging geometry of RADAR

The solid lines in the figure show the RADAR signal paths for the first interferogram pair formed by antennas at locations A_1 and A_2 and the dashed lines show the signal path for the second interferometric pair acquired over the same site with antennas located at positions A_1 and A_2' .

The DInSAR phase measurements are explained with the help of equations as follows

$$\Psi_1 = \frac{4\pi}{\lambda} \rho \quad (2.1)$$

$$\Psi_2 = \frac{4\pi}{\lambda} (\rho + \delta\rho) \quad (2.2)$$

$$\Psi_3 = \frac{4\pi}{\lambda} (\rho + \delta\rho') \quad (2.3)$$

Where, Ψ_1 , Ψ_2 and Ψ_3 are the phases measured at the three platforms to a ground point, ρ , $(\rho + \delta\rho)$ and $(\rho + \delta\rho')$ are the path lengths measured from A_1 , A_2 and A_2' respectively and λ is the wavelength of the RADAR wave.

Therefore, the interferometric phases of the two pairs are given by

$$\Phi = \Psi_1 - \Psi_2 = \frac{4\pi}{\lambda} \delta\rho \quad (2.4)$$

$$\Phi' = \Psi_1 - \Psi_3 = \frac{4\pi}{\lambda} \delta\rho' \quad (2.5)$$

It is clearly seen in the Figure [2.1] that $\delta\rho \approx B_{\parallel}$. Thus the interferometric phases become

$$\Phi = \frac{4\pi}{\lambda} B_{\parallel} = \frac{4\pi}{\lambda} B \sin(\Theta - \alpha) \quad (2.6)$$

Similarly,

$$\Phi' = \frac{4\pi}{\lambda} B'_{\parallel} = \frac{4\pi}{\lambda} B' \sin(\Theta - \alpha') \quad (2.7)$$

Where,

- $B_{\parallel}, B'_{\parallel}$ = component of the baseline parallel to the look direction of the first pair and second pair respectively
- B, B' = baseline length of the first pair and second pair respectively
- Θ = look angle
- α, α' = angle of the baseline with respect to horizontal at the sensor for the first pair and second pair respectively.

Differential RADAR interferometry which is a result of the phase difference of two interferograms is a combination of two approaches: motion sensitivity and sensitivity to topography as given by a sensor temporal change and sensor location change respectively. A map of the coseismic displacement field resulting from the Landers, California, earthquake which occurred on June 28, 1992 is presented here. Three European Remote Sensing satellite (ERS) 1 SAR data sets acquired in April, July and August 1992 were used to generate a high-resolution map of the displacements occurred. The results achieved were found to be more accurate than the previous space studies and their accuracy matched with those obtained by conventional field survey techniques. In this study, from the DEM of the Landers area, the interferogram which contained phase signals from the local topography and from the earthquake displacements was subtracted. The Interferometric fringes obtained represented about 2.8 cm of motion in the RADAR line of sight direction.

DInSAR started gaining recognition due to its deformation mapping capability. Studies on topographic and deformation mapping from all over the world were received with immense interest by the scientific communities. L-band seems to be a well-suited wavelength for long-term DInSAR. This has been presented by Reigber [21] in the year 2003. The first results of airborne DInSAR using the German Aerospace Centre experimental SAR system in the Interferometric repeat-pass mode are presented in this paper. L-band SAR data of vegetated areas were used for the study. An analysis of coherence of the images has been done in this paper. Acceptable coherence over vegetated areas, even after one year, can be provided by SAR backscattering in L-band.

To promote random temporal change detection in relief areas using repeat-pass InSAR coherence imagery, topographic phase in the interferogram has to be removed to facilitate sample coherence

estimation. Such a study has been done by Lee and Liu [22]. Analysis on the effect of topographic phase to degrade coherence estimation is done and a novel method to generate topographic phase-free coherence, called the differential coherence is proposed. The resultant differential coherence image shows improved coherence on terrain slopes.

The principles of DInSAR are also introduced by Yaobin et.al. [9]. The paper focuses on the application of DInSAR in monitoring underground coal mining-induced subsidence. A brief overview of two-pass DInSAR and advanced DInSAR techniques is given in the paper. Two-pass DInSAR unlike three-pass DInSAR uses an interferometric pair and an external DEM. This technique of DInSAR is illustrated in this paper. Underground coal mining activities cause ground subsidence which is a threat to the safety of surface infrastructure of a city and can cause environmental problems. Monitoring the spatial distribution of surface deformation is important as it helps in land-use planning and land reclamation purposes. Hence, DInSAR which can measure Earth surface deformation, capable of obtaining dense information related to deformation is used for monitoring purposes.

The four-pass DInSAR technique to monitor the location and magnitude of ground deformations due to mining activities was applied by Linlin et.al. [23] in the year 2003. This technique of DInSAR requires two pairs of SAR images. From one pair, a DEM is generated which contains the topographic information. The other pair, also known as targeting pair is used to identify the ground deformation formed between the two acquisitions. A pair of C-band images was used to generate DEM and a pair of L-band images was used as the targeting pair in this study. For precise georeferencing purposes, InSAR was integrated with Global Positioning System (GPS). About 20-30 cm of ground deformations was found as a result of DInSAR. Although DInSAR technique was applied, the subsidence was not very clearly visible. Thus, this technique was combined with Geographical Information Systems (GIS) technique to get a clear visibility of the locations of subsidence.

DInSAR has been applied to investigate land subsidence in Jakarta during 2007 and 2008 by Bayuaji et.al. [24]. Advanced Land Observation Satellite (ALOS) Phased Array type L-band Synthetic Aperture Radar (PALSAR) data taken on three different acquisition dates (31 January 2008, 3 February 2008 and 5 November 2008) have been used to observe the land subsidence. The centres of subsidence were successfully located and the subsidence depth and volume around these centres were estimated. The L-band DInSAR method when compared with ground-based GPS measurements produced reasonable results of urban subsidence.

Many works have been done on the crucial step in interferogram determination which is called phase unwrapping. The total phase difference obtained between two points in an interferogram measures many multiples of 2π Burgmann et.al. [2]. This phase difference needs to be determined by counting the number of phase cycles, also known as fringes, between the points. Eineder and Holzner [25], Boncori [12] are some scholars who have worked on phase unwrapping techniques.

As the roots of RADAR interferometry spread widely all over the scientific world, a deeper understanding of its limitations arose. One of the most intractable problems with InSAR is the effect of the refractive atmosphere on the phase of the interferogram. Accuracy in height and displacement is known to be affected by atmospheric propagation. InSAR measurements are affected by the RADAR signals that propagate through the atmosphere. Great efforts have been made to understand the properties of the atmospheric effects on InSAR and to develop methods to mitigate the same.

2.4. Study of atmospheric effects on RADAR interferometry

The atmosphere artefacts were first observed in interferograms by Goldstein [26], Massonnet and Feigl [27] and Zebker et.al. [28]. The atmosphere is divided into many different layers out of which the two major layers troposphere and ionosphere are responsible for the artefacts in the interferograms. The troposphere which is the lowest portion of the Earth's atmosphere contains 99% of water vapour and aerosols. Propagation delays are caused due to air refractivity gradients of the troposphere [7]. The ionosphere which is located at a height of 50 km-1500 km is characterized by free electrons and ions that define the refractive index in this area [29]. The effects of these layers on the phase of an interferogram have been subjected to detailed study in many research works. A review on the works done on the effect of these layers is discussed individually in the sections below.

2.4.1. Tropospheric Effects

Extra delay features on the interferogram were observed by Goldstein [26] in the year 1995 which were the results of turbulent mixing of water vapour and air in the troposphere. A region of Mojave Desert of California was chosen as the study area. The extremely dry desert is regarded as one of the world's most stable areas. The effects of troposphere on topographic accuracy are revealed in this study. Three RADAR observations of the same site were taken for the research purpose. The phase inconsistencies found on the interferogram were the result of water vapour and turbulence. One fringe in the interferogram represented 2.8 cm of one-way time delay. Thus, the accuracy of motion detection and topographic estimation is limited by tropospheric turbulence coupled with water vapour.

Various geophysical phenomena such as displacements on the ground, atmospheric perturbations, and errors in the DEM are recorded in the interference patterns formed by differencing two SAR images. It is necessary to distinguish various types of geophysical signals and to identify the interferometric artefacts. This becomes possible by comparing different pairs of images spanning different intervals of time. This logic was applied by Massonnet and Feigl [27] in the year 1995. To apply this pair-wise logic, SAR images acquired by ERS-1 satellite of the area around the 1992 Landers, California earthquake were used. The signatures of the different geophysical phenomena and interferometric artefacts were identified and separated using the pair-wise logic. A kidney shaped feature consisting of one closed fringe was observed in an interferogram. The reason for the appearance of this feature was a perturbation in the RADAR propagation delay through the atmosphere at the acquisition time.

Phase distortions in RADAR interferograms due to variations in atmospheric water vapour were reported by Zebker et.al. [28] in the year 1997. The main objective of this paper was to examine phase defect caused due to troposphere in data acquired by SIR-C sensor over Hawaii Island and to make an assessment of the impact of troposphere on the performance of space borne interferometric RADAR topographic and surface deformation measurement systems. Zebker developed a model of atmospheric effects in repeat-pass RADAR interferograms. A general assumption has been made in this paper: "The signals propagate at known constant velocity to convert time delays and phase shifts to distance" [28]. When the RADAR signals propagate through the Earth's atmosphere, which has a high refractive index, the velocity is lowered leading to variable delays which affect the observations. The model for path delay is as explained below.

$$\Delta x = (\Delta x)_{dry} + (\Delta x)_{wet} \quad (2.8)$$

Where,

$$(\Delta x)_{dry} = \text{contributions to path length from hydrostatic delay}$$

$(\Delta x)_{\text{wet}}$ = contributions to path length from water vapour

$$\Delta x = 77.6 \times 10^{-5} \int_0^X \frac{P}{T} dx + 3.73 \times 10^{-1} \int_0^X \frac{e}{T^2} dx \quad (2.9)$$

Where,

- Δx = change in effective path length,
- X = total path length through the atmosphere
- P = atmospheric pressure in millibars
- T = temperature in Kelvin
- e = partial pressure of water vapour in millibars

The excess path length depends on P , T and e of troposphere along the propagation path from the sensor to the surface of the Earth and back to the sensor. As the atmospheric delay is independent of wavelength, the longer L-band measurements which derive the most accurate results from highest correlation interferograms are preferred.

The spatial distribution of water vapour is important for climate and meteorological studies. Water vapour mapping is necessary for accurate precipitation forecasts. Water vapour mapping from interferometric RADAR measurements was demonstrated by Hanssen [30] in the year 1999. ERS-1 and ERS-2 data were acquired over the Netherlands and three interferograms were formed. The signature of cumulonimbus cloud could be observed as a localized delay difference in the interferogram. The delay differences were mapped to zenith-integrated precipitable water. A maximum delay difference of 2 mm would be produced with the contribution of liquid water in a cumulus cloud. The areas which showed delay differences more than 30 mm were regarded as precipitation regions. Weather forecasting has become successfully possible due to the readily attainable integrated precipitable water amounts. Much greater accuracy can be achieved in meteorological understanding and forecasting with the proper use of airborne and spaceborne SAR systems.

With the rapidly increasing interest in the field of InSAR, the numerous studies done in this field showed that atmospheric inhomogeneities could act as a major source of error in these measurements.

A standard formula for atmospheric range correction was derived by Saastamoinen [31]

$$\ddot{A}_{S_0} = 0.002277 \sec Z \left[p + \left(\frac{1255}{T} + 0.05 \right) e - B \tan^2 Z \right] + \delta_R \quad (2.10)$$

Where,

- \ddot{A}_{S_0} = range correction in meters
- Z = apparent zenith distance of the satellite
- p = total barometric pressure in millibars
- e = partial pressure of water vapour in millibars
- T = absolute temperature in degree Kelvin
- B, δ = correction quantities

This range correction when subtracted from the observed electromagnetic distance, gives the true measured length of the effective ray path. This model for atmospheric range correction was used in many research works to get error free results.

A simplified form of Saastamoinen model was used by Hanssen and Feijt [32]. A first quantitative evaluation of these effects on InSAR measurements was carried out in this work. The main focus of this work was to estimate the magnitude of phase shifts due to tropospheric effects on interferograms and to suggest some possible solutions to tackle these problems. When a signal propagates through a medium with refractive index unequal to 1, an incremental path length due to the signal delay in the medium will be observed. Through various experimental measurements, the incremental path length can be approximated by integrating the parameters (atmospheric pressure, temperature and partial pressure of water vapour) over the total path length in the troposphere. This incremental path length was estimated using Saastamoinen tropospheric model in this research work. The incremental path length in this model is expressed as a function of pressure, relative humidity, temperature and inclination. The simplified form of Saastamoinen model is as given below

$$\Delta \tilde{n} = 2.277 \times 10^{-3} \frac{P + \left(\frac{1225}{t+273.15} + 0.05 \right) e^{-1.156 \tan^2 \theta}}{\cos \theta} \quad (2.11)$$

Where,

- $\Delta \tilde{n}$ = incremental path length,
- P = total atmospheric pressure in HPa,
- t = temperature in degree Celsius,
- θ = inclination angle and
- e = partial pressure of water vapour

The partial pressure of water vapour can be derived from relative humidity as given below

$$e = \frac{rh}{100} e^{\left(-\frac{372}{165} + 0.213166(t+273.15) - 0.000256908(t+273.15)^2 \right)} \quad (2.12)$$

Where, rh = relative humidity (%)

A SAR interferogram of Groningen area, The Netherlands used for in a case study was evaluated. Meteosat and NOAA-AVHRR imagery were clearly studied to assess the effects of atmosphere on them. Meteorological ground observations of the study area were acquired at the moment of SAR data acquisition. The results of these observations were used to get a first estimation for the parameters in the Saastamoinen model.

The RADAR wave which propagates through the atmosphere follows a straight line. In fact, the ray is bent due to the refractive atmosphere. An assessment of the effects of ray bending on DEM generation has been done by Tarayre and Massonnet [33]. The wave propagation through a refractive medium, interferometric processing and the refractive index of the two layers of the atmosphere: troposphere and ionosphere have been modelled in this paper. The time delay is given by the below equation

$$T = \frac{2}{C} \int_{z_{sat}}^{z_p} \frac{n}{\cos \theta} dz \quad (2.13)$$

Where,

- T = time delay
- C = speed of light
- z = distance from the centre of the Earth to the point

- θ = local incidence angle
 z_{sat} = satellite altitude
 z_p = altitude of the point on the ground

It was concluded that 0.8 cm artefacts are due to neutral atmosphere and 1.2 cm of artefacts are due to ionospheric refraction.

A work by Danklmayer et.al. [8] involves the review and identification of major atmospheric effects on TerraSAR-X images. A review of the ionospheric and tropospheric effects has been presented in this paper. Some of the ionospheric effects on microwave radiation are Faraday rotation (FR), scintillation, refraction, diffraction, phase delays etc. Investigations on FR effect at X-band and L-band have shown the FR at X-band to be 60 times lower than that at L-band. Higher microwave wavelengths and higher electron densities result in intensified effects. Along with the ionospheric effects, the major tropospheric effects which are attenuation and signal delay have also been briefly discussed in this paper. The signal delay due to troposphere can be divided into wet delay and dry delay. The wet delay is affected by variations in water vapour concentration and dry delay is caused due to gaseous nature of the lower part of the atmosphere. The wet delay can reach values up to 0.4 m and dry delay can reach values up to 2.3 m. Huge volumes of data were inspected carefully in order to choose the dataset which emphasized distortions due to atmospheric effects. The ‘‘SIR-C/X-SAR’’ image of tropical rain forest was acquired. The rain-induced heavy-downpour appeared as a black cloud on the X-band image with the C-band and L-band images showing very faint cloud block. Thus, the shorter RADAR wavelengths are unusually affected by heavy rainfall cells.

A number of models to determine the path delay due to tropospheric water vapour have been proposed. Some of the possibilities to improve estimation of tropospheric delays have been investigated by Askne and Nordius [13]. Two new methods were suggested: A model by using two parameters to describe the decrease in temperature with height and the relation between pressure and partial pressure of water vapour respectively and the other model uses temperature and humidity profiles. The two-parameter formula derived for the path delay is as shown below.

$$\Delta L = 10^{-6} \frac{k_1 R_d}{g_m} \left\{ p_s + \left[\frac{k'_2}{k_1(\lambda+1)} + \frac{k_3}{k_1(\lambda+1-\alpha R_d/g_m)T_s} \right] e_s \right\} \quad (2.14)$$

Where,

- ΔL = path delay
 R_d = R/M_d (R = molar gas constant = 8.314J/molK, M_d = molar mass of dry air = 28.9644g/mol)
 g_m = gravity acceleration at the mass centre of a vertical column of atmosphere
 p_s = total surface pressure in millibars
 T_s = Temperature in degree Kelvin
 e_s = partial pressure of water vapour in millibars

The empirical constants,

- k_1 = 77.604 \pm 0.014 K/mbar
 k'_2 = $k_2 - k_1$, k_2 = 64.79 \pm 0.08 K/mbar
 k_3 = (3.776 \pm 0.004) $\times 10^3$ K²/mbar
 λ, α vary for different seasons and latitudes

By knowing the surface values of pressure, temperature and humidity, the temperature and humidity

profiles were estimated. This method can be used to estimate the delay, refraction and attenuation along the ray path.

An extensive comparison between InSAR observations of atmospheric artefacts and meteorological data was carried out by Hanssen et.al. [34]. The interferometric phase variation was explained with the use of atmospheric features derived from sea surface. The observed wind streaks over water areas in the backscatter intensity images were compared with the wave effects observed in the interferograms over the land areas. To derive a combined interferogram two adjacent ERS SAR tandem pairs centered over Flevoland in the Netherlands were used. The phase variation was compared with the meteorological data using ground truth measurements and SAR derived wind speed and direction. With this exploration, it was inferred that SAR backscatter imaging repeat-pass InSAR techniques can be regarded complementary for the analysis of atmospheric dynamics. This is due to the ability of SAR backscatter information over water areas to obtain information on wind direction and the ability of repeat-pass InSAR to detect spatial variations in the refractive index over land inspite of its disability to work on water areas due to temporal decorrelation.

A research work by Boncori [12] in the year 2006 integrates error modeling for InSAR. The statistical modeling of atmospheric refractive index errors is the central part of this work. It is well known that a RADAR wave propagating through the atmosphere is subjected to bending and propagation delay. The effects of bending on RADAR interferometry are negligible when compared to those of propagation delay. Propagation delay results in an excess path length, which is caused by variations of refractivity. This excess path length is given by

$$\Delta R_e = 10^{-6} \int_0^H \frac{N}{\cos\theta} dh \quad (2.15)$$

Where,

- H = vertical distance travelled by the RADAR wave in m
- N = refractivity
- θ = incidence angle
- h = topographic height

The refractivity is calculated from the following equation

$$N = k_1 \frac{P}{T} + \left(k_2 \frac{e}{T} + k_3 \frac{e}{T^2} \right) - 4.028 \times 10^7 \frac{n_e}{f^2} + 1.45 W \quad (2.16)$$

Where,

- k_1 = $77.6 K hP_a^{-1}$
- k_2 = $23.36 K hP_a^{-1}$
- k_3 = $3.75 \times 10^5 K^2 hP_a^{-1}$
- P = total atmospheric pressure (hP_a)
- T = temperature (K)
- e = partial pressure of water vapour (hP_a)
- n_e = electron density (per m^3)
- f = RADAR frequency (H_z)
- W = liquid water content (g/m^3)

The above equation is a combination of four terms. The first term is the hydrostatic delay, the second term is the wet component of refractivity, the third term is due to ionosphere and the fourth term accounts for liquid water in clouds. The atmospheric model which is derived in this thesis work, when considered for all data sets, appeared to bring a realistic contribution to the error estimation.

The properties of atmospheric effects on InSAR and methods for mitigating these effects have been systematically reviewed by Ding et.al. in [5]. Changes in the refractive index of the medium lead to atmospheric artefacts in SAR interferograms. These changes in the refractive index are caused by atmospheric pressure, temperature and water vapour. The effects of pressure and temperature are generally small in magnitude when compared with that of water vapour. The artefacts caused by water vapour are the major dominating atmospheric artefacts in SAR interferograms. The RADAR signals are subjected to propagation delay which is explained in the following equations.

$$\Psi_1 = \frac{4\pi}{\lambda}(L_1 + \Delta L_1) \quad (2.17)$$

$$\Psi_2 = \frac{4\pi}{\lambda}(L_2 + \Delta L_2) \quad (2.18)$$

Where,

Ψ_1	= phase measured during first image acquisition
Ψ_2	= phase measured during second image acquisition
L_1	= slant range during first image acquisition
L_2	= slant range during second image acquisition
λ	= wavelength of the RADAR signal
ΔL_1	= atmospheric propagation delay corresponding to first acquisition
ΔL_2	= atmospheric propagation delay corresponding to second acquisition

From the above equations, the interferometric phase is

$$\Phi = \Psi_1 - \Psi_2 = \frac{4\pi}{\lambda}(L_1 - L_2) + \frac{4\pi}{\lambda}(\Delta L_1 - \Delta L_2) \quad (2.19)$$

Where,

$\frac{4\pi}{\lambda}(L_1 - L_2)$	= topography and surface deformation induced interferometric phase
$\frac{4\pi}{\lambda}(\Delta L_1 - \Delta L_2)$	= atmosphere induced interferometric phase

The term $(\Delta L_1 - \Delta L_2)$ is responsible for errors in InSAR measurements.

Various methods developed to mitigate these atmospheric effects on repeat-pass InSAR have been discussed briefly in this paper.

- a) Correction based on ground meteorological observations
- b) Correction based on GPS observations
- c) Correction based on high-resolution meteorological models
- d) Correction based on MERIS data
- e) Correction based on Correlation analysis
- f) Correction based on pair-wise logic
- g) Correction using stacking method

An atmospheric modelling software tool RSL_APD that accounts for atmospheric path delays was developed by Jehle [29]. Using the knowledge of the contributions of atmosphere to the path delay and models for calculating the path delay, this software tool was developed to calculate pixel based path delays for L to X-band SAR applications. The input parameters vary depending on the accuracy requirements and available measurements of Total Electron Content (TEC), water vapour etc. For SAR systems, the atmospheric delay can add up to 16 m (two way path delay). An example of calculated atmospheric path delay from the developed software was demonstrated on an ENVISAT-Advanced Synthetic Aperture Radar (ASAR) scene. The effects of ionospheric and tropospheric path delays were clearly visible on the example images.

2.4.2. Ionospheric Effects

A complete survey of the potential ionospheric effects on the performance of space-based SAR systems has been carried out by Xu et.al. [35]. Some of the effects of ionosphere are propagation delay, dispersion, refraction, group delay, Faraday rotation, scintillation etc. These effects depend on the integral of the electron density along the ray path also called total electron content (TEC). The path delay in the ionosphere is caused by both TEC variations along the path and travelling ionospheric disturbances (TIDs). Two classes of ionospheric effects on interferograms are long wavelength and short wavelength effects. The long wavelength effects include changes in TEC and short wavelength effects include small-scale TIDs. The ionosphere affects the signal delay proportionately to λ^2 . The path delay due to ionosphere can be paired with phase advance or a decrease in the observed range.

The ionosphere consists of free electrons that are created by the major external source which is the solar ultraviolet radiation. The high-energy electrons from the solar wind ionize the atoms and thus cause an increase in electron density. The electron density varies diurnally, seasonally and geographically. The effects related to TEC and their corresponding units are given in Table 2.1.

Table 2.1: Effects related to TEC

Effects	Units
Faraday rotation	Radians
Group-path delay	Seconds
Phase advance	Radians
Doppler shift	Hertz
Time delay dispersion	Seconds per hertz
Phase dispersion	Radians per hertz

A radio wave may be expressed in terms of five parameters: phase, amplitude, frequency, direction of propagation and polarization. The phases and amplitudes of electromagnetic waves fluctuate when they propagate through a medium which varies randomly in time and space. Waves after two-way propagation suffer some additional effects such as backscattering enhancement and doubling of the variance of phase. These effects and distortions reduce the capacity of space-based RADAR systems. The ionosphere is a dispersive and turbulent medium; thus the RADAR signals propagating through this medium suffer distortion which degrades the detection performance and image quality.

For InSAR, ionospheric phase bias can lead to severe height degradation. Two approaches are mentioned here which can be applied for phase correction.

- a) Split spectrum processing: the phase bias is estimated from each spectrum phase which is obtained by dividing the single spectrum into several spectrum components.

- b) The GPS technique: a global TEC map can be derived using with the aid of GPS information which can be used to estimate phase corrections.

The effective phase-path length P of a RADAR wave is given by

$$P = \int_0^s n dl \quad (2.20)$$

The integral is taken along the ray path. The change in the phase-path length caused due to ionosphere is given by

$$\Delta l = \int_0^s (n - 1) dl \quad (2.21)$$

Where,

Δl	= change in phase-path length
s	= distance travelled by the RADAR wave
n	= refractive index

The above equation represents the one-way delay. It is inferred that Δl is directly proportional to TEC along the path.

The phase refractive index of a RADAR wave in the ionosphere is less than unity which leads to a phase advance. This phase advance $\delta\Phi$ introduced by two-way propagation in the ionosphere is given by

$$\delta\Phi = \frac{2\pi}{\lambda} 2\Delta l \quad (2.22)$$

The ionospheric characteristics change over space and time as it is not a static medium. Hence, to mitigate the degradation of SAR image, detailed information on the structure of the ionosphere may become a necessity.

Many research works have been done to study the characteristics and effects of ionosphere on InSAR. Some of them include works by Liu et.al.[36], Rignot [37], Snoeij et.al.[38].

From the above works, the primary difference between tropospheric and ionospheric effects on InSAR can be inferred. Troposphere leads to an increase in observed range or phase delay whereas ionosphere leads to a decrease in observed range or phase advance.

InSAR which is a powerful technology for observing Earth's surface is significantly affected by the atmosphere as the RADAR waves propagate through it. Great efforts have been made in recent years to avoid the degradation of InSAR-DInSAR measurements due to atmosphere. Many researchers are pursuing their research in this field which is a necessity in a wide number of applications. This work aims at correcting the phase of a three-pass DInSAR. The effects of troposphere and ionosphere are considered and corrected.

3. STUDY AREA

The site chosen for study swathes a part of the state Uttarakhand, formerly Uttaranchal, located in the northern part of India. It covers an area of 4900 km² accommodating a population of approximately 4 lakhs. It lies between 30.32 northernmost latitude - 29.6 southernmost latitude and 78.47 easternmost longitude - 77.62 westernmost longitudes. The major cities that fall within this extent are Haridwar, Rishikesh, Hetampur, Jwalapur, Meerpur and Roorkee. Rajaji national park, one of the main national parks of India, covers a portion of the study site. Other small cities that rest in this area include Manglaur, jwalapur, Narendranagar, Mohand, Lal Dhang etc. All these small cities have their own significance and contribute to the overall development of the state.

3.1. Attributes of the study area

Different land cover types such as agricultural patches, forest areas, mountainous regions, permanent settlement areas and water bodies characterize this area. This region comes under the shivalik range of Himalayas. Nestling in the foothills of Himalayas, it consists of the river Ganges emerging from the mountains to touch the plains. This river along with other minor streams makes way for the practice of agriculture in this region. Hence, lot of agricultural patches can be found which have gained recognition all over the country due to their crop production in a large scale. Agriculture is practiced in the river valleys of this region.

This region is embedded by a dense cover of deciduous forests which make up the Barkot forest range. All through the forests are a wide variety of shrubs and wildflowers. Rajaji national park that encompasses the shivaliks contains tropical and subtropical moist broadleaf forests. The forest ecosystems of this park are quite varied and diverse. The permanent vegetation of this park can be grouped into the following types.

- Sal forest
- Mixed forest
- Riverine forest
- Scrub forest
- Grassland
- Sub-tropical pine forest

Inhabiting the dense green jungles are an impressive array of creatures consisting of 23 species of mammals including tigers, leopards, deer, jungle cat, wild boar and sloth bear. This park has the largest population of elephants.

Climatic conditions of this region are extreme and erratic. Summers start in late March and go on till early July with an average temperature of 28°C which rises up to 44°C. The monsoon starts in early July and goes on till October. The total annual rainfall is about 2600 mm. Winter starts in December with a temperature of 24°C and falls to a freezing temperature of 5°C.

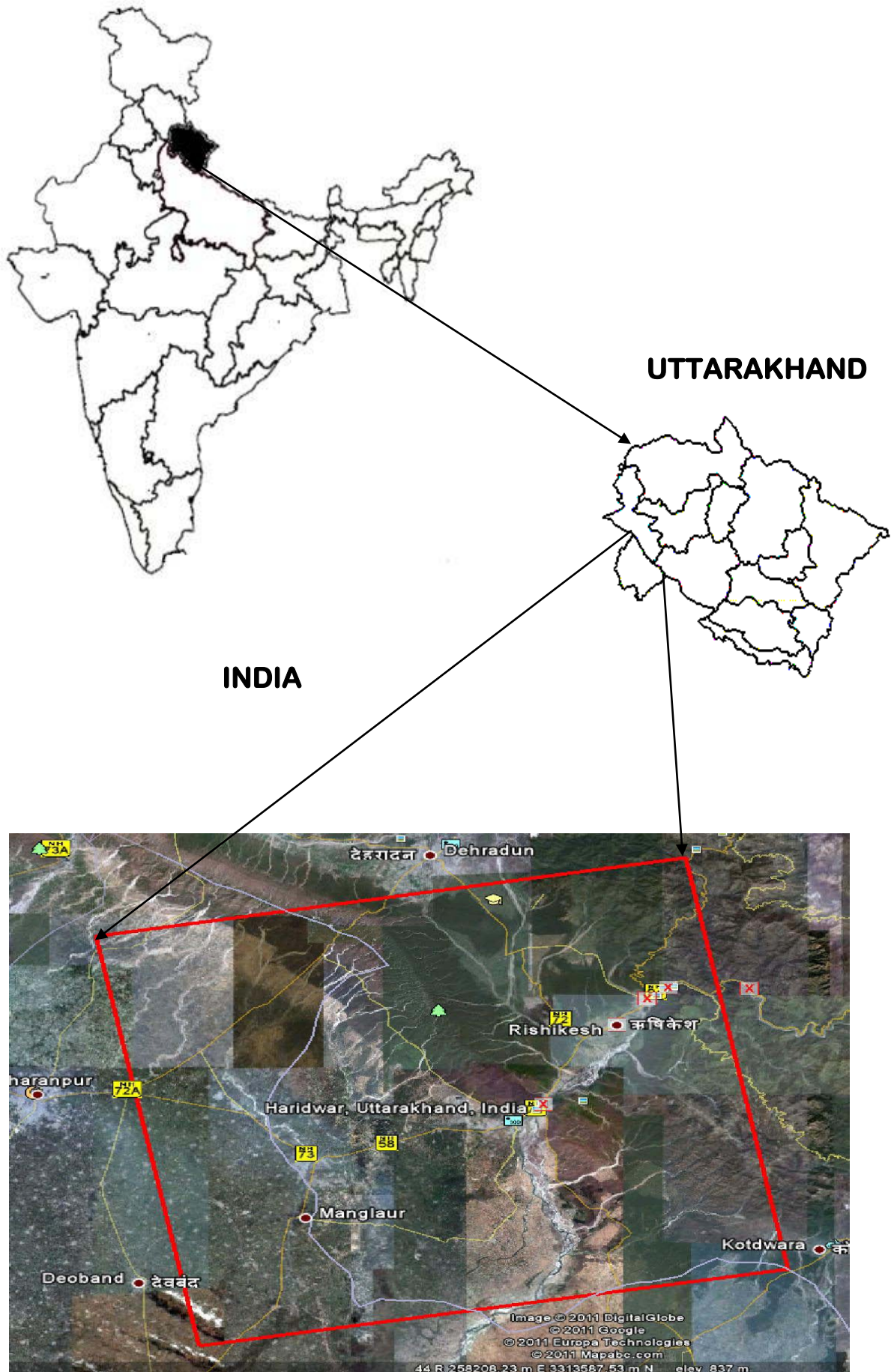


Figure 3.1: Location of the study area (Google image)

3.2. Scientific importance of the study area

This area is chosen for study particularly because of its varied land cover types. Different scatterers can be found which help in the study. The dense deciduous forests of Rajaji national park and Barkot forest range illustrate volume scattering. Permanent scatterers like buildings and mountains act as corner reflectors for the L-band RADAR wave. The water bodies having a smooth surface form the specular reflectors and the agricultural lands during crop growth act as volume scatterers and when plain act as a smooth surface for specular reflectance. All these properties put together make the area a complete package to undergo research work.

This region with a diverse combination of all characteristics can be regarded as the Land of nature's beauty embedding in it all the terrain types, water bodies amidst the great Himalayan Mountains. The exact location of this region is shown in the Figure [3.1]. The scene boundary of the region is mentioned in the Table 3.1 below.

Table 3.1: Scene Boundary

Latitude	Longitude
30.2033	77.6216
29.6006	77.7501
29.7142	78.469
30.3166	78.345

4. MATERIALS AND METHODS

The approach adopted in this research work is shown in the Figure [4.1] below

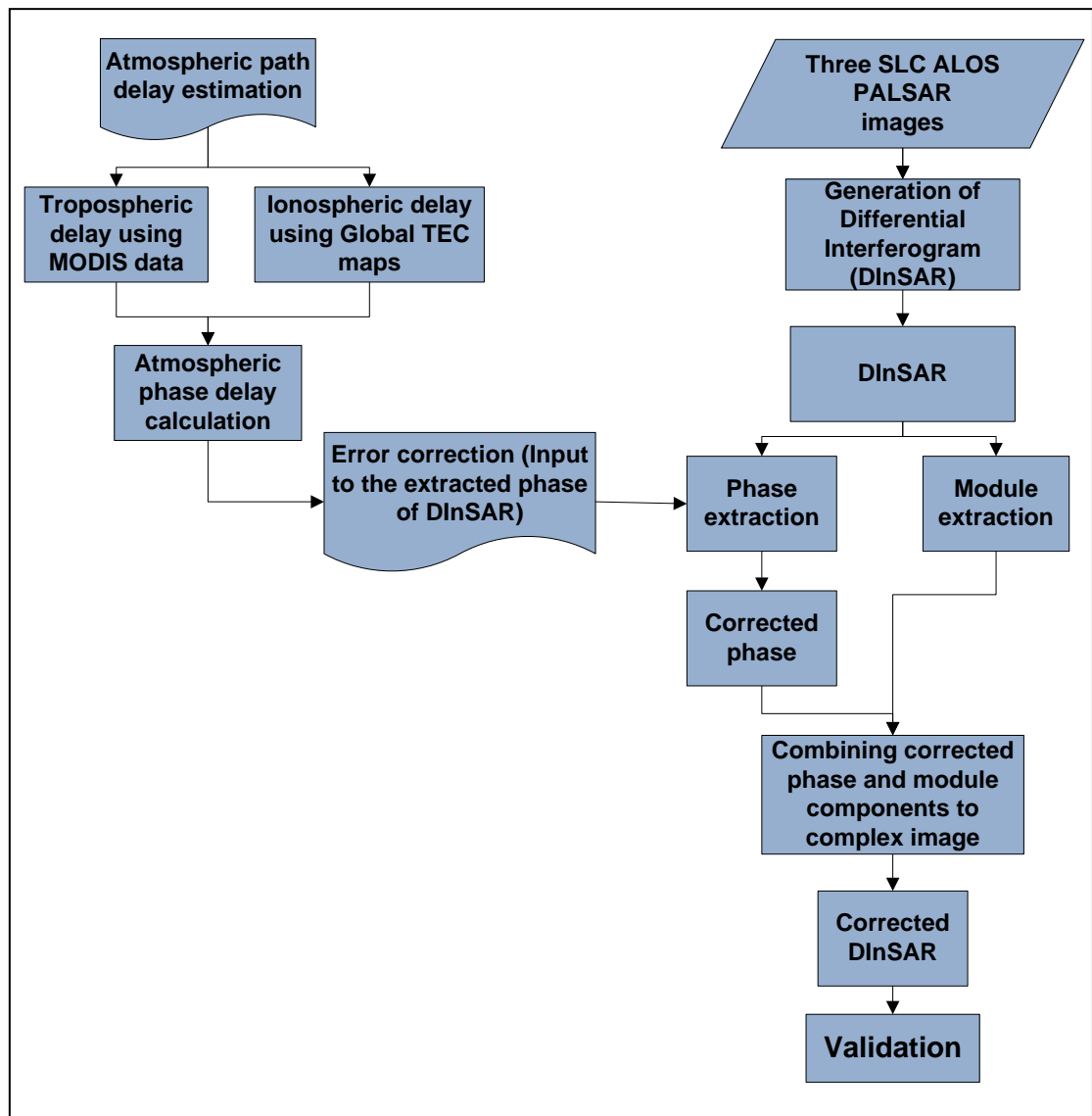


Figure 4.1: Flow Diagram of Methodology

This chapter is divided into the following sections to give an in-depth explanation of the flow diagram of methodology

- Materials
- Effects of atmospheric propagation

- Generation of DInSAR
- Phase correction

4.1. Materials

The two processes that are generation of DInSAR and calculation of atmospheric path delay require two different data sets. DInSAR is generated using three ALOS PALSAR SLC images acquired on the same site. To calculate the tropospheric path delay, the Moderate Resolution Imaging Spectroradiometer (MODIS) data acquired on the same study area is used. MODIS sensor is carried on two satellites that provide complete daily coverage of the Earth. It is possible to obtain images in the morning (Terra satellite) and afternoon (Aqua satellite) for any particular location [39]. The Terra MODIS was launched into space in December 1999 as part of National Aeronautics and Space Administration (NASA) Earth Observing System platform. Aqua MODIS was launched in May 2002. MODIS aims at providing a series of global observations of the Earth's land, oceans and atmosphere in the visible and infrared regions of the spectrum. A brief overview of the MODIS products is given below.

- MODIS is a 36 band spectrometer available with three different spatial resolutions: 250 m, 500 m and 1000 m. The resolution varies for different MODIS products.
- MODIS products are available at different levels.
- Individual daily MODIS scenes are available as MODIS level 1 products for any part of the Earth, everyday.
- MODIS level 2 products cover the atmosphere and land products.
- MODIS data can be directly downloaded from the internet as they are freely available.
- The MODIS product data are provided in the sinusoidal projection.
- The MODIS files are downloaded in Hierarchical Data Format – Earth Observing System (HDF-EOS) format.
- The MODIS cloud product is obtained with a variation of 40 hPa for pressure band and the temperature using this product has a 5 degree centigrade tolerance [40].

The HDF formatted MODIS files once downloaded are reprojected to the projection being used in the work. MODIS cloud product with the name convention MOD06 for three dates mentioned in the Table [4.1] has been used in this work from which the temperature and pressure bands required for path delay calculation from all the three images are extracted.

Details of the datasets are given in Table [4.1].

Table 4.1: Dataset

ALOS PALSAR			
Serial No.	1 (Master image)	2 (Slave image)	3 (Slave image)
Source	ALOS	ALOS	ALOS
Sensor	PALSAR	PALSAR	PALSAR
Data Center	PALSAR GDS (Ground Data System)	PALSAR GDS (Ground Data System)	PALSAR GDS (Ground Data System)
Pattern	Fine Mode/HH+HV	Fine Mode/HH+HV	Fine Mode/HH+HV
Offnadir angle	34.3	34.3	34.3
Incident angle	38.7	38.7	38.7
Orbit No.	23407	24078	24749
Path No.	523	523	523
Start Date (yyyy/mm/dd)/ Time (HH:MM:SS)	2010/06/16 17:19:41	2010/08/01 17:19:12	2010/09/16 17:18:37
Center			

Date (yyyy/mm/dd)/ Time (HH:MM:SS)	2010/06/16 17:19:46	2010/08/01 17:19:17	2010/09/16 17:18:42
End Date (yyyy/mm/dd)/ Time (HH:MM:SS)	2010/06/16 17:19:51	2010/08/01 17:19:22	2010/09/16 17:18:47
Pixel Spacing In Range In Azimuth	14.983805 3.169626	14.983805 3.169628	14.983805 3.176409
MODIS			
Product	Cloud Product Terra	Cloud Product Terra	Cloud Product Terra
Pixel Size	1000 m	1000 m	1000 m
Native Projection	Geographic Lat/Lon	Geographic Lat/Lon	Geographic Lat/Lon
a)Reprojected to b)Datum	UTM Zone 44 North WGS-84	UTM Zone 44 North WGS-84	UTM Zone 44 North WGS-84
Acquisition Date (yyyy/mm/dd)	2010/06/16	2010/08/01	2010/09/16
Acquisition Start Time (HH:MM:SS)	16:20:00	16:35:00	16:45:00

The extent covered by the images is also given in tabular form in table [4.2] and the exact scene boundary is shown in Table [3.1].

Table 4.2: Dataset extent

Latitude at the scene centre	29.9605
Longitude at the scene centre	78.0547
Northernmost Latitude	30.3166
Southernmost Latitude	29.6006
Easternmost Longitude	78.469
Westernmost Longitude	77.6216

4.2. Effects of Atmospheric Propagation

4.2.1. Introduction to the Earth's atmosphere

The atmosphere of the Earth is a mixture of discrete gases, each having its own physical properties, containing tiny suspended solid and liquid particles. It consists of definite layers having varying characteristics of temperature and combination of gases. The atmosphere is divided into a series of layers namely troposphere, stratosphere, mesosphere, thermosphere and exosphere. The outer portion of the mesosphere and the entire thermosphere are also referred to as the ionosphere. Large concentrations of ions and free electrons exist in this region. Among the different layers, troposphere and ionosphere are mainly responsible for RADAR signal delay. The microwave delays in the neutral atmosphere

(troposphere, tropopause and stratosphere) are induced due to the refractive index of the layer which arises due to the presence of gases, water vapour and cloud. Since 80% of atmosphere's mass is found in the troposphere, the effect due to neutral atmosphere is therefore referred to as the tropospheric effect. The RADAR wave crosses these atmospheric layers twice. These layers which have variable refractive indices cause propagation delays resulting in an excess path length. This section is about the estimation of troposphere and ionosphere induced range errors.

4.2.2. Troposphere case

Troposphere is the lowermost layer of the atmosphere. This layer is regarded as the most important layer because almost all of the weather events such as fog, cloud, dew, frost etc., occur in this layer. The average height of this layer is about 16 km over the equator and 6 km over the poles [41]. The signal propagation in the neutral atmosphere (troposphere) depends on temperature, pressure and water vapour. The refractive index is the factor that describes the variability of the troposphere [42]; it decreases with altitude. For the Earth's neutral atmosphere, the refractive index is always slightly greater than one. A signal propagating in a medium with a refractive index unequal to one, experiences an incremental path length due to the signal delay in the medium. Significant contribution to the excess path delay is due to the presence of water vapour. This two-way incremental path length ΔR_e (m) can be approximated by integrating the parameters (temperature, pressure and partial pressure of water vapour) over the total path length in the troposphere [32].

$$\Delta R_e = 2 \times 10^{-6} \int_0^H \frac{N}{\cos\Theta} dh \quad (3.1)$$

Where,

H	= vertical distance travelled by the RADAR wave in m
N	= refractivity
Θ	= incidence angle
h	= topographic height

The tropospheric refractivity depends on the pressure, temperature and partial pressure of water vapour.

The formula used to calculate refractivity (N) as given in [43]

$$N = 77.6 \times \frac{P}{T} - 5.6 \times \frac{e}{T} + 0.375 \times 10^6 \times \frac{e}{T^2} \quad (3.2)$$

Where,

P	= atmospheric pressure in hP_a
T	= temperature in K
e	= partial pressure of water vapour in hP_a

The partial pressure of water vapour is derived from [44] as

$$\begin{aligned} e = 0.01 \times \exp[-2991.2729 \times t^{-2} - 6017.0128 \times t^{-1} \\ + 18.87643854 - 0.028354721 \times t + 0.17838301 \\ \times 10^{-4} \times t^{-2} - 0.84150417 \times 10^{-9} \times t^3 \\ + 0.44412543 \times 10^{-12} \times t^4 + 2.858487 \times \ln(t)] \end{aligned} \quad (3.3)$$

Where,

- e = partial pressure of water vapour in hecto pascals, hPa
 t = temperature in Kelvin, K

The above equations are applied with the extracted pressure and temperature bands of the MODIS images resulting in one image indicating the tropospheric path delay.

4.3. Ionospheric case

The ionosphere extending from a height of 50 km to 1500 km above the Earth's surface is characterized by free electrons which are caused due to external sources like solar radiation. The number of free electrons in the ionosphere is represented by electron density, in electrons per m^3 . RADAR signals travelling through the ionosphere are delayed along their paths by interactions with these free electrons. Thus, the ionospheric delay can be regarded as a path integral through the ionospheric electron density. This integral is known as the Total Electron Content (TEC) having dimension electrons per m^2 . The TEC values vary between $0 m^{-2}$ at night to $20 \times 10^6 m^{-2}$ at the solar cycle minimum to $100 \times 10^{16} m^{-2}$ at the solar maximum.

The ionosphere is divided into a number of layers D, E, F1 and F2, each having different characteristics. The D (80 - 100 km) layer is weakly ionized as it receives only a minor part of solar radiation. The E-layer (100 - 140 km) has little more ionization and at night it fades into F1 layer. The F1 and F2 layers located at 140 - 200 km and 200 - 400 km respectively are ionized strongly and TEC is more in this layer. The TEC can be determined using vertical TEC maps available. The ionospheric maps show hourly change in TEC. The global TEC map produced by the Centre for Orbit Determination in Europe (CODE) is shown in Figure [4.2] below.

At CODE, Global Ionospheric Maps (GIMs) are generated on a daily basis [45][46]. Since 1996, CODE has been producing GIMs from GPS tracking data. In the figure below, the red curve shows the mean TEC, a trend function is plotted in blue and the black dots indicate the daily average mean TEC. The daily mean TEC for the months of master, slave 1 and slave 2 image acquisitions are derived from the above shown map. The two-way path delay (Δs) occurred while the RADAR wave propagates through the ionosphere as given by [29][47] is

$$\Delta s = 2 \times K \times \frac{TEC}{f^2 \cos \alpha_{offnadir}} \quad (3.4)$$

Where,

- K = refractivity constant = $-40.28 (m^3 / s^2)$
 f = frequency of the L-band wave = 1.276 GHz
 $\alpha_{offnadir}$ = Satellite Offnadir angle = 34.3 degrees
TEC = total electron content derived from the GIM.

The sign of the refractivity constant (K) is negative indicating an increase phase advance [6]. The TEC map is available with an accuracy of approximately 0.8TECU [48].

CODE GIM time series from 01-Jan-1995 to 22-Mar-2011

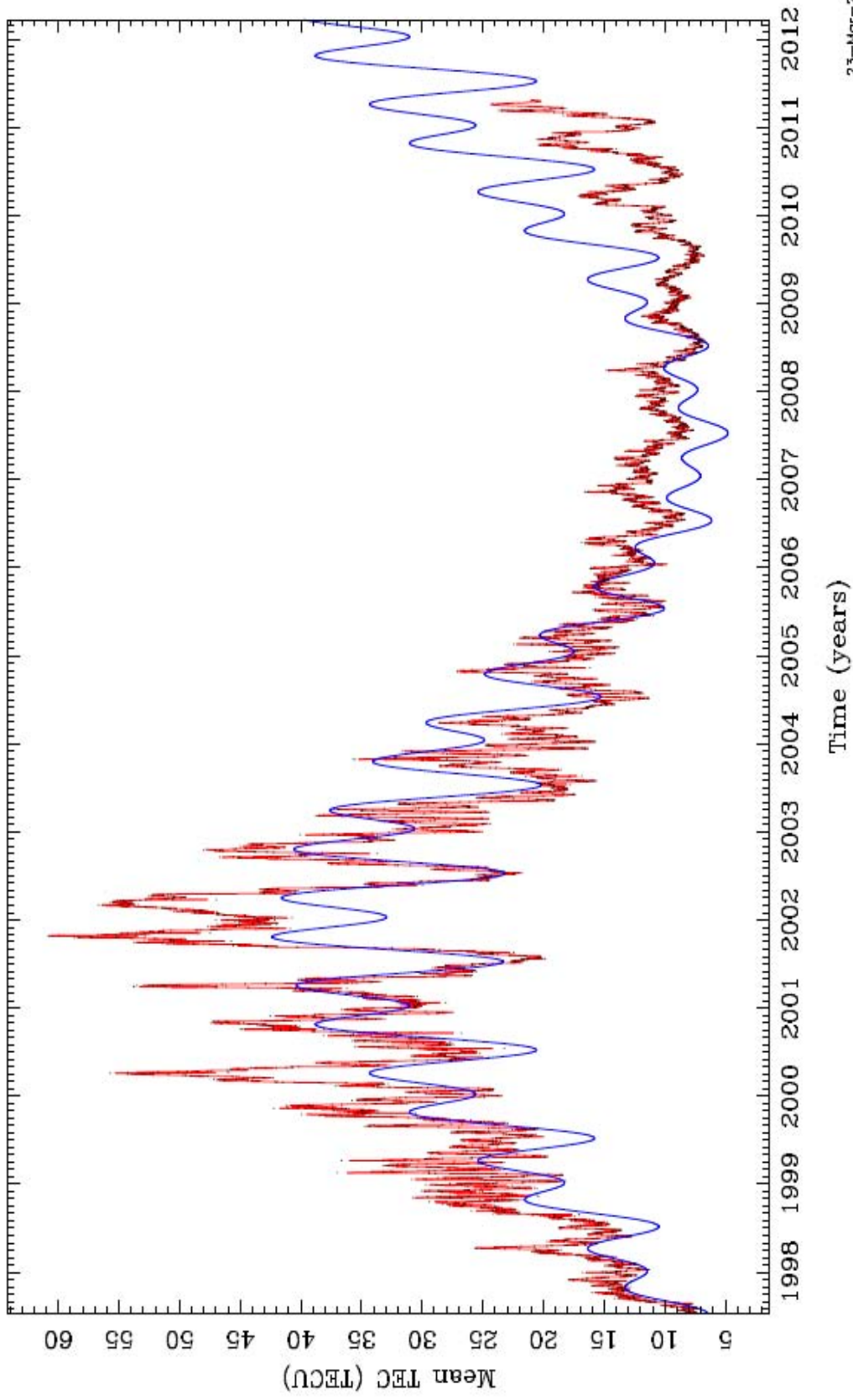


Figure 4.2: TEC map showing yearly and monthly TEC variations

The total path delay is given by

$$\text{Total Path delay (m)} = \text{Tropospheric delay (m)} + \text{Ionospheric delay (m)}$$

The images on which the total path delay has been calculated are shown in Figure [4.3], Figure [4.4] and Figure [4.5] below.

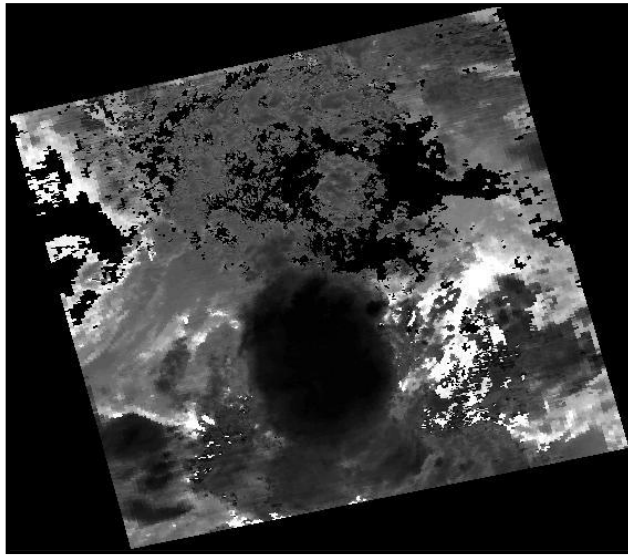


Figure 4.3: Master Image on which total path delay is calculated

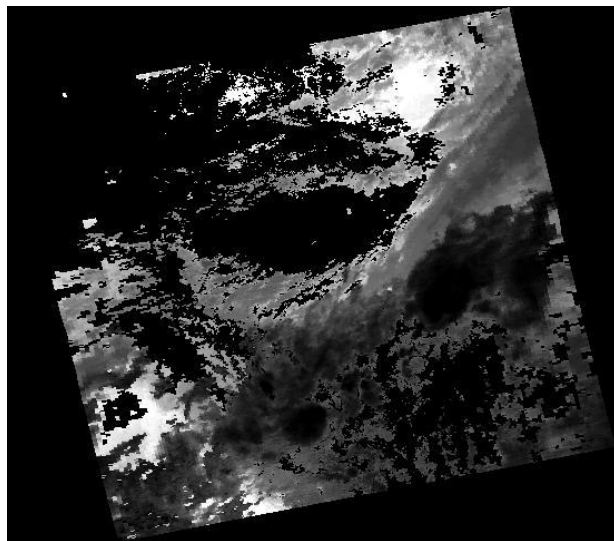


Figure 4.4: Slave image 1 on which total path delay is calculated

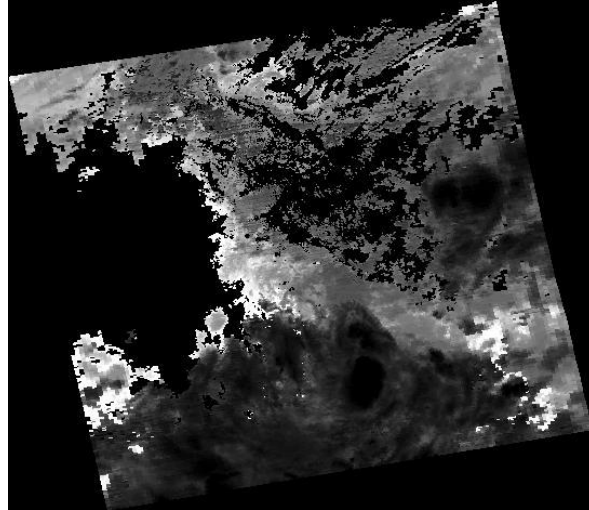


Figure 4.5: Slave image 2 on which total path delay is calculated

4.4. Generation of DInSAR

The three-pass DInSAR is generated using three ALOS PALSAR SLC images. This section describes the technique of three-pass DInSAR generation.

The differential interferometric processing aims at separating the topographic and displacement term in an interferogram. The topographic phase has to be removed to identify the displacement component. The three-pass DInSAR is based on three SAR images from which two interferometric pairs are formed having one master image in common. One of the pairs (topo-pair) is used to estimate the topographic phase which is considered to be the reference pair. The larger the perpendicular baseline, the more is the sensitivity of the interferogram phase to topography [49]. Hence, the topo-pair should be acquired with a short acquisition time interval and a large interferometric baseline. This pair does not include the displacement (if any) to be investigated. The other pair (defo-pair) in general consists of one image before and one after the coherent displacement. This pair should be acquired with a baseline as small as possible. The interferometric pairs used are mentioned below in tabular form in Table [4.3].

Table 4.3: Interferometric pairs

Topo-pair (first pair)	yyyy-mm-dd	Defo-pair (second pair)	yyyy-mm-dd
Master image:	2010-06-16	Master image:	2010-06-16
Slave image 1:	2010-08-01	Slave image 2:	2010-09-16

The different steps involved in the generation of DInSAR are explained in the below sections.

4.4.1. Image Coregistration

Depending on the start-stop times of a particular section in the orbits, arises a possibility of along-track shift between the two SAR images. Therefore, the sub-pixel registration of both the images is strictly required in the processing of interferometric data [6]. Coregistration is the process of geometrical transformation of images which insures that corresponding pixels of different images map the same area [50]. When multiple images cover the same region and operations such as image ratio and similar processes are required in slant/ground range geometry, SAR images must be coregistered. Coregistration in simple terms can be elucidated as the process of superimposing, in the slant range geometry, two or

more SAR images which have the same acquisition geometry. The computation of the interferogram first requires a coregistration step so that the corresponding pixels in the two images perfectly match. All the information enclosed in the SLC to be resampled have to be preserved. Hence, the accuracy in the coregistering operations must be at sub-pixel level.

Coregistration typically consists of computing the offsets between the two SLC images [51]. One of the images is resampled to match with the reference image. These offsets are then used to determine the coefficients of the interpolation function which are required for the resampling. The offsets between the two SLC images are computed using orbit data or by defining common points in the image by visual inspection [6]. Once the offsets are determined, resampling is applied to fit the reference image.

The RADAR sensor measures the distance between two objects and the distances of objects from the satellites along the slant range [52]. Objects in the near-range appear to be compressed relative to the far-range due to the slant-range distortion. Thus the image is corrupted and results in the variation of captured image scale from near- to far-range. By converting the slant-range image into ground-range, this effect is removed. The horizontal distance along the ground for each corresponding point measured in the slant-range distance is the ground-range [52].

The ground-range resolution in range is given by [1]

$$\textit{Ground – range resolution} = \frac{c\tau}{2} \frac{1}{\sin\theta} \quad (3.5)$$

Where,

c	= speed of light
τ	= pulse length
θ	= look angle

A high-resolution, very speckled SLC image product is produced by the SAR signal processor which uses the full synthetic aperture and the complete data history. Hence, these images are processed with multilook processing to generate square pixels and improve the radiometric resolution. This results in degradation of spatial resolution. A function of pixel spacing in azimuth direction, pixel spacing in slant range and incidence angle defines the number of looks [53]. Approximately squared pixels in obtained in the multilooked image considering the ground-range resolution and the pixel spacing in azimuth. The image statistics are used to calculate the number of looks. To generate a multilook image, appropriate factors as the number of looks in the azimuth and range directions are then selected.

4.4.2. Multibaseline Estimation

Information about the baseline values and the acquisition time distance in a multi-temporal SAR acquisition series is obtained in this process. The baseline values for all possible interferometric pair combinations are obtained.

The interferogram generation can be achieved only when the ground reflectivity attained with two antennae in the repeat-pass mode overlap. When the perpendicular component of the baseline increases beyond a limit known as the critical baseline, phase information is not preserved and coherence is lost which makes interferometry impossible. The critical normal baseline as given in [53] is calculated by the following relation

$$B_{n,cr} = \frac{\lambda R \tan(\Theta)}{2 R_r} \quad (3.6)$$

Where,

- λ = wavelength
- R = range distance
- R_r = pixel spacing in range direction
- Θ = incidence angle

Following Table [4.4] gives the information about the normal baseline values for all interferometric pair combinations obtained from this process.

Table 4.4: Normal Baseline values for all possible interferometric pairs

MASTER IMAGE: 2010-06-16 / HH_PASL1101006161719461010150007_slc	
2010-06-16 / HH_PASL1101006161719461010150007_slc	[Baseline = 0m / Days = 0]
2010-08-01 / HH_PASL1101008011719171010150008_slc	[Baseline = 254.41m / Days = 46]
2010-09-16 / HH_PASL1101009161718421010150009_slc	[Baseline = 159.551m / Days = 92]
MASTER IMAGE: 2010-08-01 / HH_PASL1101008011719171010150008_slc	
2010-06-16 / HH_PASL1101006161719461010150007_slc	[Baseline = -254.41m / Days = -46]
2010-08-01 / HH_PASL1101008011719171010150008_slc	[Baseline = 0m / Days = 0]
2010-09-16 / HH_PASL1101009161718421010150009_slc	[Baseline = -117.494m / Days = 46]
MASTER IMAGE: 2010-09-16 / HH_PASL1101009161718421010150009_slc	
2010-06-16 / HH_PASL1101006161719461010150007_slc	[Baseline = -159.551m / Days = -9]
2010-08-01 / HH_PASL1101008011719171010150008_slc	[Baseline = 117.494m / Days = -46]
2010-09-16 / HH_PASL1101009161718421010150009_slc	[Baseline = 0m / Days = 0]

The critical baseline information is obtained from the baseline estimation process in which the baseline values are obtained for the individual input pair. The critical baseline values obtained for the two pairs are given in Table [4.5]. For ALOS PALSAR FBD data, the critical baseline values can go up to 6.5 km to 9.6 km [54].

Table 4.5: Critical Baseline values

Image pairs	Master image: 2010-06-16 Slave image 1: 2010-08-01	Master image: 2010-06-16 Slave image 2: 2010-09-16
Critical Baseline (m)	7669.129	7669.129

4.4.3. Interferogram Generation

The SAR SLC image is a two-dimensional matrix carrying amplitude and a phase associated with each pixel of the image [49]. The amplitude is a measure of target reflectivity and surface parameters. The phase encodes changes at the surface and also a term proportional to the two way range from the platform to the ground. The ground surface represented by a pixel contains hundreds of individual target elements carrying different complex reflection coefficient that contribute to the phase. The resultant phase does not

form a meaningful parameter as it is dependent on the sum of hundreds of complex numbers. When two different images of the same target are compared, phases become meaningful. Hence, to deduce meaningful information from the phase, repeat pass acquisition is made from which a correlation between the phases of corresponding image pixels is established. The phases of the two images are differenced and from this difference the height of the pixel in relation to the altitude of the RADAR can be determined [55].

The interferogram generation requires the pixel to pixel computation of the Hermitian product of the two coregistered SAR images. From [11], the interferogram for the whole scene is represented by

$$v_I = u_m \times u_s^* \quad (3.7)$$

Where u_m and u_s represent the master and slave image respectively and u_s^* represents the complex conjugated slave image.

The phase of the interferogram which is the difference between the phase of the master and that of the slave is represented [53] as

$$\Phi = \tan^{-1} \left(\frac{\text{Imag}(I)}{\text{Real}(I)} \right) \quad (3.8)$$

Where, $\text{Imag}(I)$ and $\text{Real}(I)$ are the imaginary and real parts of the interferogram respectively.

The RADAR imaging geometry is explained in the Figure 2.1. Equations 2.6 and 2.7 denote the interferometric phase of both the interferograms generated from the three SLC images.

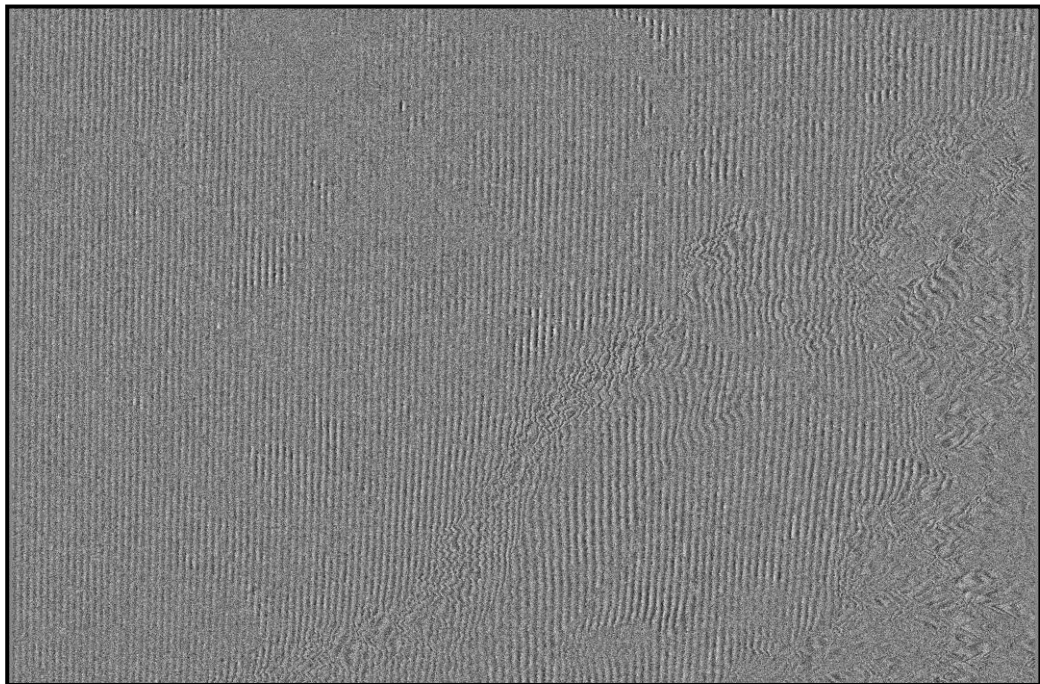


Figure 4.6: Interferogram of first image pair (Master image and Slave image 1)

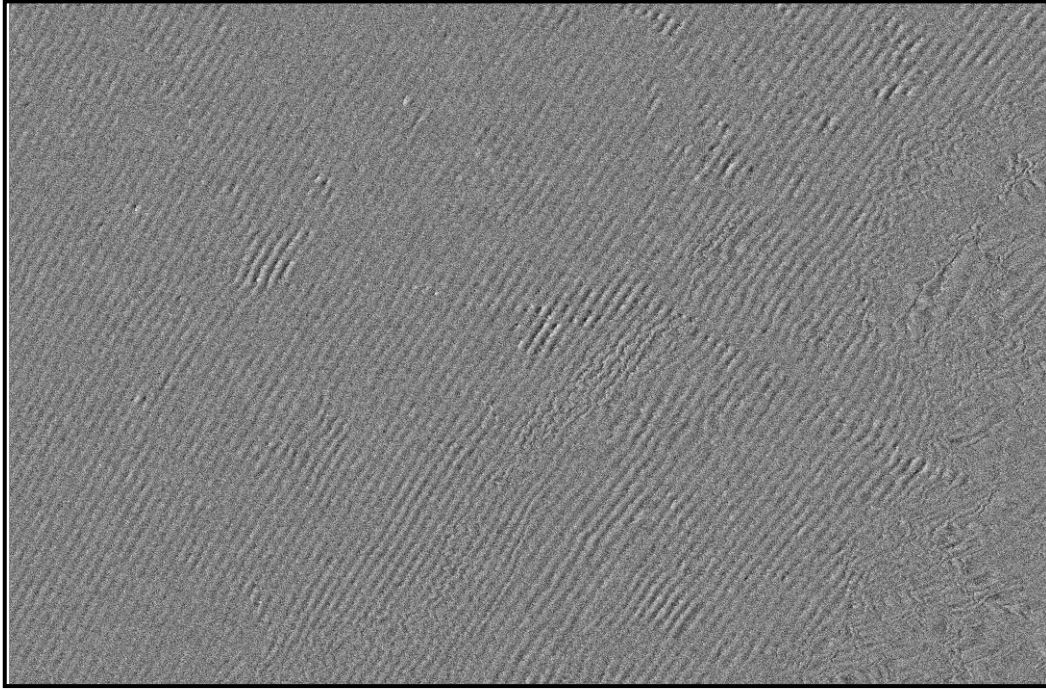


Figure 4.7: Interferogram of second image pair (Master image and Slave image 2)

Figure [4.6] and Figure [4.7] show the interferograms generated for the two SAR image pairs.

4.4.4. Interferogram Flattening

The topographic fringes are overlaid by the fringe pattern caused by the flat Earth [55]. The flattening process removes the fringe and phase effects due to the shape of the Earth ellipsoid. This leaves the interferogram with fringes only related to changes in elevation (as well as noise, atmosphere and surface displacement if any). In this step, the topographic phase is removed from the displacement/residual phase. From Figure [2.1] the phase corrected for the curved Earth effect is given by [20]

$$\Phi_{flat} = \frac{4\pi}{\lambda} [B \sin(\theta - \alpha) - B \sin(\theta_0 - \alpha)] \quad (3.9)$$

$$\Phi'_{flat} = \frac{4\pi}{\lambda} [B' \sin(\theta - \alpha) - B' \sin(\theta_0 - \alpha)] \quad (3.10)$$

Where,

θ_0 = look angle to each point in the image assuming zero local height

From the three SLC images, two flattened interferograms were generated. The following Figure [4.8] and Figure [4.9] show the generated flattened interferograms.

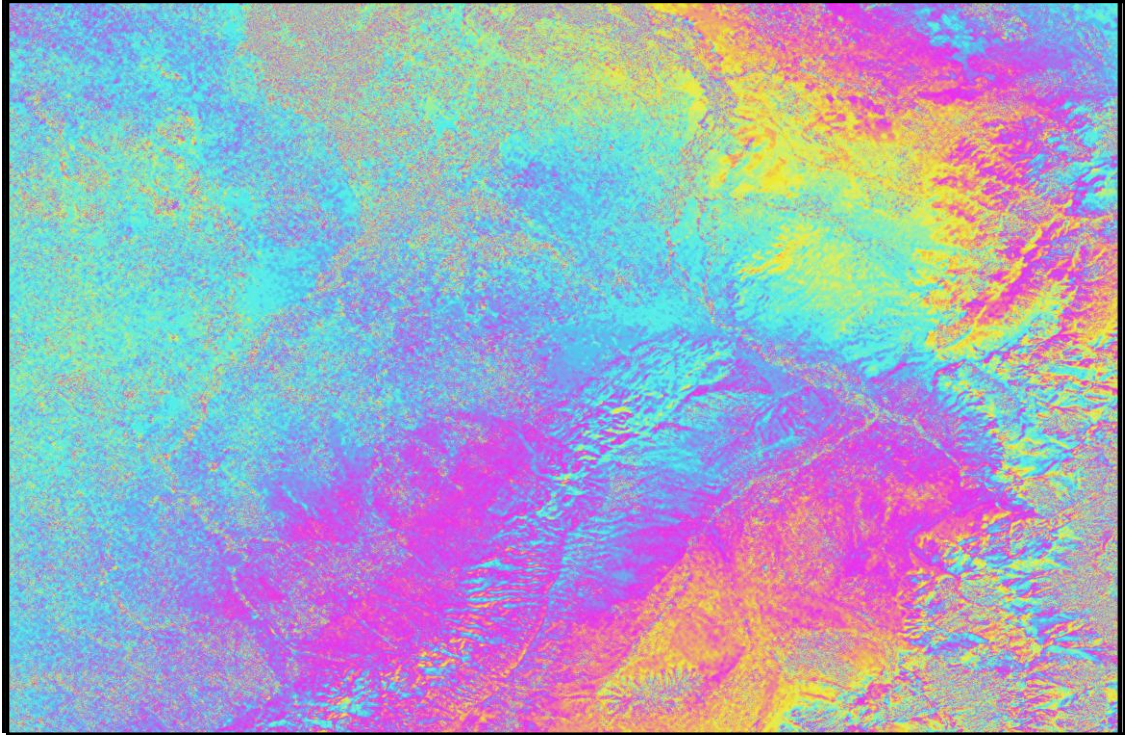


Figure 4.8: Flattened interferogram generated from the first pair (Master image and Slave image 1)

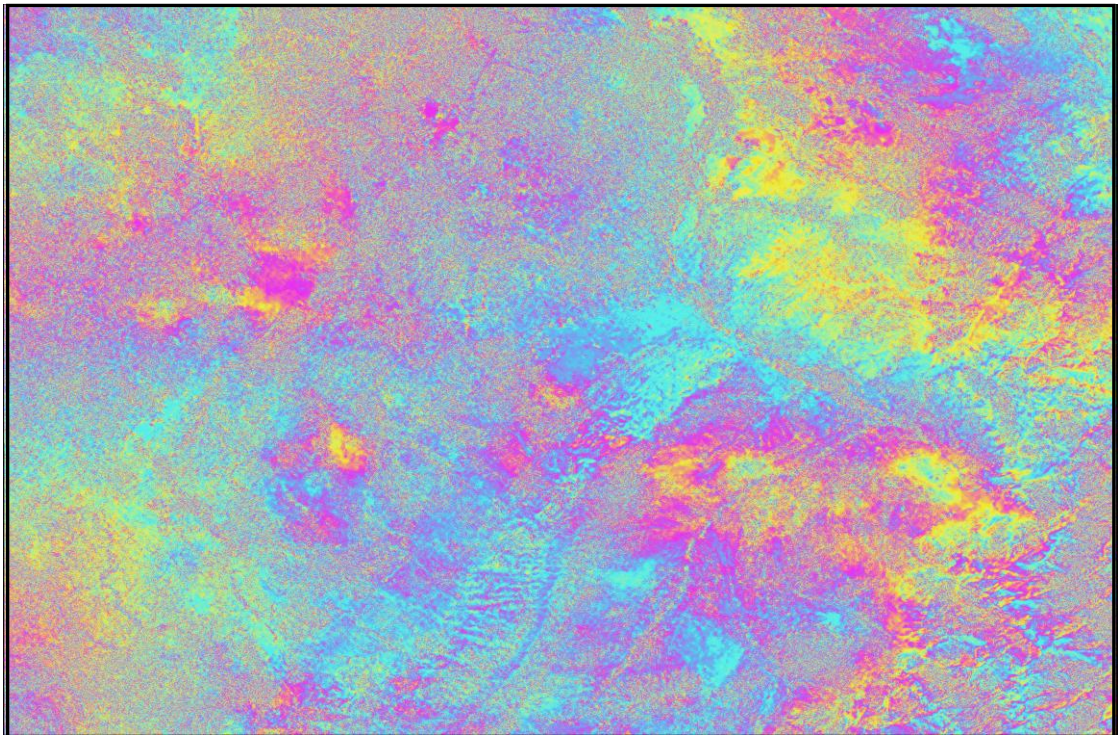


Figure 4.9: Flattened interferogram generated from the second pair (Master image and Slave image 2)

4.4.5. Interferogram Adaptive Filter and Coherence Generation – Boxcar Window

Filtering of flattened interferogram results in reduced noise smoothed interferogram phase. In this step, the Coherence, which is an indicator of the phase quality, is also generated.

The degree of similarity between the two images is known as Coherence [6]. An approach to measure the interferometric complex coherence as expressed in [1] is

$$\Upsilon = \frac{\sum_N P_1 \cdot P_2^*}{\sqrt{\sum_N |P_1|^2 \sum_N |P_2|^2}} \quad (3.11)$$

Where,

- N = number of pixels in the N-sample estimation window
- P_1 = complex SAR image (Master)
- P_2 = complex SAR image (Slave)
- P_2^* = complex conjugate of slave image

The pixel value of a coherence image ranges between 0 and 1. Areas of high coherence between the two images show a pixel value of 1 and areas of low coherence show a pixel value of 0. Coherence is computed using a sliding window. The window slides from pixel to pixel, for each pixel the coherence is computed using the above equation. A window of size 3×3 is used in this work.

The coherence product serves two purposes

- a) Determination of the quality of the measurement (Interferometric phase). To derive reliable phase measurements, InSAR pairs with low coherence should not be used.
- b) Extraction of thematic information related to ground features properties and their temporal changes.

There are several factors which lead to a loss of coherence. As mentioned in [19], few of them are

- a) Different atmospheric conditions during the acquisition of the images
- b) Processing errors in phase
- c) Changes in the position, properties of the object between the data acquisition
- d) Different viewing positions.

The coherence images are generated from the filtered interferogram. The two coherence images generated from the interferometric pairs are shown in Figure [4.10] and Figure [4.11] below.

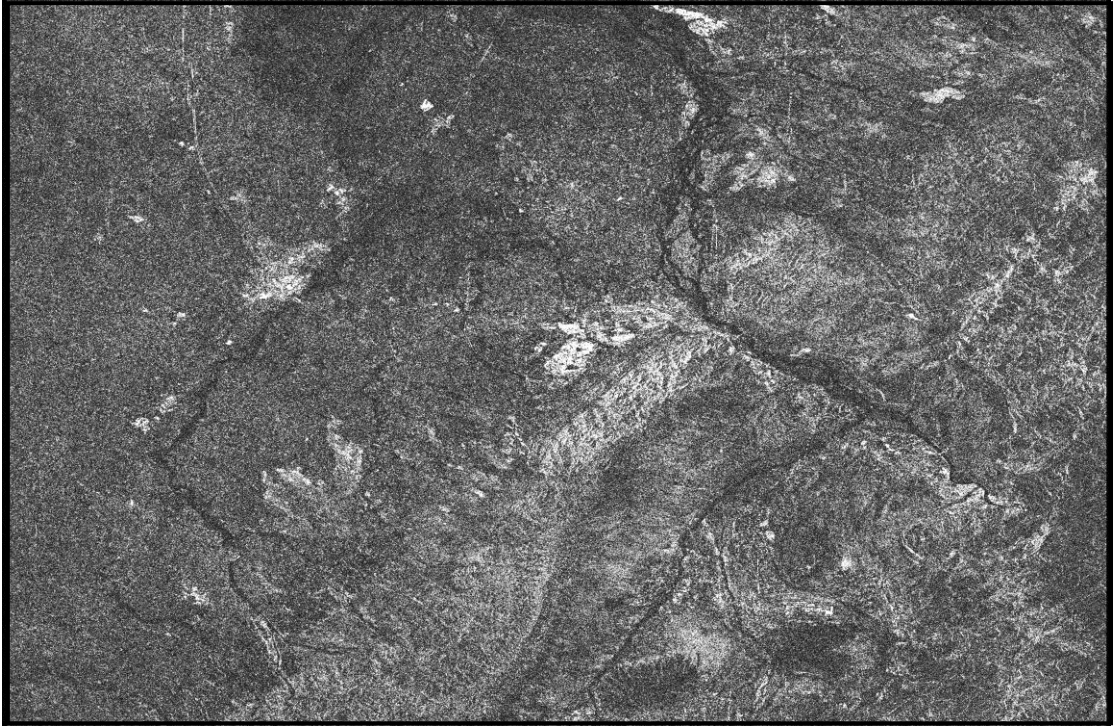


Figure 4.10: Coherence image obtained from the first pair (Master image and Slave image 1)

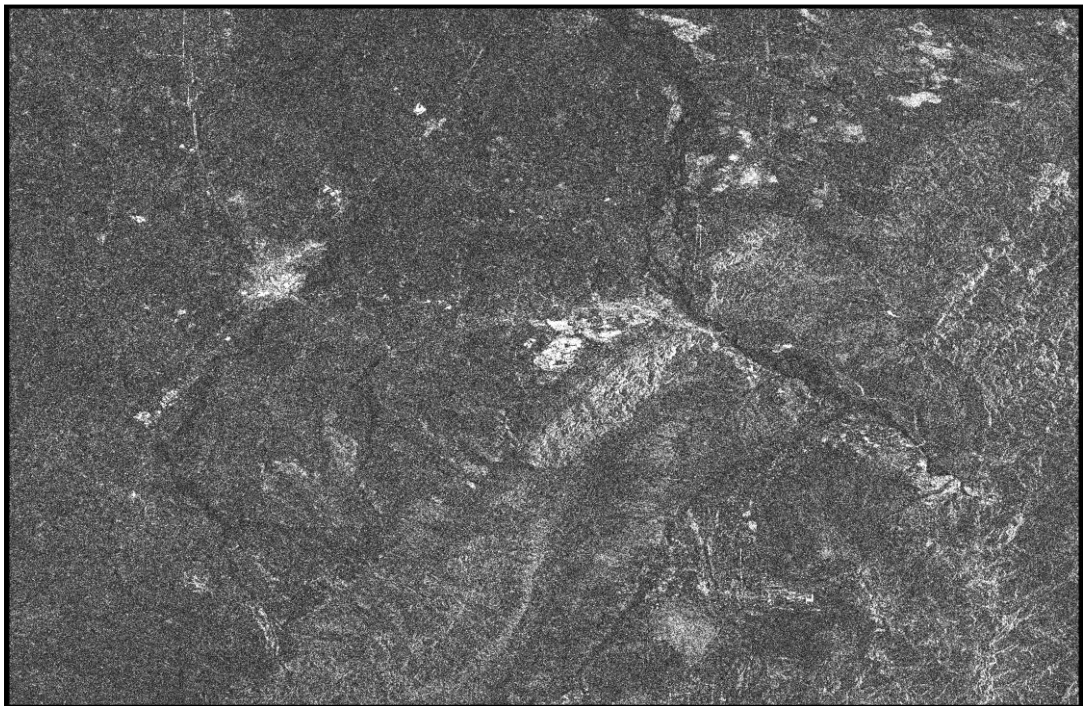


Figure 4.11: Coherence image obtained from the second pair (Master image and Slave image 2)

4.4.6. Phase Unwrapping

The two-dimensional phase signal in the interferogram is given as modulo 2π [43]. Phase unwrapping is the process in which the correct multiple of 2π is added to the interferometric phase for each pixel. The interferogram containing the wrapped phase values ($0 - 2\pi$ interval) which results in 2π ambiguity. The

unwrapping of the phase resolves the 2π ambiguity. This is the most crucial step in InSAR processing. The flattened interferograms are subjected to phase unwrapping process.

Figure [4.12] and Figure [4.13] show the unwrapped interferograms obtained from the two image pairs.



Figure 4.12: Phase unwrapped interferogram obtained from the first pair (Master image and Slave image 1)

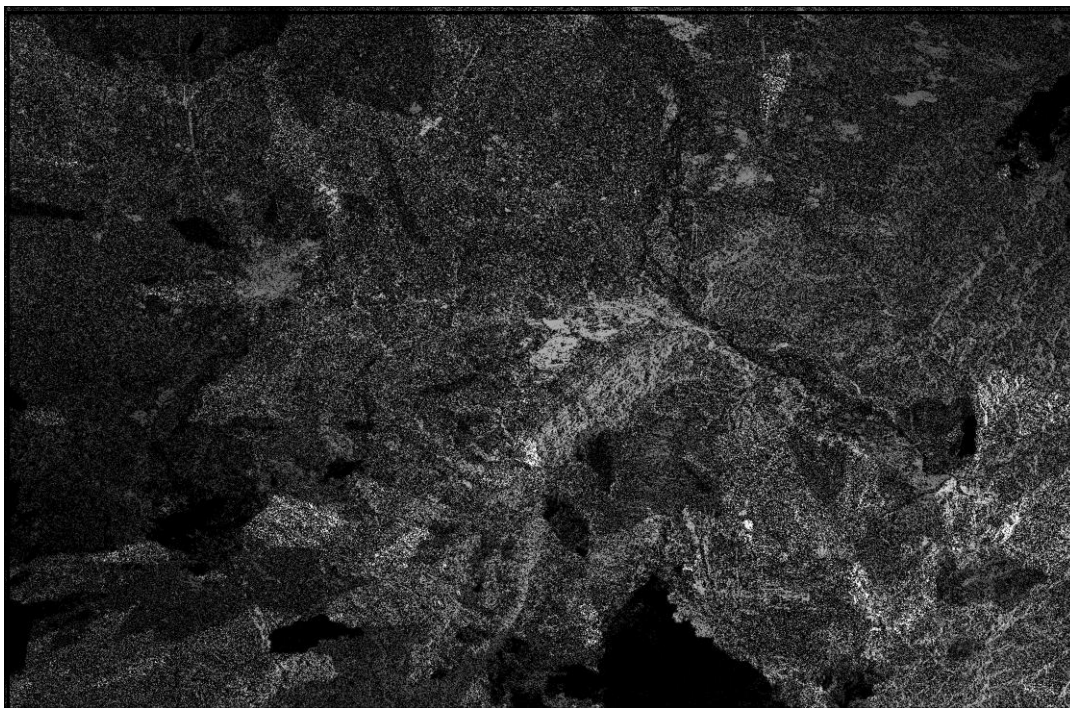


Figure 4.13: Phase unwrapped interferogram obtained from the second pair (Master image and Slave image 2)

4.4.7. DInSAR generation from the two interferograms

The final DInSAR generation step is implemented by using the flattened interferograms of the two pairs. The flattened interferogram Φ_{flat} is equal to the product of the perpendicular component of the baseline B_{\perp} and topographic angular distortion $\delta\theta$. From Figure [2.1] the ratio of the two phases according to [20] yield

$$\frac{\Phi_{flat}}{\Phi'_{flat}} = \frac{B_{\perp}}{B'_{\perp}} \quad (3.12)$$

In order to remove the topographic term and retain only the displacement term in the DInSAR, the data from the first interferogram are scaled to the perpendicular baseline conditions of the second interferogram and subtracted from it. This eliminates the confusion created between the topographic term and displacement term during the interpretation of results.

The differential phase equation is given by [20]

$$\Phi'_{flat} - \frac{B'_{\perp}}{B_{\perp}} \Phi_{flat} = \frac{4\pi}{\lambda} \Delta\rho \quad (3.13)$$

Where,

- $\Delta\rho$ = displacement term
- Φ'_{flat} = flattened interferogram generated from the second pair
- B'_{\perp} = perpendicular baseline component of the second pair

The DInSAR obtained from the above equation is shown in the Figure [4.14] below.

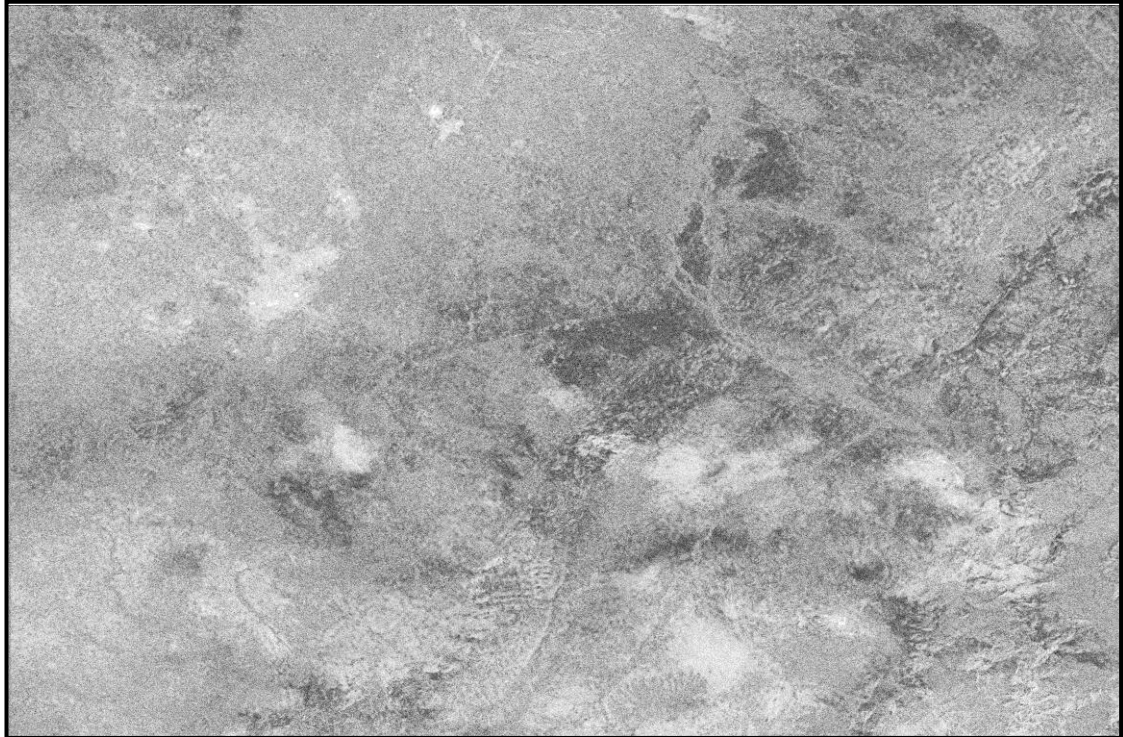


Figure 4.14: Differential Interferogram (DInSAR) obtained from the three SAR images (Master, Slave 1 and Slave2)

4.5. Phase Correction

The phase correction is done on the generated DInSAR using the range correction already calculated. The two interferograms which are a complex combination of module and phase are split into two components (phase and module). This is done in order to add the correction into the phase component of the DInSAR. Once the correction on phase is done, it is recombined with the module (intensity) component to get the corrected interferogram.

Due to the propagation delay of RADAR wave, the phase measurements corresponding to equations (2.1), (2.2) and (2.3) become

$$\Psi_1 = \frac{4\pi}{\lambda}(\rho + \Delta R_1) \quad (3.14)$$

$$\Psi_2 = \frac{4\pi}{\lambda}(\rho + \delta\rho + \Delta R_2) \quad (3.15)$$

$$\Psi_3 = \frac{4\pi}{\lambda}(\rho + \delta\rho' + \Delta R_3) \quad (3.16)$$

The interferometric phase of the two interferograms corresponding to equations (2.4) and (2.5) now become [5]

$$\Phi = \Psi_1 - \Psi_2 = \frac{4\pi}{\lambda}\delta\rho + \frac{4\pi}{\lambda}(\Delta R_1 - \Delta R_2) \quad (3.17)$$

$$\Phi' = \Psi_1 - \Psi_3 = \frac{4\pi}{\lambda}\delta\rho' + \frac{4\pi}{\lambda}(\Delta R_1 - \Delta R_3) \quad (3.18)$$

Where ΔR_1 , ΔR_2 , ΔR_3 are the atmospheric propagation delays obtained from the MODIS images corresponding to the master, slave 1 and slave 2 image acquisitions.

Let $\frac{4\pi}{\lambda}(\Delta R_1 - \Delta R_2) = \Psi_{correction1}$ and $\frac{4\pi}{\lambda}(\Delta R_1 - \Delta R_3) = \Psi_{correction2}$

Then,

$$\Phi - \Psi_{correction1} = \frac{4\pi}{\lambda}\delta\rho \quad (3.19)$$

$$\Phi' - \Psi_{correction2} = \frac{4\pi}{\lambda}\delta\rho' \quad (3.20)$$

Where, $\frac{4\pi}{\lambda}\delta\rho$ and $\frac{4\pi}{\lambda}\delta\rho'$ represent the corrected phase of the two interferograms.

The corrected phases are now combined with the respective module components previously extracted to produce the corrected interferograms. From the two corrected interferograms, the final DInSAR is generated using the equation [3.13]. This results in an atmospheric phase corrected differential interferogram. The corrected DInSAR along with validation is shown in the results and discussion section in the following chapter.

5. RESULTS AND DISCUSSIONS

This chapter presents the results obtained from the method discussed in chapter 4. It begins with the presentation of results obtained from section 4.2 followed by a discussion on the areas exhibiting high coherence. Finally the results obtained from phase correction of the interferograms are presented and discussed.

5.1. Path delay as an effect of atmospheric propagation

Understanding the effects of the two atmospheric layers on the interferograms requires the knowledge of the atmospheric properties on the day and at the time of acquisition of all the three SAR images forming the interferograms. This is supported by the histograms shown below obtained from the calculations (section 4.2).

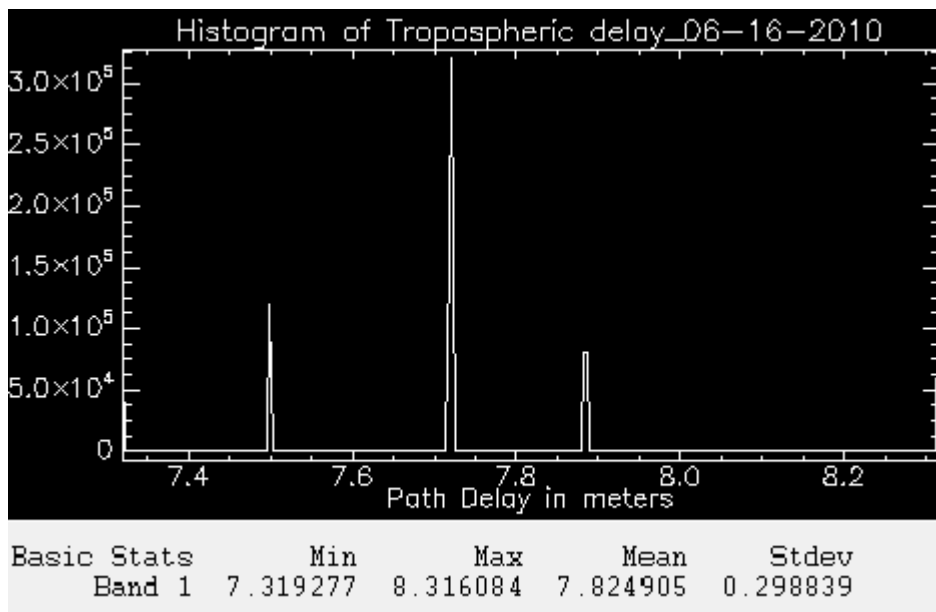


Figure 5.1: Histogram showing the tropospheric path delay caused on the day of acquisition of Master image

It is clear from Figure [5.1] that less tropospheric delay was experienced by the wave during the acquisition of the master image on June 6, 2010. This is mainly due to the presence of less water vapour and clouds. Considerably less water vapour forming clouds are encountered in this region on this date as this month is apparently dry albeit a delay of 7.6 m to 7.8 m is noticed at some points in the region. The histograms of path delay occurred on the same region on August 8, 2010 and September 16, 2010 shown in Figure [5.2] and Figure [5.3] below give an idea of the atmospheric characteristics on that particular day.

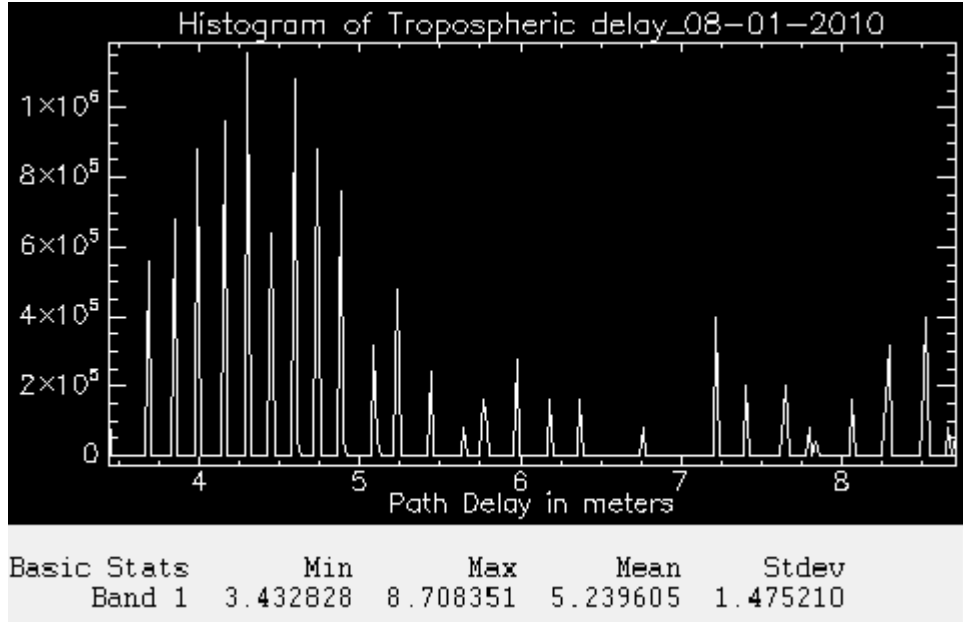


Figure 5.2: Histogram showing the tropospheric path delay caused on the day of acquisition of Slave image 1

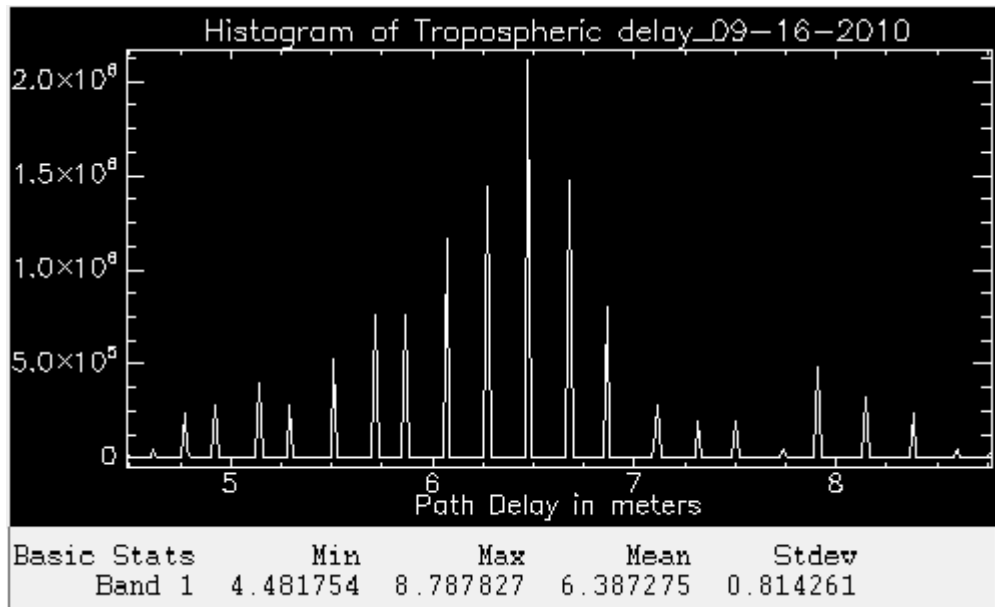


Figure 5.3: Histogram showing the tropospheric path delay caused on the day of acquisition of Slave image 2

The above two figures clearly show that the tropospheric path delay varies between 2 m and 10 m. The two way tropospheric delay can add up to 16 m [29]. This indicates the presence of considerably high amount of water vapour and clouds causing elongation of the wave passing through them.

The TEC present in the ionosphere majorly affects longer RADAR wavelengths (L-band). This dispersive medium affects the signal delay proportionately to λ^2 [35] according to equation (3.4). The map in Figure [4.2] above shows that the TEC varies monthly. Daily TEC maps are also available which show the TEC variations on a daily basis. According to the availability of the map, global yearly-monthly TEC map has been used in the present work. Variations in TEC depend on the degree of ionization i.e. the number of free electrons. The traversing signal interacts with the free electrons causing a path delay that depends on

the frequency of the traversing signal. Using the equation (3.4), the ionospheric path delay was calculated using the monthly ionospheric TEC map. The TEC found in all the three months and the amount of delay occurred is given below.

Table 5.1: Path delay calculated from TEC

	TEC (TECU)	Path delay (m)
June	9×10^{16}	- 5.39
August	11×10^{16}	- 6.59
September	12×10^{16}	-7.19

The total delay caused due to troposphere and ionosphere is shown in the form of histograms below.

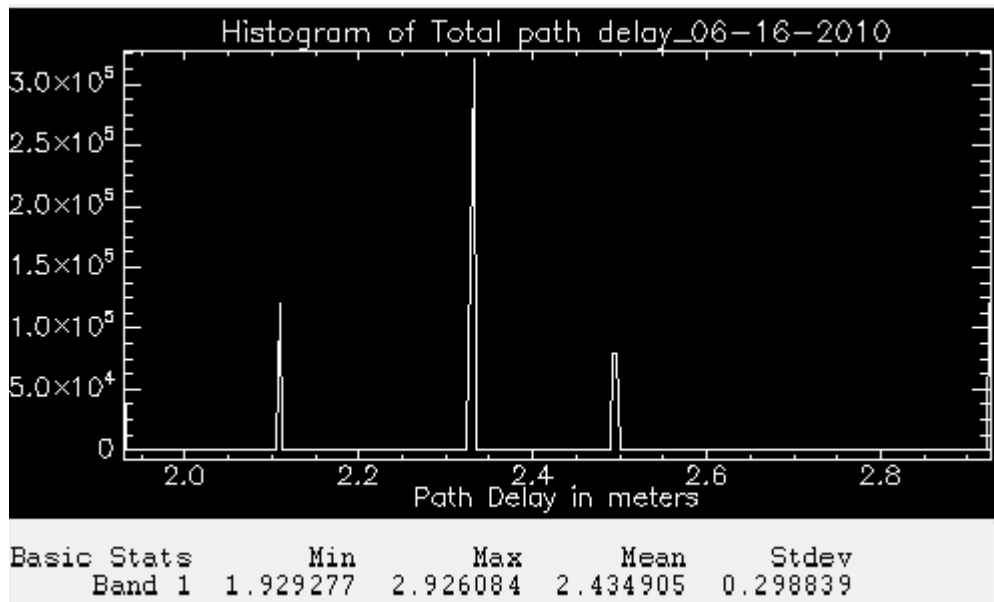


Figure 5.4: Troposphere Ionosphere delay (total path delay) occurred on June 16, 2010

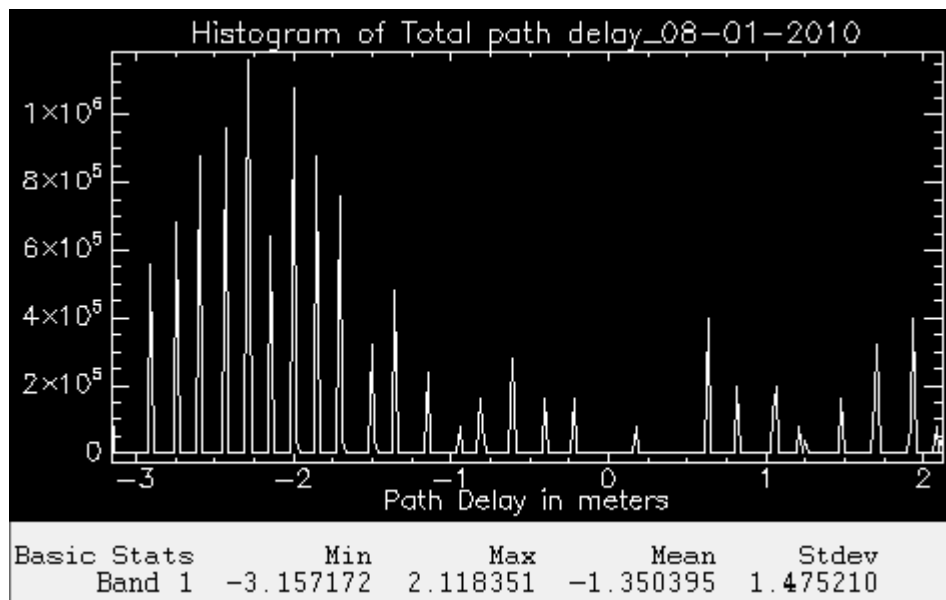


Figure 5.5: Troposphere Ionosphere delay (total path delay) occurred on August 01, 2010

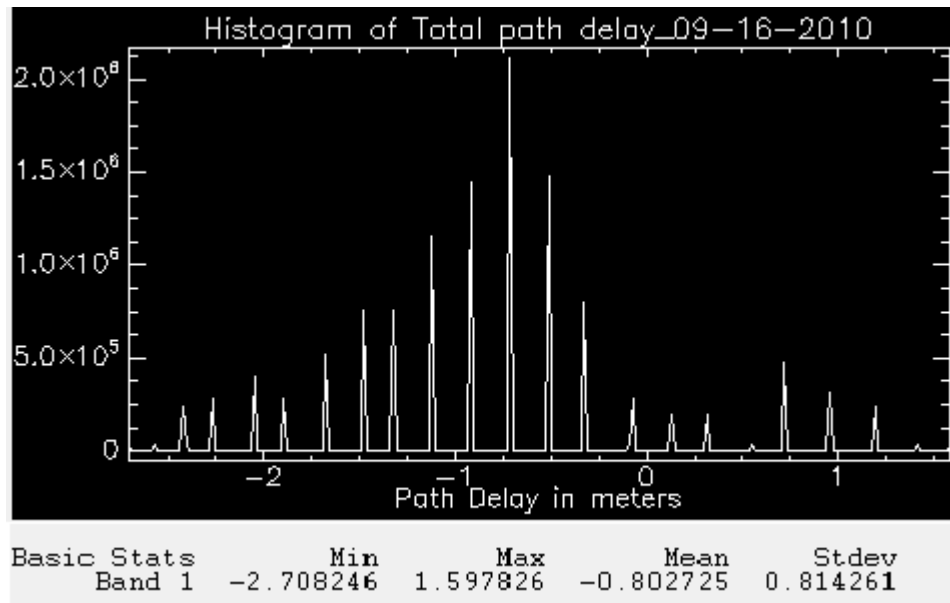


Figure 5.6: Troposphere Ionosphere delay (total path delay) occurred on September 16, 2010

Figure [5.4], Figure [5.5] and Figure [5.6] show the total path delay occurred on 16 June 2010, 01 August 2010 and 16 September 2010 respectively. The negative sign of the delay indicates phase advance.

The difference between the ionospheric and tropospheric effects is based on sign of delay. The electron density in the ionosphere creates propagation path shortenings or phase advance and the partial pressure of water vapour in troposphere causes an increase in the observed range or phase delay. Also, areas with reduced water vapour (hole in the cloud layer) results in a phase advance [6].

5.2. A discussion on the degree of similarity (coherence) between the three images

The quality of the interferometric phase is determined by its coherence product. InSAR pairs with low coherence are not suitable to derive reliable phase related measurements. A strong coherence indicates that two images are identical. Thus, a measurement of phase stability between two RADAR images is termed as coherence. The study area chosen for this study, as mentioned in section 3.2, consists of different types of land cover and land use. Urban areas and areas covered with rocks maintain a high coherence. Agricultural fields captured at the same period of the year also exhibit high coherence. A weak coherence between acquisitions may originate due to many reasons like geometric deformations introduced by SAR, water surfaces, changes on land, forests etc. The coherence images show bright patches at some places with pixel values close to one indicating high coherence. For the study, two areas showing high coherence have been considered and the degree of similarity between the three images has been studied.

One of the areas within the study site having high coherence is shown in Figure [5.7] below.



Figure 5.7: Google image of Region 1 showing settlement areas

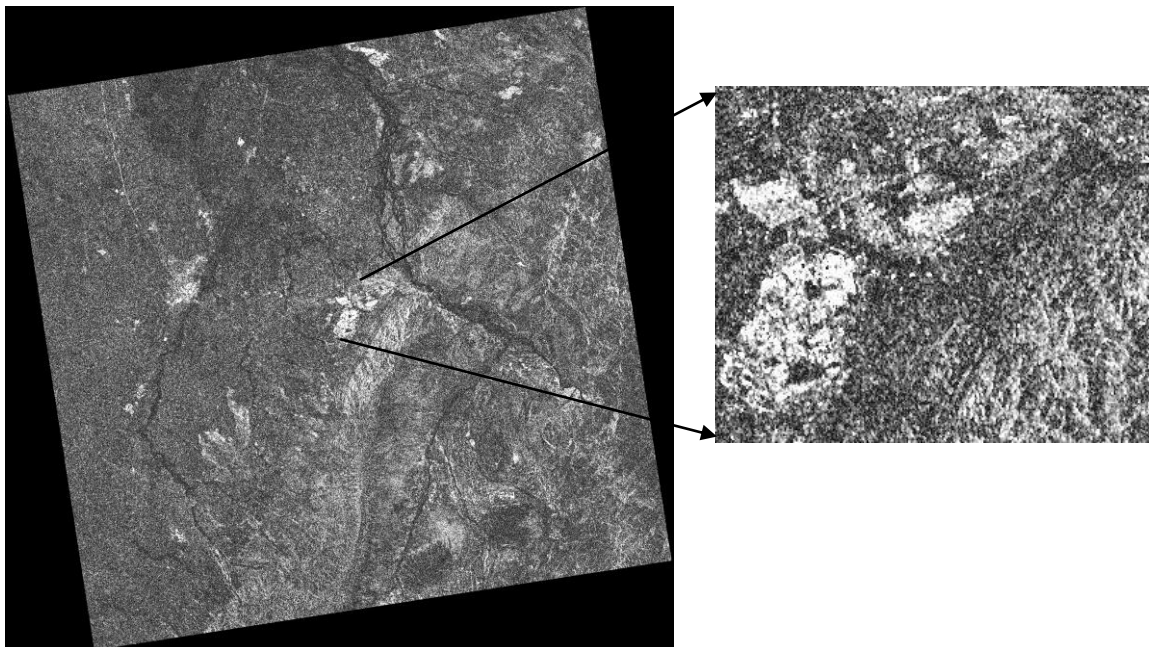


Figure 5.8: Region 1 showing high coherence between Master image and Slave image 1

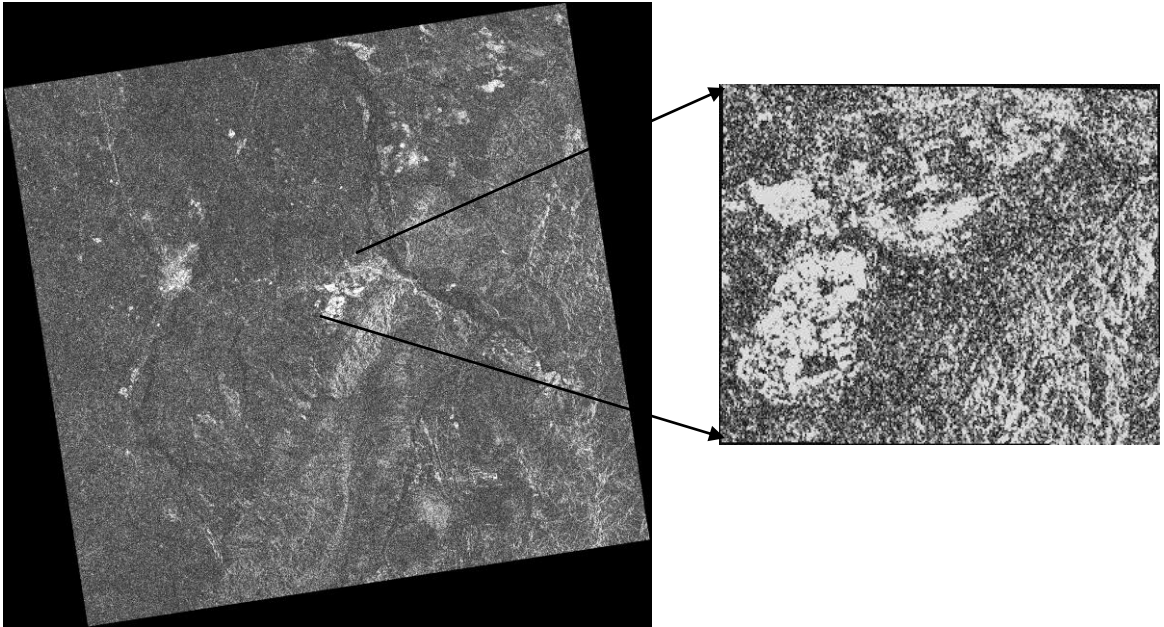


Figure 5.9: Region 1 showing high coherence between Master image and Slave image 2

The above Figure [5.8] and Figure [5.9] clearly show one of the regions within the study site indicating high coherence. This Region 1 which covers the areas Hetampur, Jwalapur, Meerpur etc consists of settlement areas.

Many other regions within the study site exhibit high coherence. To illustrate this, one more region is considered and its coherence between the two image pairs (Master and Slave image 1, Master and Slave image 2) is studied. This region (Region 2) comes under the city Roorkee which is one of the majorly established urban areas of Uttarakhand. The Google image shown in Figure [5.10] and the coherence images in Figure [5.11] and Figure [5.12] indicate the presence of urban settlement area exhibiting high coherence.



Figure 5.10: Google image of Region 2 showing settlement areas

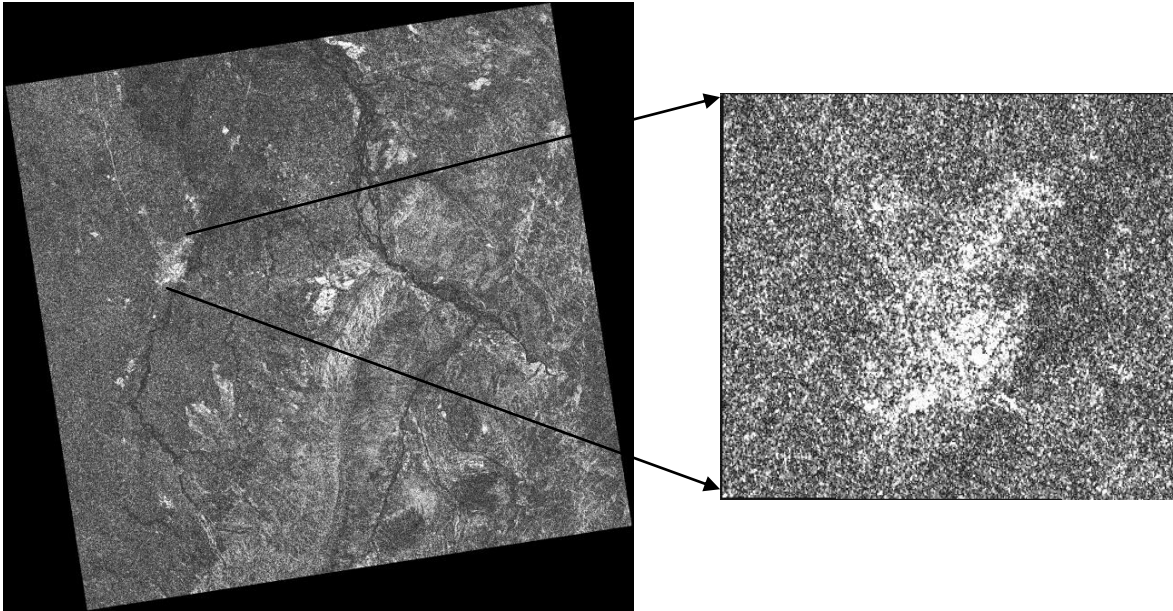


Figure 5.11: Region 2 showing high coherence between Master image and Slave image 1

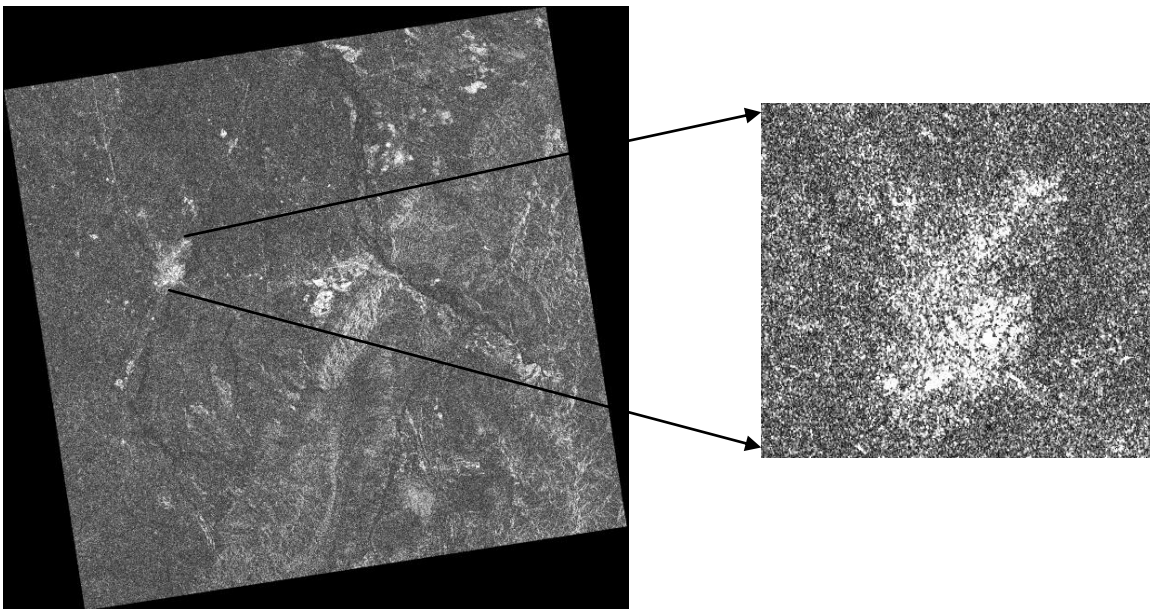


Figure 5.12: Region 2 showing high coherence between Master image and Slave image 2

The coherence values between the two image pairs for the two regions as shown in graphical form in Figure [5.13] and Figure [5.14] below vary very closely. The coherence values as inferred from the below graphs vary between 0.6 and 0.9 indicating that the scattering mechanisms in these areas have not faced any changes between the times of acquisition of the images. During the 46 days revisit interval of the satellite, these areas have maintained their stability without undergoing any kind of changes. These areas as seen from the Google images in Figure [5.7] and Figure [5.10] mark the settlement areas which are regarded as scatterers not changing frequently unless there is some human intervention (construction work), some form of land movement disturbing the structures etc. The plain lands present within the study area also show high degree of similarity between the images taken.

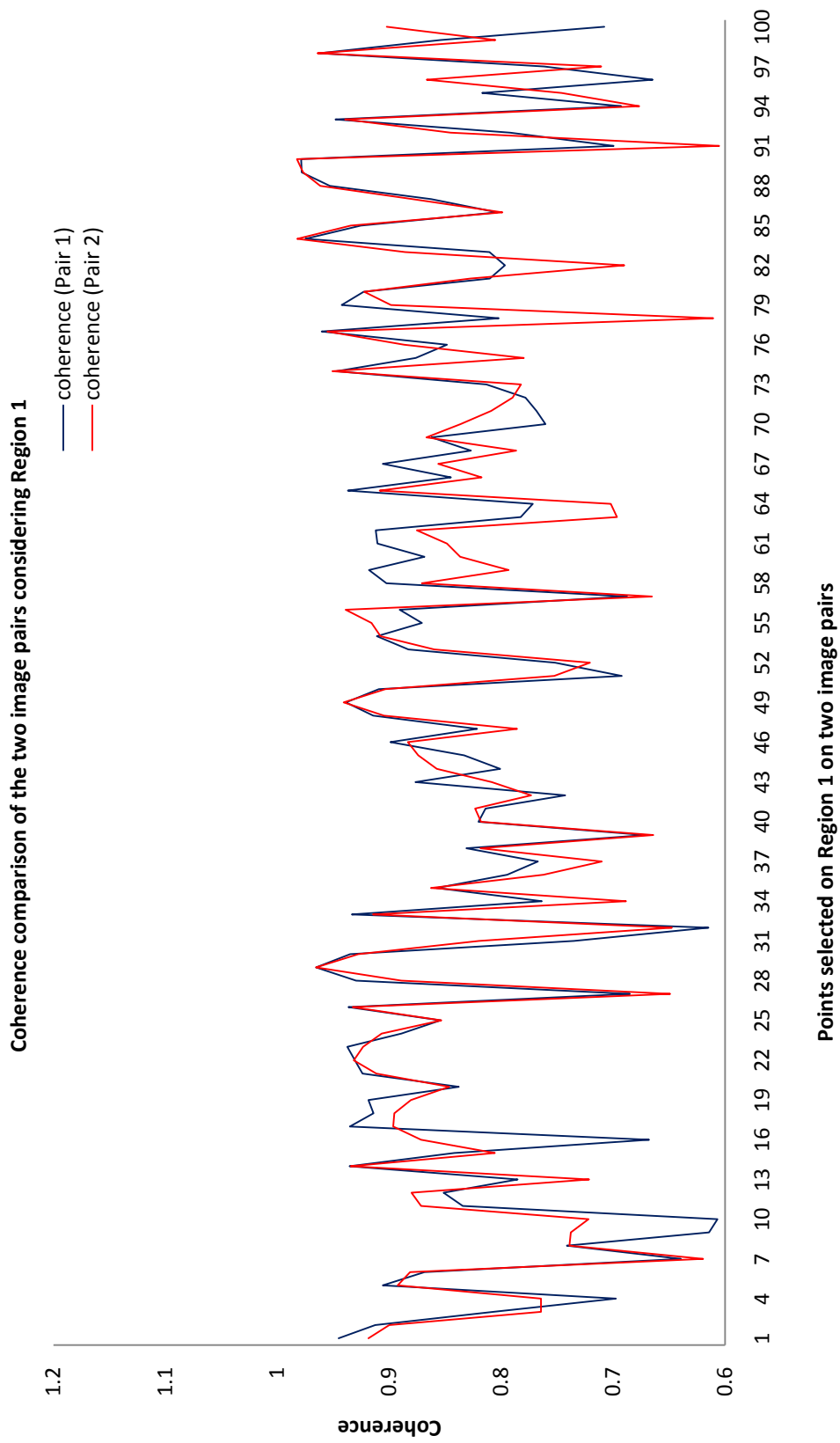


Figure 5.13: Variation of coherence between the two image pairs (Region 1)

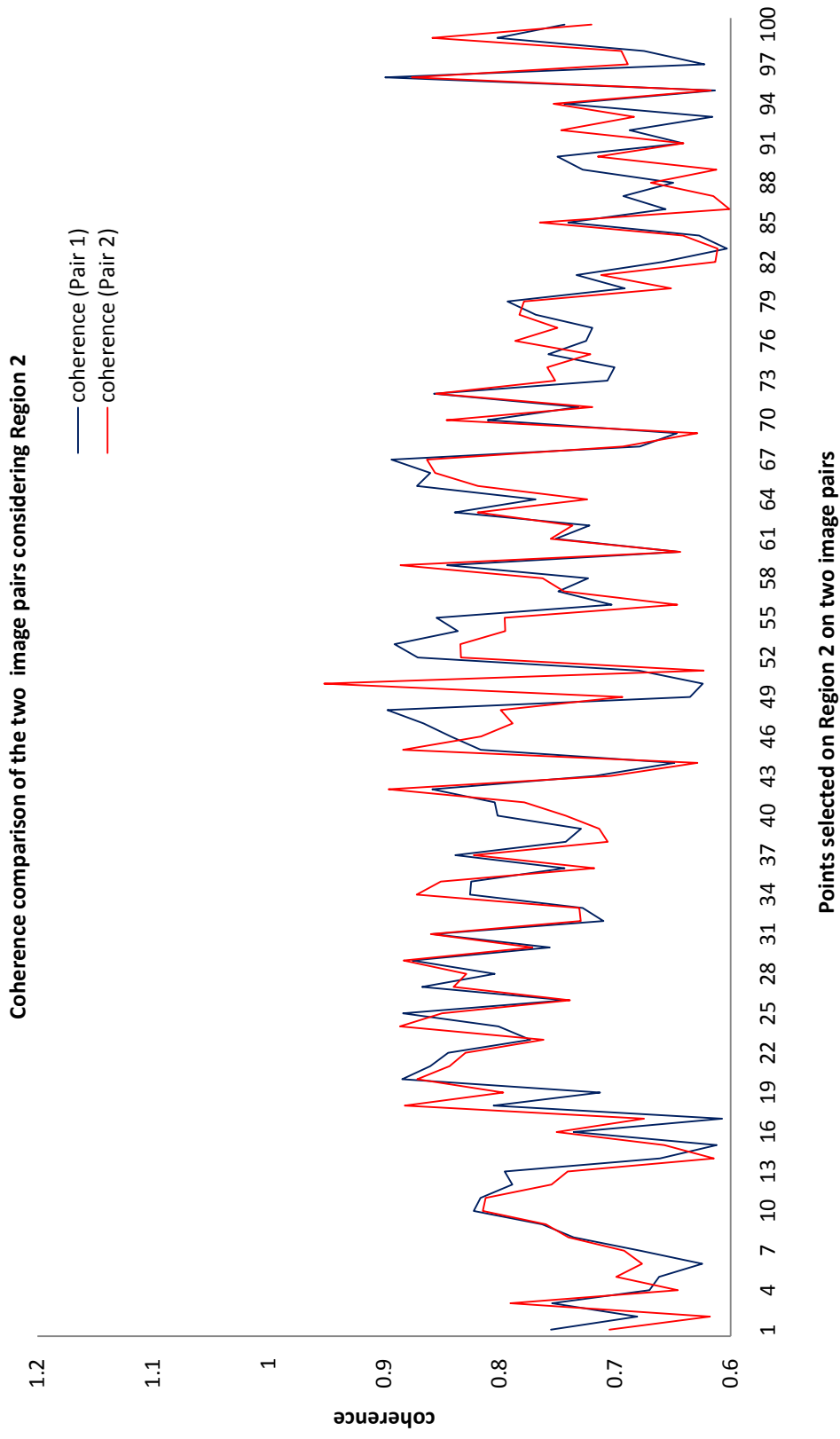


Figure 5.14: Variation of coherence between the two image pairs (Region 2)

From the two coherence images, 100 points have been taken on Region 1 and Region 2 to show the variation in coherence values between the two image pairs. This variation on both the regions is clearly indicated in the above two graphs. It is clear from the above graphs that the regions 1 and 2 which have not changed between the image acquisitions show high coherence which is the main requirement for repeat-pass interferometry. Other areas in the study area have undergone changes between the image acquisitions and act as a source of error in repeat-pass interferometry. Hence, the regions with low coherence indicate phase instability and therefore are not suitable for repeat-pass interferometric studies.

5.3. Effects of phase correction on interferogram

The path elongation caused due to the refractive index of atmosphere introduces errors in the phase of an interferogram. For a differential interferogram, these variations in phase have a large impact on the measurements obtained. Once the amount of path delay occurred is estimated, the correction is applied to the phase of the DInSAR generated as described in section 4.4.7. Phase of the interferogram formed from Master image and Slave image 1 (Pair 1) is given below.

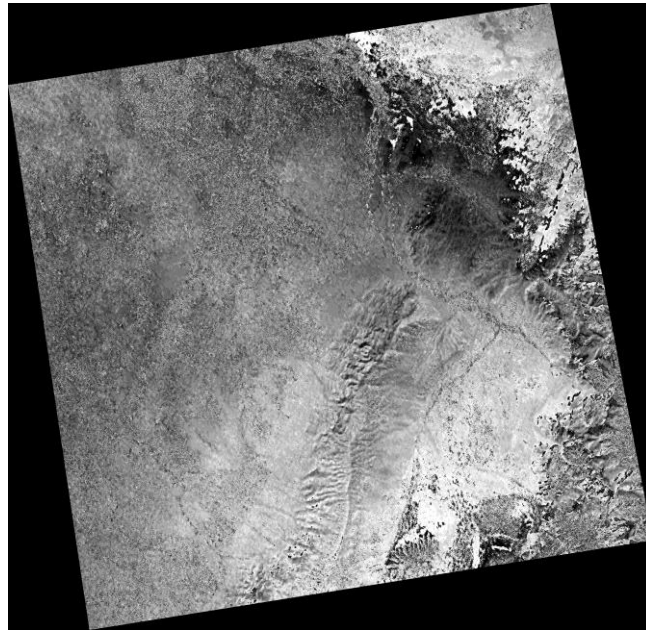


Figure 5.15: Phase image (Pair 1) before correction

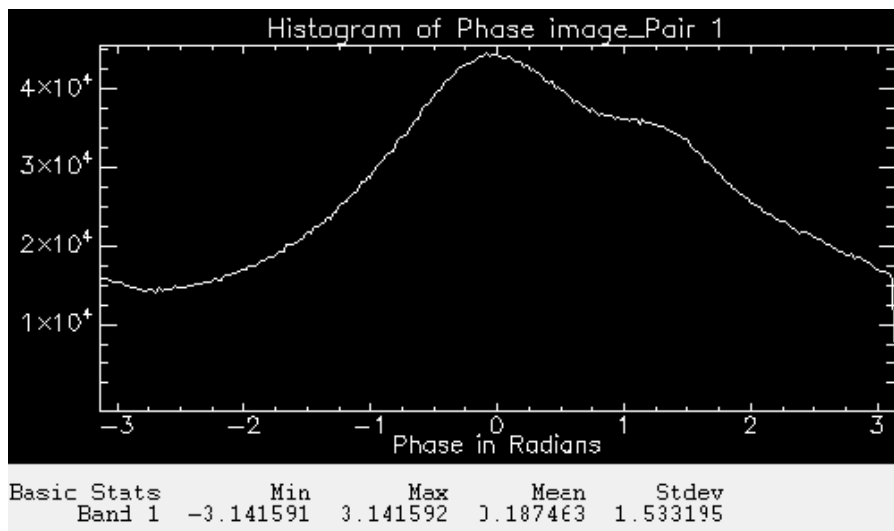


Figure 5.16: Phase variation of Pair 1 before correction

Figure [5.15] shows the phase of the interferogram (Pair 1) before correction. The phase as seen in Figure [5.16] varies from -3 to +3 radians. The phase thus obtained is a result of the contribution of phase from topography, atmosphere, noise and baseline decorrelation. The objective of this study i.e. the removal of atmospheric phase is achieved by applying the method explained in section 4.5 and the phase of the interferogram after applying the correction is shown in Figure [5.17] and Figure [5.18] below.

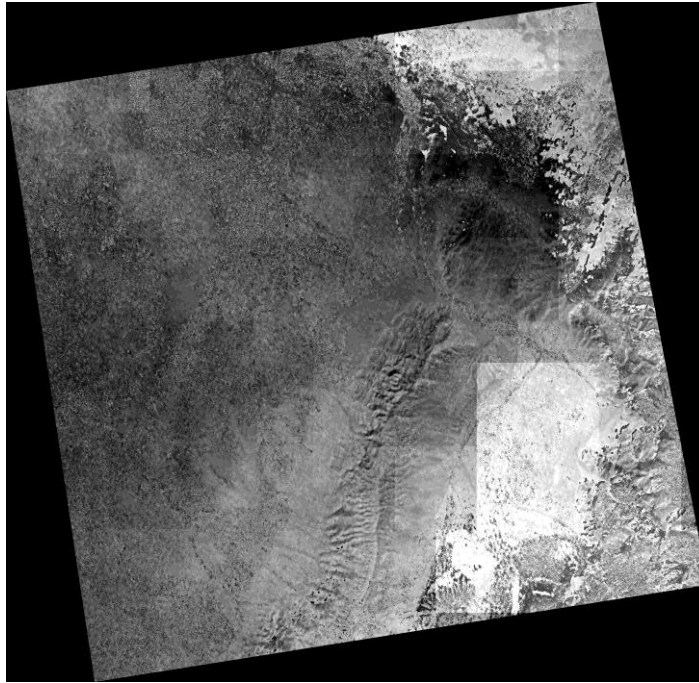


Figure 5.17: Phase image (Pair 1) after correction

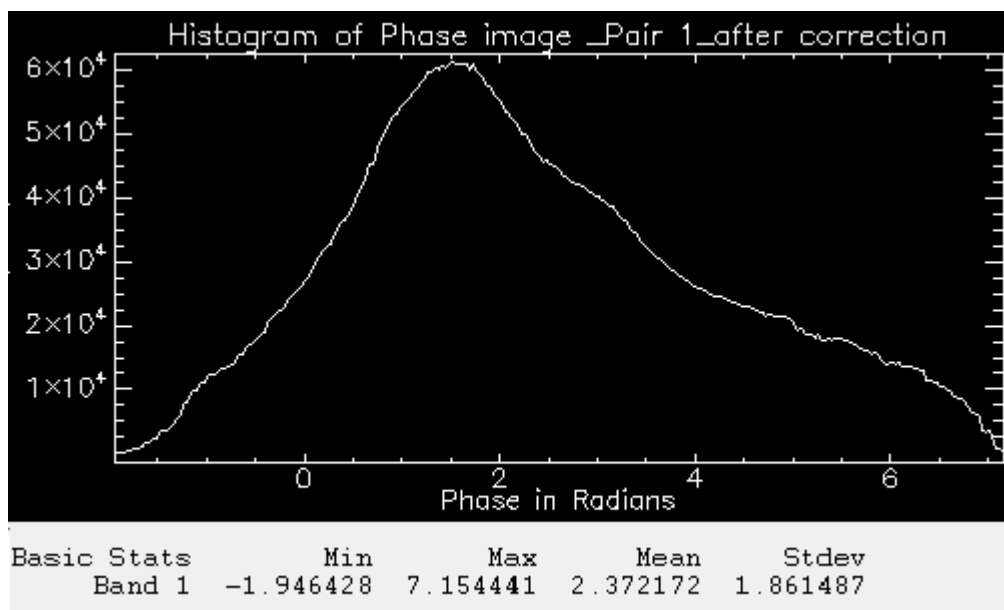


Figure 5.18: Phase variation of Pair 1 after correction

Practical application of error correction on the phase of an interferogram with zero baseline should result in a phase close to zero. But when the baseline is kept zero, there will not be any phase difference information obtained. Hence, there must be a shift in the location of the instrument. This interferogram (topo-pair) consists of topographic phase, phase due to atmospheric delay and phase due to non-zero baseline. Since the topographic phase is removed from this pair in the interferogram flattening process (section 4.4.4), this phase is left with phase due to baseline decorrelation, phase noise and atmospheric induced phase. When the atmospheric correction is applied, the resultant phase should have been zero. But due to the baseline phase component, the phase is not showing values close to zero. As seen in above figure, even after applying the correction, there is a large variation in phase. As mentioned in section 4.4.2, the normal baseline value obtained for Pair 1 is 254.41 m. As the separation between the measurements increases, the scattered field pattern will become less similar and hence the signals will decorrelate [1]. The degree of decorrelation depends upon the baseline (the separation distance). When compared to Pair 2 (having a shorter baseline), this large baseline of Pair 1 has an effect on the phase and thus has resulted in such a variation even after atmospheric error is removed. Other source of error is the phase noise occurred due to temporal changes of the scatterers and volume scattering.

Considering the second interferogram (Pair 2), the phase variation before correction can be seen in Figure [5.19] and Figure [5.20] below. It shows a variation of -3 to +3 radians.

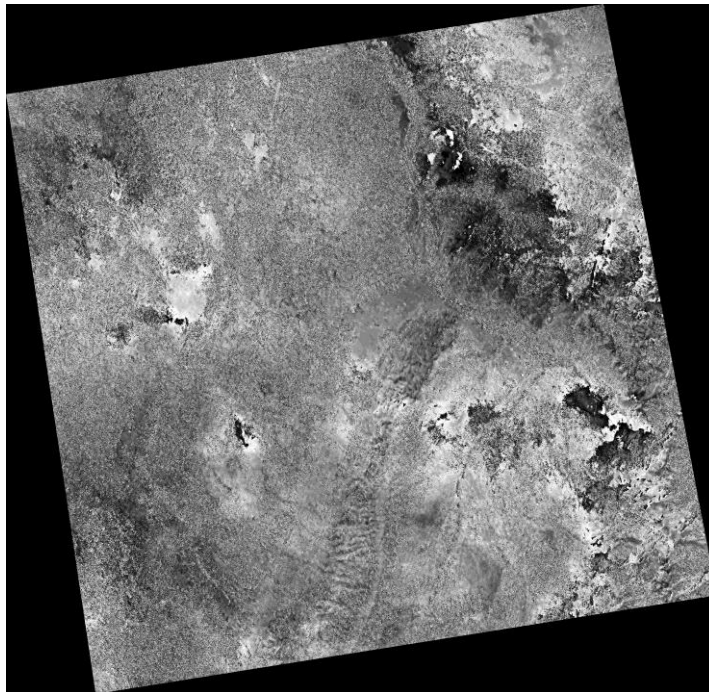


Figure 5.19: Phase image (Pair 2) before correction

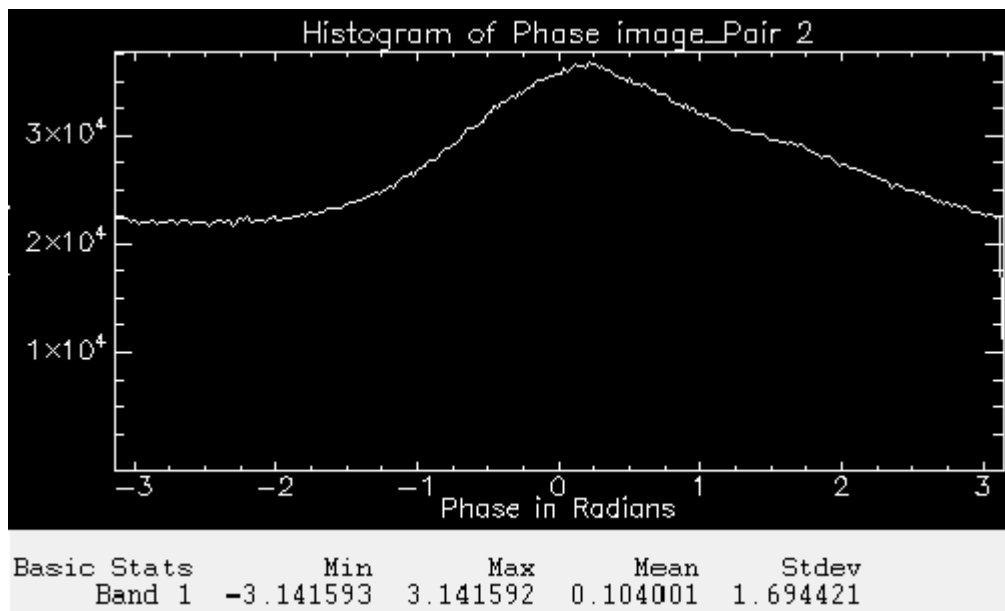


Figure 5.20: Phase variation of Pair 2 before correction

The changes in phases after applying atmospheric correction can be seen in Figure [5.21] and Figure [5.22] showing phase and phase variation of Pair 2 after correction.

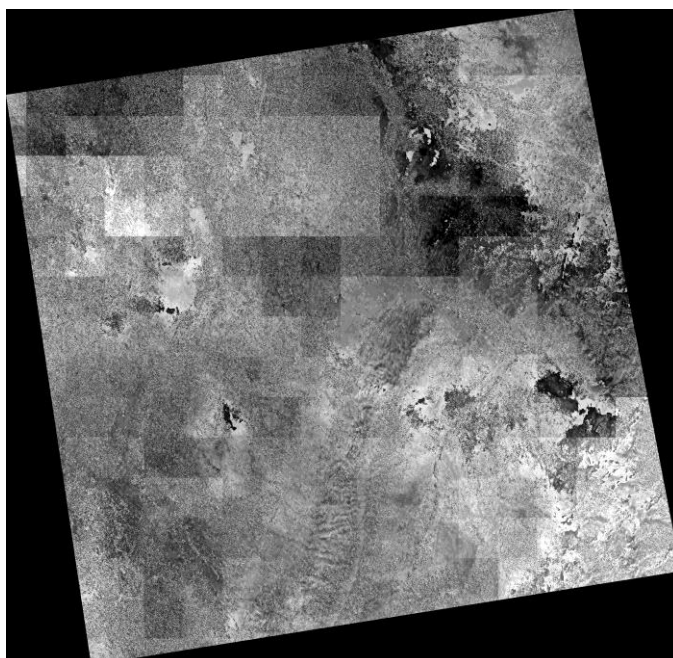


Figure 5.21: Phase image (Pair 2) after correction

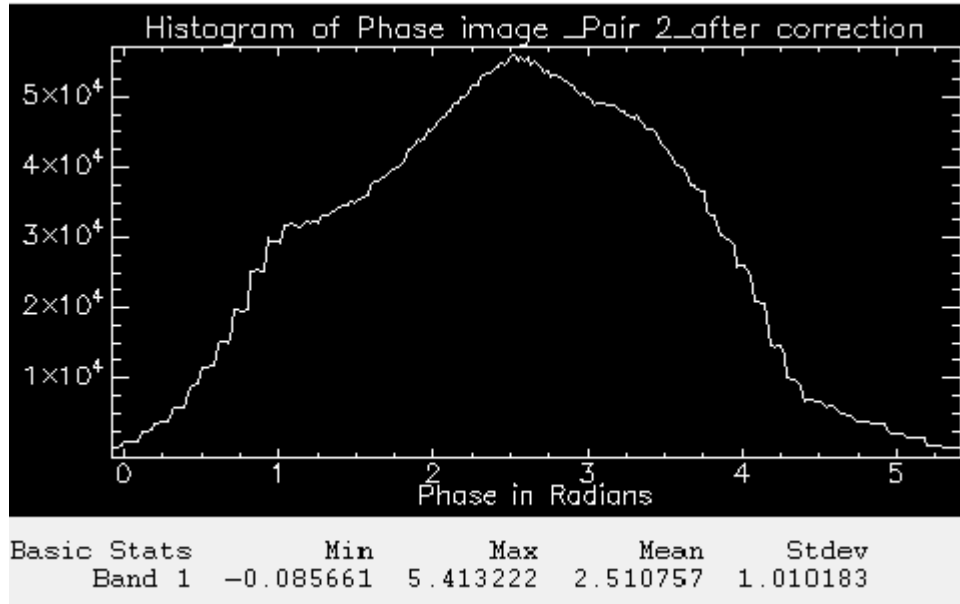


Figure 5.22: Phase variation of Pair 2 after correction

The Pair 2 (defo-pair) consists of phases due to surface displacements, atmosphere and phase noise. This pair is acquired with a smaller baseline and therefore no significant contribution of phase due to baseline decorrelation exists. According to a minor survey made on the study site, no changes in the land (ground displacements) have been recorded. Hence, phase due to surface displacement does not appear. Now, this phase is left with atmospheric phase and phase noise. Generally after applying the correction to the phase of the second pair (defo-pair), the phase values must have appeared approximately close to zero. But in this case, the result as seen in Figure [5.22] above, does not give values close to zero. When atmospheric correction is applied, the residual atmospheric phase is cancelled out leaving only phase due to noise. As mentioned in section 3.2, the chosen study area consists of highly vegetated areas and water bodies which lead to coherence loss. Along with the presence of urban settlement areas and plain lands, areas exhibiting temporal decorrelation also exist. These regions form a source of phase noise which includes error due to temporal decorrelation and volume scattering.

Within the target area, when there is a large spread of scatterers, a problem in estimating coherence occurs due to the range of heights of the scatterers (for example, forests). This volume decorrelation is treated to be important as it creates a problem in interferometry. Also, the time delay between the acquisitions causes temporal decorrelation. Very few targets remain unchanged over time. The changes in water, sand, vegetation, agricultural surfaces have a significant impact on the measured coherence. Hence, the above Figure [5.21] shows atmospheric corrected phase consisting of phase values due to phase noise.

When the permanent scatterers such as buildings, plain areas exhibiting high coherence are considered, after atmospheric error removal, they should indicate phase values close to zero. These areas do not include errors due to volume decorrelation (as there is no vegetation) and temporal decorrelation (as they show high coherence). But they include phase due to the different baseline factor required for height extraction.

The difference can be noticed between the phase considering the whole study site which includes areas of both low and high coherence and the phase considering only the areas of high coherence after applying atmospheric correction. As mentioned in chapter 3, the study area consists of all kinds of scatterers. Water bodies, agricultural patches, and vegetation have a tendency to change and permanent structures such as buildings do not change frequently. Due to the changing features, coherence loss is introduced between

the image acquisitions which even after atmospheric correction have an impact on the measurements made. Hence, the phase variations obtained in both the interferograms, before and after applying the correction on the whole area and on the area exhibiting high coherence are studied. It can be noticed in the graphs given below that the correction has not yielded good results when the whole area is considered leaving the region 1 (high coherence). Correction when applied only on the area of high coherence within the study area (region 1) yields better results. From the whole image (leaving the regions of high coherence) 100 points have been taken to study the phase variation and 100 points have been taken on the area of high coherence (Region 1) and the results are compared. Figure [5.23] and Figure [5.24] below show the phase comparison for Pair 1 and Figure [5.25] and Figure [5.26] show the phase comparison for Pair 2. These Figures indicate the influence of atmospheric correction on the phase of the interferograms considered on both areas of low and high coherence.

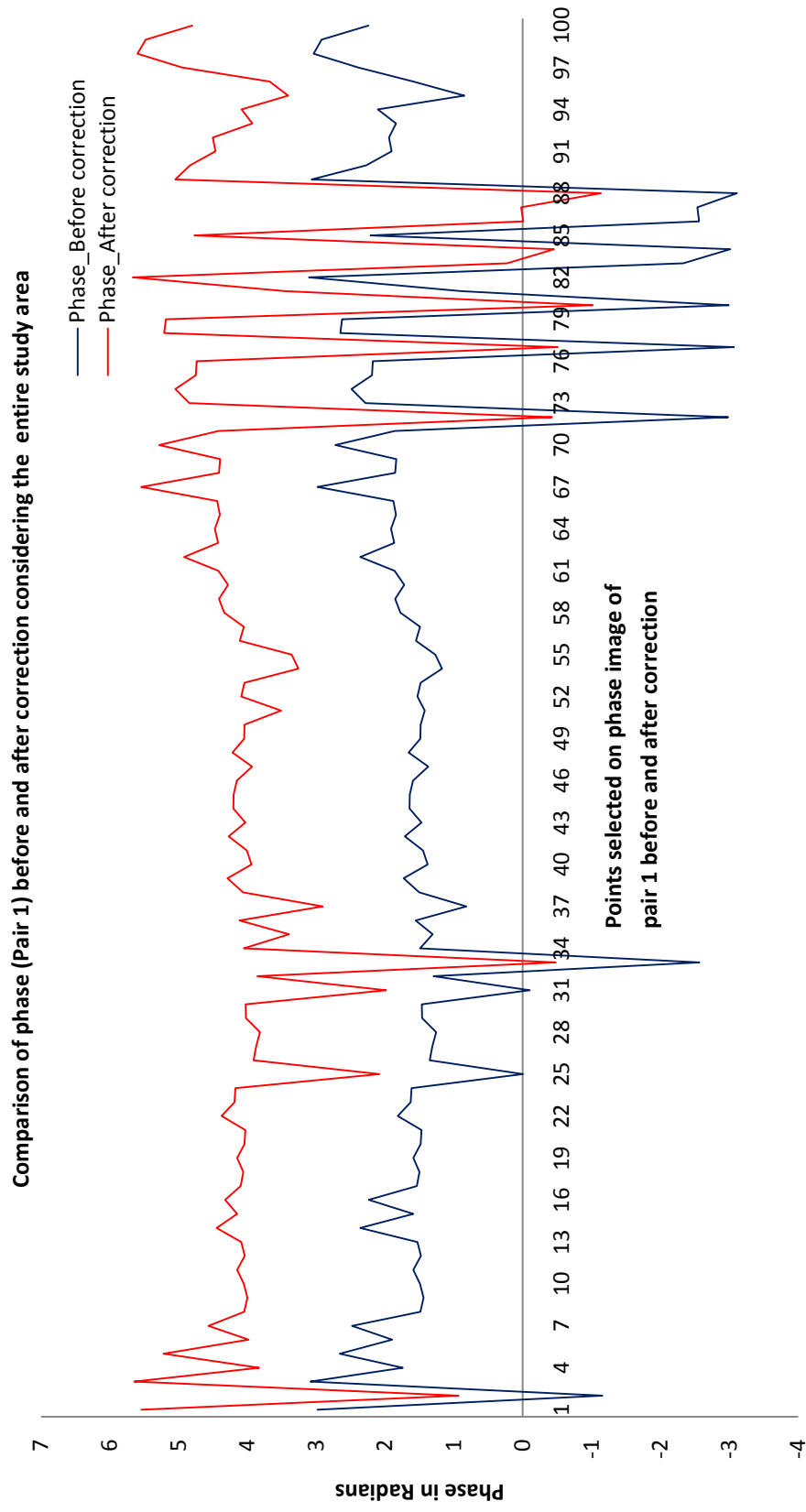


Figure 5.23: Pair 1 (100 points chosen on entire study area)

Due to the presence of changing scatterers within the study area, the phase even after applying error correction does not show good results.

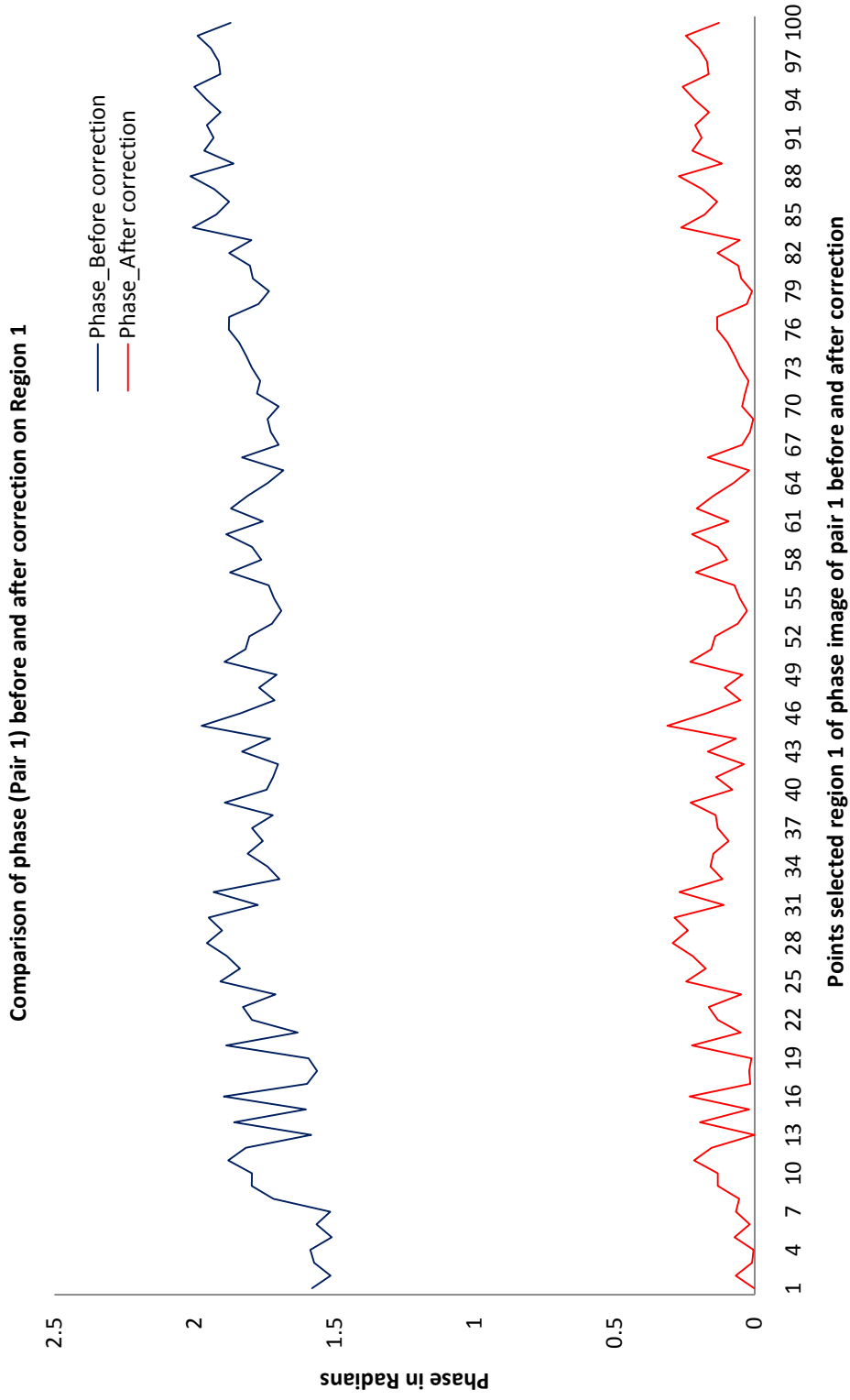


Figure 5.24: Pair 1 (100 points chosen on region 1 of study area)

Before applying the correction, the phase in Region 1 showed a high variation from 1.5 to 2 radians. After correction, the phase varies between 0 and 0.5 radians clearly indicating the impact of applying error correction. This is due to the presence of permanent scatterers which have not faced any changes.

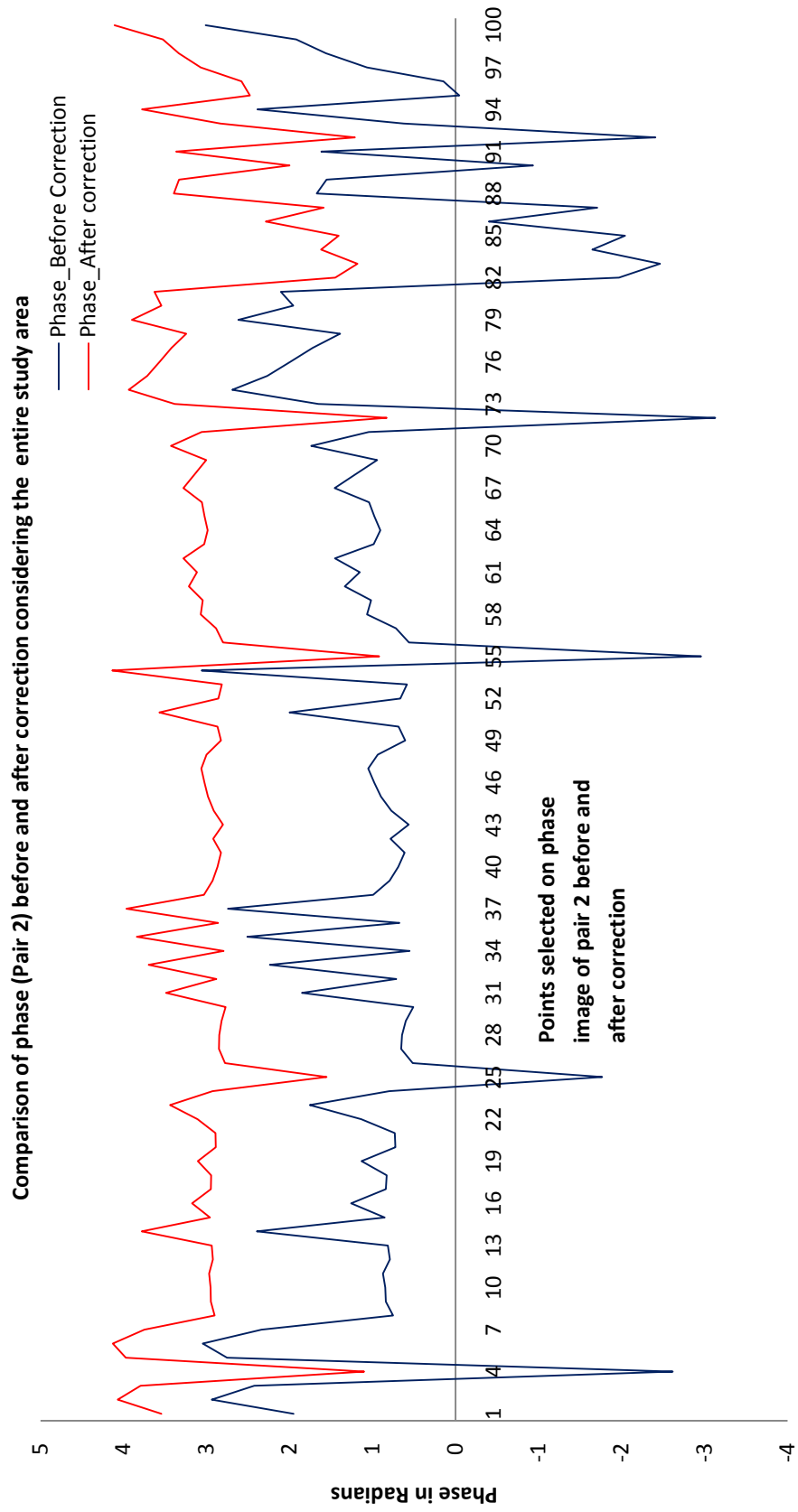


Figure 5.25: Pair 2 (100 points chosen on entire study area)

Similar to the results obtained for pair 1, the correction applied for the whole area for pair 2 does not yield good results.

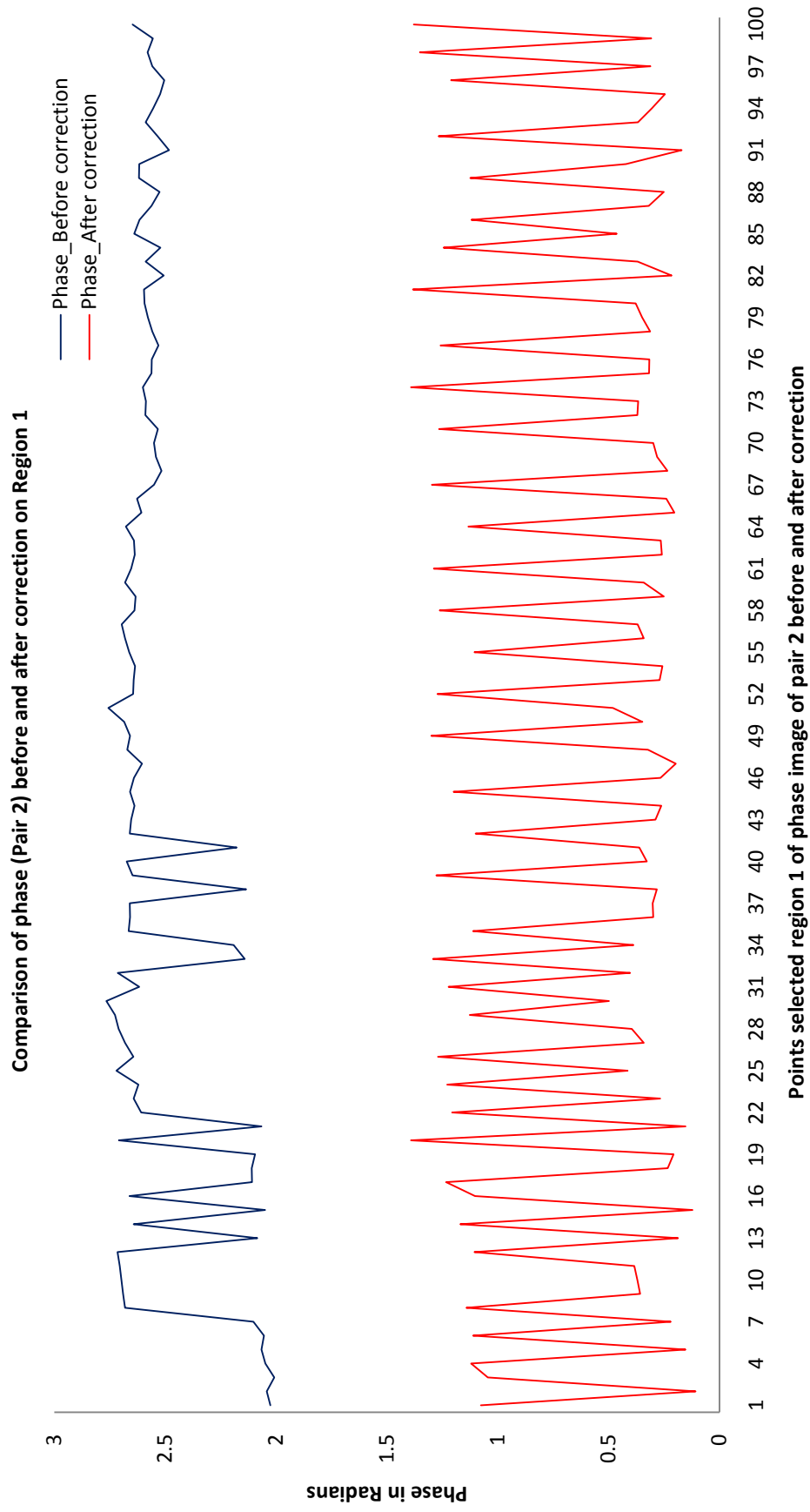


Figure 5.26: Pair 2 (100 points chosen on region 1 of study area)

Similar to the results obtained for pair 1, better results are obtained for regions of high coherence due to their non changing nature.

In Figure [5.23] above, 100 points have been taken randomly on the entire phase image of pair 1 before and after correction and the phase variation is mapped. Because of the change in scatterers, coherence loss is induced and thus the correction has not shown effective results. But when the correction applied on one of the regions within the study area showing no changes is analysed, the phase values appear close to zero as shown in Figure [5.24]. When the same 100 points are taken on phase image of pair 2, the correction gives similar results. The same procedure is applied for pair 2 and results are shown in Figure [5.25] and Figure [5.26] above. This gives a comparative study of the application of repeat-pass interferometry on regions of low coherence and on regions of high coherence. This graphical analysis also signifies the importance of coherence between images and applying atmospheric correction on interferograms.

5.3.1. Correction on phase of DInSAR

Using the two corrected interferograms, the DInSAR is generated. A comparison of the generated three-pass DInSAR before and after correction is shown in Figure [5.27] and Figure [5.28] below.

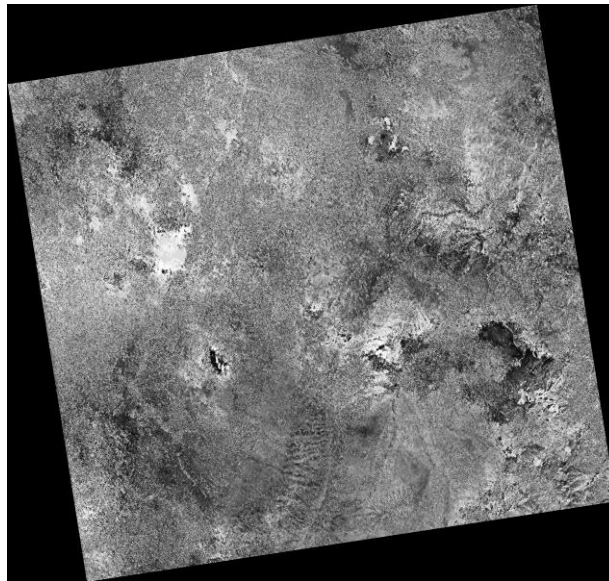


Figure 5.27: Phase image of DInSAR before correction

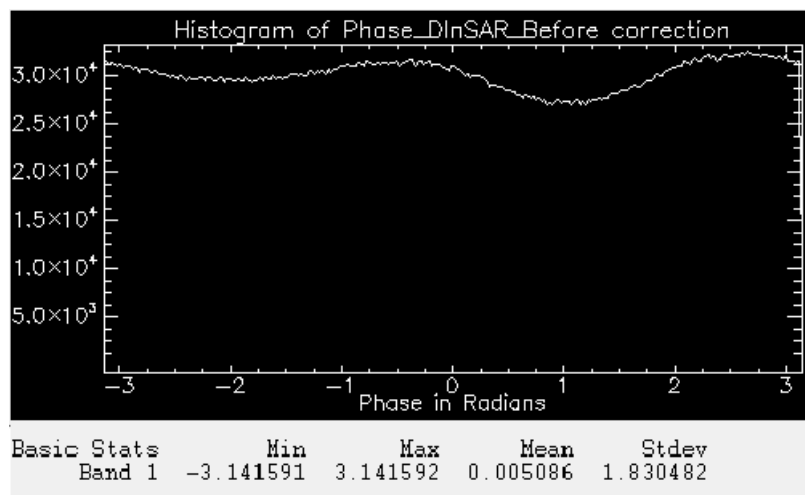


Figure 5.28: Phase variation of DInSAR before correction

5.3.1.1. DInSAR Error Map

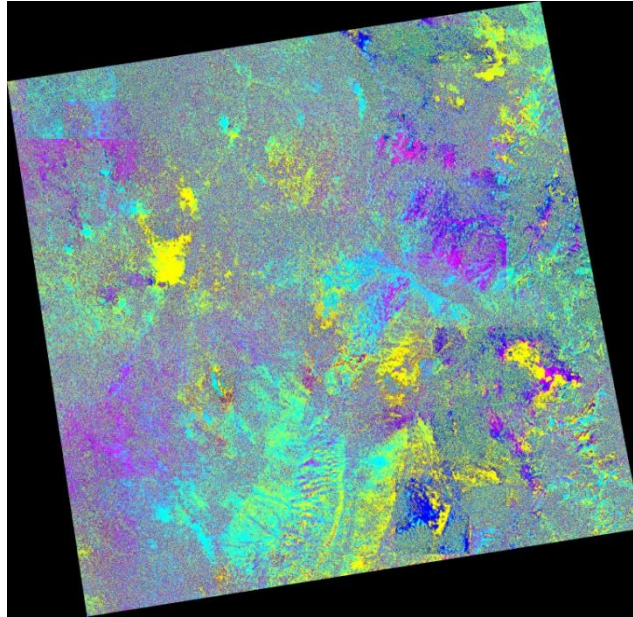


Figure 5.29: DInSAR Error Map

Table 5.2: Error ranges estimated in DInSAR

Error Range (Phase in Radians)
-6.2878 to -4.5085 [Red]
-4.5085 to -2.7292 [Green]
-2.7292 to -0.9499 [Blue]
-0.9499 to 0.8294 [Yellow]
0.8294 to 2.6087 [Cyan]
2.6087 to 4.3880 [Magenta]
4.3880 to 6.1673 [Maroon]
6.1673 to 7.9466 [Sea Green]

The Figure [5.29] shows the amount of atmospheric error introduced in the DInSAR. This much error when subtracted from the original DInSAR gives the atmospheric corrected DInSAR. The maximum error introduced in the phase of the DInSAR is 7.9466 radians. This amount of error leads to inaccurate measurements.

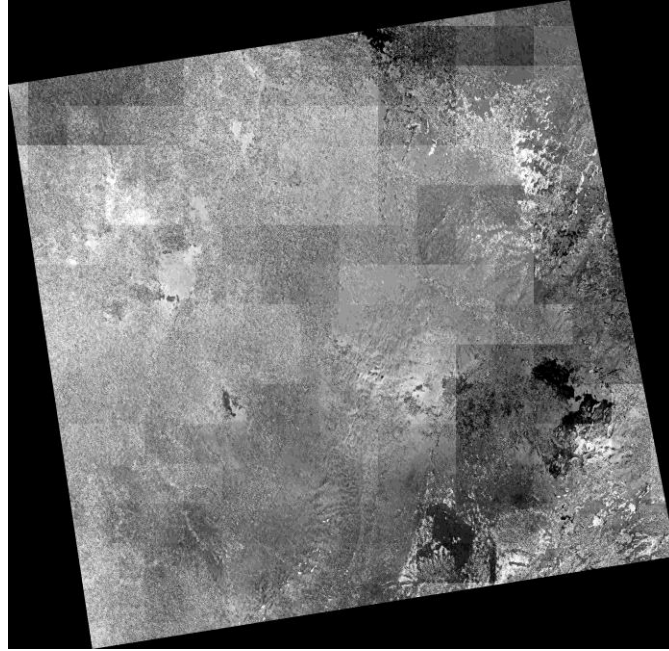


Figure 5.30: Phase image of DInSAR after correction

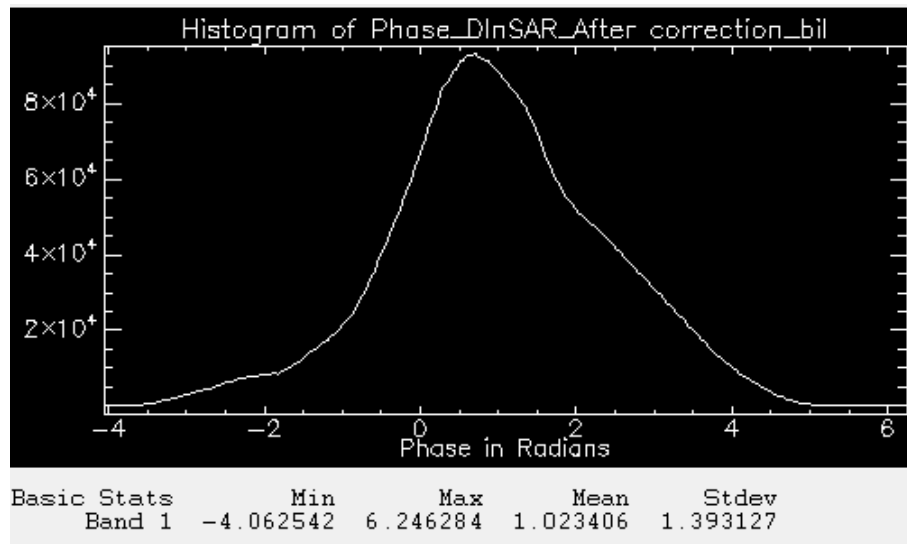


Figure 5.31: Phase variation of DInSAR after correction

The Phase of DInSAR before correction as seen in Figure [5.28] above shows a variation between -3 and +3 radians. After applying the correction, as seen in Figure [5.31], the phase values appear close to zero. The DInSAR which is an outcome of subtraction of two interferograms contains the displacement phase (topographic phase is removed). Since it is known that no significant movement of land due to processes such as earthquake has occurred in this region, there is no displacement phase present in the DInSAR. Most of the phase as seen in above figure has accumulated around zero. But the phase is not exactly equal to zero. This is because the baseline is not zero and also due to the presence of phase noise as explained for InSAR. The correction has influenced the values of the DInSAR to a great extent. When the phase of the DInSAR before correction and phase of the DInSAR after correction is observed, a drastic change is noticeable. Before correction, the phase as seen from Figure [5.28] shows random variation. Once the correction is applied, the phase values are altered and are brought back to a meaningful phase term. The same points considered for studying the phase variation of pair 1 and pair 2 of region 1 are selected here to study the difference in phase values before and after correction. The points are randomly chosen on the entire image leaving region 1. This is shown in Figure [5.32] below.

Also, the same comparative analysis conducted on InSAR is conducted on DInSAR. The phase of the whole interferogram is compared with the phase of region 1 which shows high coherence. Some 100 points are taken only on region 1 and compared with the phase obtained on the remaining area of study. This is to study the variation in phase after correction on both the areas of low and high coherence.

.

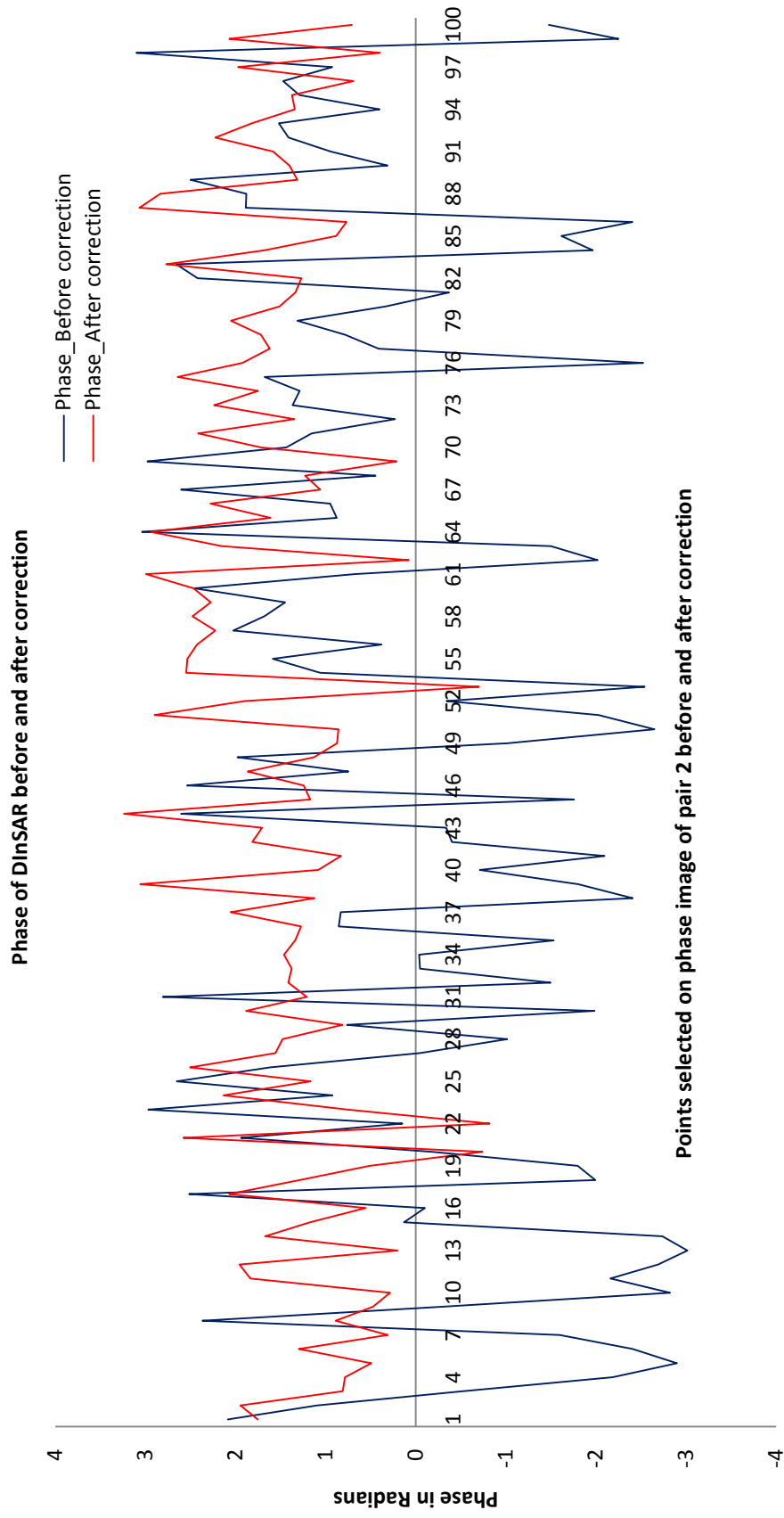
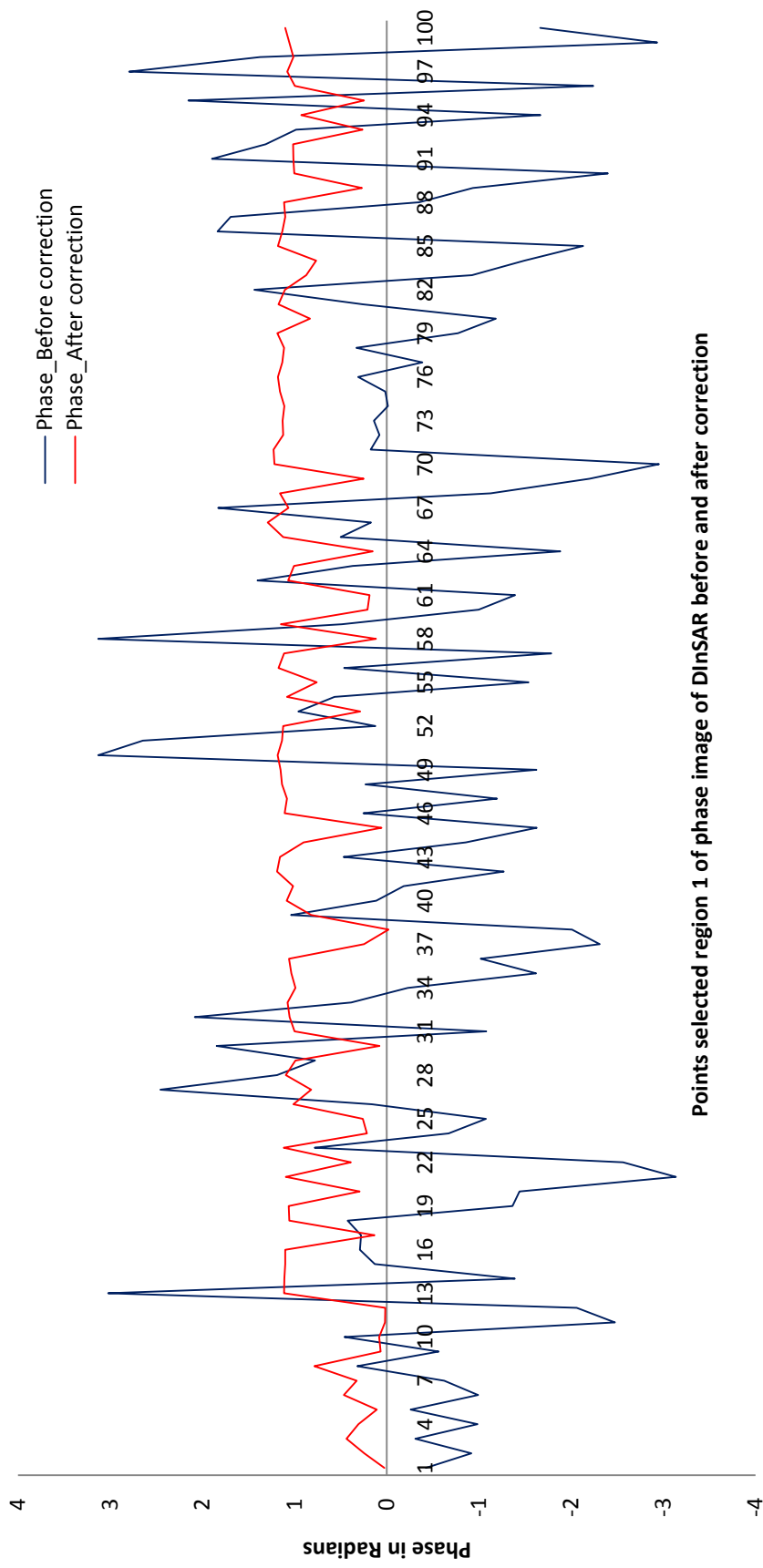


Figure 5.32: Phase of DInSAR before and after correction

The correction applied on the entire study area leaving region 1 has not performed effectively as can be seen from the figure above.

Comparison of phase (DInSAR) before and after correction on Region 1



Points selected region 1 of phase image of DInSAR before and after correction

Figure 5.33: DInSAR (100 points chosen on region 1 of study area)

The area of high coherence where no change has occurred shows the influence of error correction clearly. Once the correction is applied, phase values close to zero are noticeable.

It is clear from the above graphs that atmospheric error removal influences the DInSAR measurements to a significant extent. The changes in phase can be clearly noticed when the error correction is applied. In order to obtain reliable displacement measurements from a DInSAR, it is required to eliminate the atmospheric error. The main requirement of repeat-pass interferometry is coherence. If there is a coherence loss, this technique is not suitable for height and displacement measurements. The Figure [5.33] shows the effect of phase correction on the area of high coherence. The difference between the phase values of DInSAR before correction and after correction can be clearly seen in the above figure.

Once the corrected phase is obtained, the differential interferogram is generated by recombining the extracted module (intensity) component with the corrected phase. This gives a complex corrected differential interferogram.

The Figure [5.34] and Figure [5.35] below show the differential interferogram generated before and after correction.

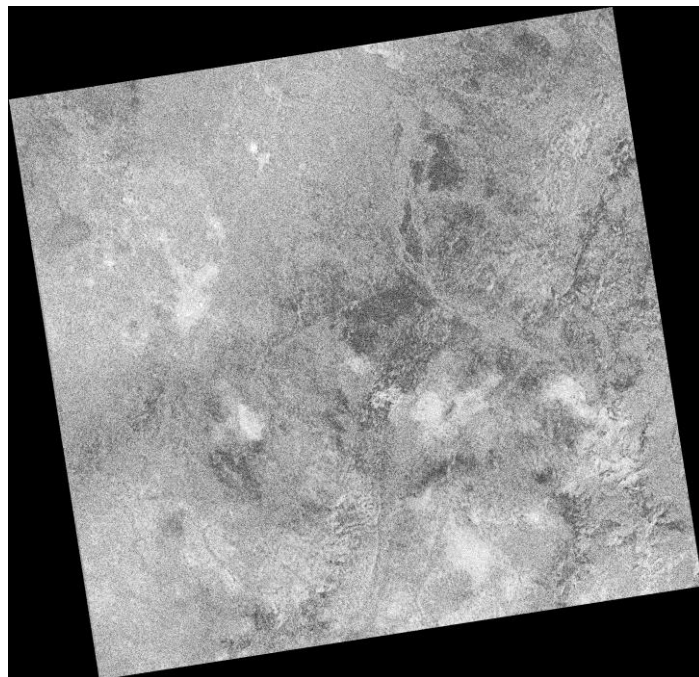


Figure 5.34: DInSAR before correction

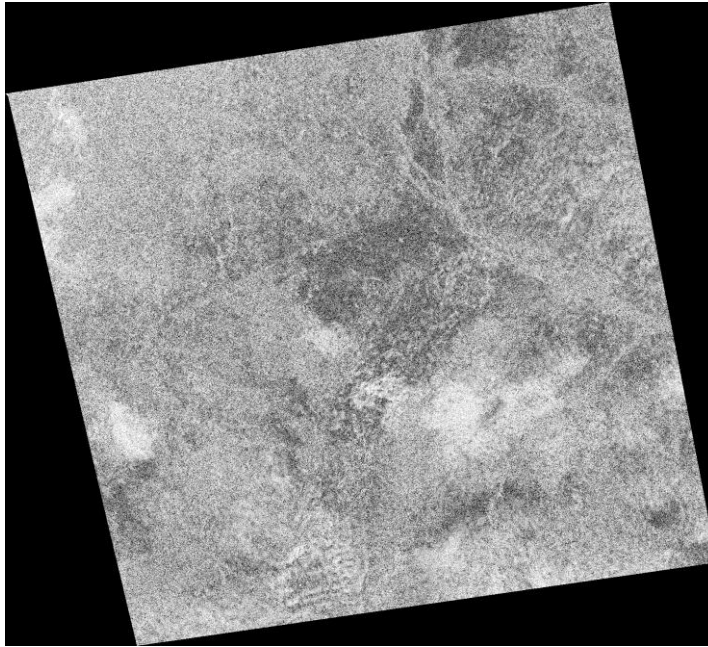


Figure 5.35: DInSAR after correction

5.4. Validation of the corrected interferograms

The phase of a SAR interferogram under ideal conditions (baseline = 0, no atmospheric disturbances), becomes zero. But this is practically not possible because in repeat-pass interferometry, there is no meaning in keeping a baseline of zero to extract height information and the atmospheric disturbances do exist in all conditions. The only way to reduce the errors induced in the phase to avoid erratic measurements is to eliminate atmospheric errors. Regions showing high coherence are an indication of phase stability between the acquisitions as discussed in section 5.2. For such regions, again under ideal conditions, the phase shown by the interferograms should be equal to absolute zero. Due to different baselines, phase difference of two images cannot reach a value zero as this is the special feature of interferometry from which the height is extracted. Thus, the extra path length added to the path of propagating RADAR wave by the atmosphere has to be reduced. This additional path length has the ability to corrupt the phase of the interferogram leading to inaccurate results. The interferograms obtained from both the image pairs after correction do not consist of phase values close to zero. This is due to the presence of different features within the study area which contribute to coherence loss. When the region 1 in which the features have not undergone any changes is considered, the phase of the interferograms before correction show phase values which are not reliable. Because the regions which show high coherence have similar phase values and would result in a phase difference of zero with zero baseline. Since, the baseline is not zero, there is some phase difference observed. This phase contains the extra path length due to the atmospheric refractivity. When this phase is removed, the exact phase difference is obtained which is reliable for height-displacement measurements. The correction when checked on the region of high coherence, reliable results are noticed i.e. the phase values appear close to zero as there is no change in the region and the region exhibits high coherence. This indicates that the atmospheric induced extra path length has been eliminated from the phase of the interferogram.

The principle of repeat-pass DInSAR is best described by considering a zero baseline. With no surface changes and coherence between images equal to one, the phase differences between images will be zero. Any small movement of the surface between the image acquisitions will add noise to the phase differences by decorrelating the signals. As it is a difficult task to maintain a zero baseline, DInSAR is employed with non-zero baselines which induce an extra phase shift. In this case, the DInSAR generated from the two interferograms for which atmospheric correction has been applied, shows phase values close to zero.

When the topo-pair containing phase due to baseline decorrelation and the defo-pair containing phase noise are used to generate DInSAR by considering the baseline conditions (equation (3.12)), a DInSAR with phase values close to zero and not exactly equal to zero (due to the non zero baseline and other phase noise) is generated. A clear difference between the DInSAR before correction and DInSAR after correction can be noticed from Figure [5.32] and Figure [5.33]. Any kind of movement of the surface would result in a significant variation of phase values. Though no displacement has occurred in the study area, the DInSAR before correction shows a large variation in phase values. But when the correction is applied, the phase values are corrected and a DInSAR with corrected phase values is obtained synchronizing with the no displacement phase.

6. CONCLUSIONS AND RECOMMENDATIONS

This chapter has been divided into conclusions (section 6.1) and recommendations (section 6.2)

6.1. Conclusions

The main topics addressed in this research work have been

- Effects of a refractive atmosphere on phase of interferograms
- Generation of a three-pass differential interferogram and elimination of atmospheric propagation delays from the same.

Interferometry technique utilizes the coherent properties of two or more electromagnetic waves to provide large-scale imaging and elevation measurements. This cloud-penetrating microwave system allows the generation of digital elevation models. From InSAR the height structure inside a RADAR pixel is extracted. A much more powerful technique termed differential interferometry or DInSAR is used to measure physical surface changes in the order of centimetres. DInSAR is being widely used in many applications in the field of geophysics, vulcanology and glaciology to measure small ground and ice movements, in ground displacement studies etc. The main aim of DInSAR is to identify the displacement component by removing the topographic phase. The topographic phase can be determined by using an external DEM (termed as two-pass differential interferometry) or by using another interferometric pair (termed as three-pass differential interferometry). In this work, the latter technique has been employed to generate a DInSAR. The repeat-pass interferometry technique facilitates deformation mapping which is possible using DInSAR.

The main problems with repeat-pass interferometry are surface decorrelation, baseline decorrelation and atmospheric signal in the data. The latter two error sources are influenced by the effective baseline length. A long baseline increases noise due to geometric decorrelation but reduces the effect of atmospheric disturbances. These error sources do not have any influence on single-pass interferometry as the data are acquired at the same time. The atmospheric component in the interferometric phase severely hinders the measurement when deriving the height or computing the displacement. It is possible to mitigate the effects of the atmosphere and be able to obtain correct measurements.

The two major atmospheric layers troposphere and ionosphere induce an additional path length to the RADAR wave propagating through them. The variations in the effective path length of the propagating wave arise due to the heterogeneous refractivity distribution in the atmosphere. This variation in refractivity is due to the variation of water vapour and presence of clouds. This adds an extra path length to the actual length of the propagating wave. The refractivity in troposphere depends on pressure, temperature and partial pressure of water vapour. On the other hand, the TEC present in the ionosphere are the cause for propagation path shortenings.

The tropospheric delay calculated using MODIS data acquired at the time of SAR data acquisitions varies between 2 m and 10 m. This delay along with the ionospheric delay of -5.39 m, -6.59 m and -7.19 m for the months of June, August and September respectively for L-band ALOS PALSAR data used resulted in a total path delay ranging from -3 m to 2 m. This amount of delay occurred in the path length of the

propagating RADAR wave is subtracted from the phase of the generated DInSAR to produce a DInSAR free from atmospheric effects.

The phase of the first the interferometric pair even after undergoing correction did not produce the desired phase (close to zero). The main reason behind this is the baseline decorrelation as this pair is obtained with a larger interferometric baseline in comparison with the other pair. The phase of second interferometric pair also did not give reliable results due to the presence of phase noise including temporal decorrelation, volume scattering etc. When the phase values after correction were checked on region 1 exhibiting high coherence, phase values close to zero were observed. This result is desirable because the phase of the regions which show high degree of similarity should lead to a phase difference of zero with a zero baseline. Since the baseline is not equal to zero, phase values close to zero and not exactly equal to zero are observed. These corrected interferometric pairs were used to generate a corrected DInSAR. The obtained DInSAR showed values close to zero. If any kind of surface movement was encountered, there would be a rapid variation in the phase. As it is already known that no significant movement/changes on the surface has taken place, the residual phase after correction is inferred to exist because of other phase noise and baseline decorrelation. The main focus of this work is atmospheric error removal which is achieved. When the remaining phase errors are accounted for, more accurate results will be obtained.

The atmospheric induced errors are one of the major limiting sources in repeat-pass InSAR measurements. Errors of over 10 cm can be introduced by these effects while taking ground deformation measurements. These effects can be eliminated by the use of meteorological models.

It can be concluded from this work that the atmospheric disturbances can hinder the InSAR measurements giving inaccurate results. The atmosphere has a major impact on the phase of a RADAR wave. Hence, it is essential to eliminate these errors from the phase of the interferogram to minimize the production of inaccurate measurements and thus make InSAR a powerful technique for height and ground displacement measurements.

6.2. Recommendations

The phase of an interferogram is a combination of atmospheric phase, phase due to baseline decorrelation, phase due to topography and other phase noise. The present work aims at removal of only atmospheric errors from the interferometric phase. The conditions of obtaining a phase difference of zero arises when DInSAR is carried out with a zero baseline and all the errors are eliminated from the InSAR phase. As it is difficult to handle the satellite orbits to maintain a baseline of zero, a non-zero baseline DInSAR technique is carried out for practical applications. Elimination of only atmospheric removal does not resolve the problem of phase errors. The phase error induced due to decorrelation of the non-zero baseline has to be accounted for. When there is no surface change, this correction should lead to a zero phase difference. In case of any small movement, decorrelation of signals is encountered indicating changes on the surface. This technique is very useful for determining ground displacements, changes in ground water, any changes due to urban construction, glacier studies etc. It is proposed to carry out further work considering the errors due to baseline decorrelation and other phase noise in order to obtain precise measurements.

The main focus of the present work is to study the atmospheric propagation effects on the phase of interferograms and removal of this error. The phase unwrapping problems associated with the DInSAR have not been covered. The phase variation in an interferogram can be modulo 2π . If the phase variation becomes larger than this value, the phase cycle repeats again from the start. It is mandatory to resolve this ambiguity. After obtaining the corrected interferogram, unwrapping the phase is required. Further work on the phase unwrapping techniques would lead to more accurate results.

LIST OF REFERENCES

- [1] I. H. Woodhouse, *Introduction to Microwave Remote Sensing*. CRC Press, 2006.
- [2] R. Burgmann, P. A. Rosen, and E. J. Fielding, "Synthetic Aperture Radar Interferometry to Measure Earth's Surface Topography and its Deformation," *Annual Review Earth Planet Science*, pp. 169-209, 2000.
- [3] P. Rosen et al., "Synthetic Aperture Radar Interferometry," in *Proceedings of the IEEE*, vol. 88, p. 50, 2000.
- [4] F. I. Okeke, "InSAR Operational and Processing Steps for DEM Generation," in *Promoting Land Administration and Good Governance*, pp. 1-13, 2006.
- [5] X. Ding, Z. Li, J. Zhu, G. Feng, and J. Long, "Atmospheric Effects on InSAR Measurements and Their Mitigation," *Sensors*, vol. 8, no. 9, pp. 5426-5448, 2008.
- [6] R. Hanssen, *Radar interferometry : data interpretation and error analysis*. Dordrecht, Boston: Kluwer Academic, 2001.
- [7] M. Doin, C. Lasserre, G. Peltzer, O. Cavalie, and C. Doubre, "Corrections of stratified tropospheric delays in SAR interferometry: Validation with global atmospheric models," *Elsevier B.V.*, vol. 69, no. 1, pp. 35-50, 2009.
- [8] A. Danklmayer, B. J. Doring, M. Schwerdt, and M. Chandra, "Assessment of Atmospheric Propagation Effects in SAR Images," *IEEE Transactions on Geoscience and Remote Sensing*, vol. 47, no. 10, pp. 3507-3518, 2009.
- [9] S. Yaobin., W. Yunjia., G. Linlin., and R. Chris., "Differential Radar Interferometry and its Application in Monitoring Underground Coal Mining-Induced Subsidence," vol. 38, pp. 227-232, 2009.
- [10] A. K. Gabriel, R. M. Goldstein, and H. A. Zebker, "Mapping Small Elevation Changes over Large Areas: Differential Radar Interferometry," *Journal of Geophysical Research*, vol. 94, pp. 9183-9191, Jul. 1989.
- [11] A. Ferretti, A. Monti-Guarnieri, C. Prati, and F. Rocca, *InSAR Principles: Guidelines for SAR Interferometry Processing and Interpretation*, 19 vols. The Netherlands: ESA Publications, 2007.
- [12] J. P. M. Boncori, "Error Modelling for SAR Interferometry and Signal Processing Issues Related To The Use Of An Encoding SAR Transponder," Ph.D. Thesis, University of Rome "Tor Vergeta", 2006.
- [13] J. Askne and H. Nordius, "Estimation of Tropospheric Delay for Microwaves from Surface Weather Data," *Radio Science*, vol. 22, no. 3, pp. 379-386, Jun. 1987.
- [14] L. Graham, "Synthetic Interferometer Radar for Topographic Mapping," *Proceedings of the IEEE*, vol. 62, no. 6, pp. 763-768, Jun. 1974.
- [15] H. Zebker and R. Goldstein, "Topographic Mapping From Interferometric Synthetic Aperture Radar Observations," *Journal of Geophysical Research*, vol. 91, no. 5, pp. 4993-4999, Apr. 1986.
- [16] F. Li and R. Goldstein, "Studies of Multibaseline Spaceborne Interferometric Synthetic Aperture Radars," *IEEE Transactions on Geoscience and Remote Sensing*, vol. 28, no. 1, pp. 88-97, Jan. 1990.
- [17] A. K. Gabriel and R. M. Goldstein, "Crossed orbit interferometry: theory and experimental results from SIR-B," *International Journal of Remote Sensing*, vol. 9, no. 5, pp. 857-872, 1988.
- [18] S. Madsen, H. Zebker, and J. Martin, "Topographic Mapping Using Radar Interferometry: Processing Techniques," *IEEE Transactions on Geoscience and Remote Sensing*, vol. 31, no. 1, pp. 246-256, Jan. 1993.
- [19] R. Gens and J. L. Van Genderen, "Review Article SAR interferometry - issues, techniques, applications," *International Journal of Remote Sensing*, vol. 17, no. 10, pp.

- 1803-1835, 1996.
- [20] H. Zebker, P. A. Rosen, R. Goldstein, A. Gabriel, and C. Werner, "On the derivation of coseismic displacement fields using differential radar interferometry: The Landers earthquake," *Journal of Geophysical Research*, vol. 99, no. 10, pp. 617-634, Oct. 1994.
 - [21] A. Reigber, "Airborne Differential SAR Interferometry: First results at L-band," *IEEE Transactions on Geoscience and Remote Sensing*, vol. 41, no. 6, pp. 1516-1520, Jun. 2003.
 - [22] H. Lee and J. G. Liu, "Topographic Phase Corrected Coherence Estimation using Multi-pass Differential SAR Interferometry: Differential Coherence," *IEEE*, pp. 776-778, 2000.
 - [23] G. Linlin, H. Chang, L. Qin, M. Chen, and Rizos Chris, "Differential Radar Interferometry For Mine Subsidence Monitoring," in *11th FIG Symposium on Deformation Measurements*, 2003.
 - [24] L. Bayuaji, J. T. S. Sumantyo, and H. Kuze, "ALOS PALSAR D-InSAR for land subsidence mapping in Jakarta, Indonesia," *Canadian Journal of Remote Sensing*, vol. 36, no. 1, pp. 1-8, Feb. 2010.
 - [25] M. Eineder and J. Holzner, "Phase Unwrapping of Low Coherence Differential Interferograms," *IEEE*, pp. 1727-1730, 1999.
 - [26] R. Goldstein, "Atmospheric limitations to repeat-track radar interferometry," *Geophysical Research Letters*, vol. 22, no. 18, pp. 2517-2520, Sep. 1995.
 - [27] D. Massonnet and K. Feigl, "Discrimination of geophysical phenomena in satellite radar interferograms," *Geophysical Research Letters*, vol. 22, no. 12, pp. 1537-1540, Jun. 1995.
 - [28] H. Zebker, P. Rosen, and S. Hensley, "Atmospheric Effects in Synthetic Aperture Radar Surface Deformation and Topographic Maps," *Journal of Geophysical Research*, vol. 102, no. 4, pp. 7547-7563, Apr. 1997.
 - [29] M. Jehle, O. Frey, D. Small, E. Meier, and D. Nuesch, "Improved knowledge of SAR Geometry through Atmospheric Modelling," *Remote Sensing Laboratories, University of Zurich*, pp. 1-3, Feb. 2008.
 - [30] R. F. Hanssen, "High-Resolution Water Vapour Mapping from Interferometric Radar Measurements," *Science*, vol. 283, no. 5406, pp. 1297-1299, 1999.
 - [31] J. Saastamoinen, "Contributions to the theory of atmospheric refraction," *Bulletin Géodésique*, vol. 105, no. 1, pp. 279-298, 1972.
 - [32] R. Hanssen and A. Feijt, "A first quantitative evaluation of atmospheric effects on SAR interferometry," *Fringe '96 workshop, ERS SAR Interferometry*, 1996.
 - [33] H. Tarayre and D. Massonnet, "Effects of a Refractive Atmosphere on Interferometric Processing," *IEEE*, pp. 717-719, 1999.
 - [34] R. Hanssen, S. Lehner, and I. Weinreich, "Atmospheric Heterogeneties from ERS Tandem Interferometry and Sea Surface Images," *Proceedings of CEOS SAR workshop*, 1988.
 - [35] Z. Xu, J. Wu, and Z. Wu, "A survey of ionospheric effects on space-based radar," *Waves in Random Media*, vol. 14, no. 2, pp. S189-S273, 2004.
 - [36] J. Liu, Y. Kuga, and A. Ishimaru, "Simulations of Ionospheric Effects on SAR at P-band," *IEEE*, pp. 1842-1844, 1999.
 - [37] E. J. M. Rignot, "Effect of Faraday Rotation on L-Band Interferometric and Polarimetric Synthetic-Aperture Radar Data," *IEEE Transactions on Geoscience and Remote Sensing*, vol. 38, no. 1, pp. 383-390, Jan. 2000.
 - [38] P. Snoeij, N. Van der Valk, E. Boom, and D. Hoekman, "Effect of the Ionosphere on P-band Spaceborne SAR Images," *IEEE*, pp. 132-134, 2001.
 - [39] USGS Earth Resources and Earth Observation Science (EROS) Center, "MODIS

- Reprojection Tool, User's Manual," Land Processes DAAC USGS Earth Resources and Earth Observation Science (EROS) Center, 26-Sep-2009.
- [40] W. Menzel, A. Frey, and A. Baum, "Cloud Top Properties and Cloud Phase Algorithm Theoretical Basis Document," Oct-2010.
- [41] S. Singh, "Climatology," in *Climatology*, Allahabad, India: Prayag Pustak Bhawan, 2005.
- [42] S. Katsougiannopoulos, C. Pikridas, D. Rossikopoulos, I. Ifadis, and A. Fotiou, "Tropospheric Refraction Estimation Using Various Models, Radiosonde Measurements and Permanent GPS Data," in *PS5.4 – GNSS Processing and Applications*, p. 15, 2006.
- [43] *tre*, *Processing of synthetic aperture radar images*. London ;Hoboken NJ: ISTE ;;Wiley, 2008.
- [44] A. L. Buck, "New Equations for Computing Vapor Pressure and Enhancement Factor," *National Centre for Atmospheric Research*, pp. 1527-1532, Aug. 1981.
- [45] S. Schaer, G. Beutler, and M. Rothacher, "Mapping and Predicting the Ionosphere," in *Proceedings of the IGS AC workshop*, p. 12, 1998.
- [46] "Global Ionosphere Maps Produced by CODE," *University of Bern-Astronomisches Institute*, 23-Mar-2011. [Online]. Available: http://www.aiub.unibe.ch/content/research/gnss/code___research/igs/global_ionosphere_maps_produced_by_code/index_eng.html.
- [47] M. Jehle, M. R"uegg, D. Small, E. Meier, and D. N"uesch, "Estimation of Ionospheric TEC and Faraday Rotation for L-Band SAR," in *Proceedings of Society of Photographic Instrumentation Engineers*, vol. 5979, 2005.
- [48] S. Schaer, "Mapping and Predicting the Earth's Ionosphere using the Global Positioning System," 1999.
- [49] Z. Li, "Correction of Atmospheric Water Vapour Effects on Repeat-Pas SAR Interferometry Using GPS, MODIS and MERIS Data," Doctor of Philosophy, University of London, 2005.
- [50] A. Vasileisky, "Automated Sub-Pixel Coregistration of the Same Sensor Images by the Least Square Technology," pp. 1-8.
- [51] GAMMA Remote Sensing, "Interferometric SAR Processing," Nov-2007.
- [52] S. Kumar, "Retrieval of forest parameters from Envisat ASAR data for biomass inventory in Dudhwa National Park, U.P., India," M.Sc., Indian Institute of Remote Sensing (IIRS) and International Institute for Geoinformation Science and Earth Observation (ITC), 2009.
- [53] SARscape, "Synthetic Aperture Radar and SARscape," Sep-2008.
- [54] D. T. Sandwell, D. Myer, R. Mellors, M. Shimada, B. Brooks, and J. Foster, "Accuracy and Resolution of ALOS Interferometry: Vector Deformation Maps of the Father's Day Intrusion at Kilauea," *IEEE Transactions on Geoscience and Remote Sensing*, vol. 46, no. 11, p. 11, Nov. 2008.
- [55] North Atlantic Treaty Organization., *Radar polarimetry and interferometry*. Neuilly-sur-Seine Cedex: N.A.T.O. Research and Technology Organization, 2005.